Phase Space Dynamics in a Linear RFQ Trap for Time-of-Flight Mass Spectrometry

by

C.W. Van Fong

Department of Physics,
McGill University
Montreal, Canada

December, 2000

A thesis submitted to
the Faculty of Graduate Studies and Research
in partial fulfillment of the requirements for the degree of
Doctor of Philosophy

Ad maiorem Dei gloriam

Abstract

A new Linear RFQ Ion Trap/Axial Time-of-Flight mass spectrometer was developed and tested. A segmented quadrupole rod system was used to create a static axially confining field that could trap and cool an ion cloud from a DC ion source. In addition, an adjustable extraction field was applied, after sufficient ion collection, by pulsing the trapping rod segments to send the cooled ion cloud into a collinear Time-of-Flight spectrometer. Two chevron stacked multichannel plates, with a measured charge amplification of 3.75×10^{7}, were used as a detector at the end of the flight tube.

The purpose of this work was to investigate ion dynamics in the linear trap (LTRAP) so as to determine the suitability of this system as a source for TOFMS. The trap was therefore designed to be relatively weak so that the ion collection volume would be large enough to obtain a detailed picture of the cloud. The system was tested using a Cs^{+} ($m/z = 133$) ion source. Optimal parameters were found to be an applied well depth of –5V to –15V with a q value between 0.3 and 0.6 in a buffer gas environment of N_2 at pressures of 10^{-4} Torr or greater. Under these conditions and a cooling/collection time of 50ms the trap was observed to contain about 2500 ions. This translated to a detection efficiency of about 26.7% of the ions entering LTRAP.

Computer simulations based on a thermodynamic model were created to analyze the experimental data. The ion ensemble was found to reach an equilibrium temperature of 0.0353 ± 0.0025eV in less than 10ms. Another computer program was used to reconstruct the phase space density of the LTRAP collection from the detector signals. The results of this reconstruction agreed with the results obtained from the model fitting procedure thereby confirming the thermodynamic model.

The phase space density distribution in LTRAP showed that with a time-focusing reflectron even this weak trap would have a $m/\Delta m = 250$. This has led to guidelines for the construction of a high-resolution hybrid mass spectrometer using a linear ion trap. Based on these current results, a mass resolution of almost 10,000 is predicted as an upper limit of this type of mass spectrometer.

Résumé

Un nouveau spectromètre de masse de type "piège d'ion RFQ linéaire/temps-de-vol axial a été développé et testé. Un système quadrupolaire de tiges segmentées a été employé pour créer un champs statique confinant axialement qui peut emprisonner et refroidir un nuage d'ions provenant d'une source d'ions continue. De plus, après une collection suffisante d'ions, un champs d'extraction pulsé réglable a été appliqué sur les segments des tiges de piégeage pour envoyer le nuage refroidi d'ions dans un spectromètre de temps-de-vol situé sur la même axe. Deux détecteurs multicanaux montés en style chevron, avec une amplification de charge mesurée de $3{,}75\times10^{7}$, ont été utilisés comme détecteur à l'extrémité du spectromètre.

Le but de ce travail était d'étudier la dynamique des ions dans le piège linéaire (LTRAP) afin de déterminer la performance de ce type de système comme source pour TOFMS. Le piège a été donc conçu pour être relativement peu profond pour que la collection d'ions se passe sur un volume assez grand pour obtenir une image détaillée du nuage d'ions. Le système a été testé utilisant une source d'ion de Cs+ ($m/z = 133$). Les paramètres optimaux se sont avérés être une profondeur appliquée du piège de -5V à -15V avec une valeur de q entre 0,3 et 0,6 dans un environnement de gaz tampon d'azote aux pressions de 10^{-4} Torr ou plus. Dans ces conditions et avec un temps de refroidissement/collection de 50ms, on a observé que le piège contient environ 2500 ions. Ceci se traduit par une efficacité de détection d'environ 26,7% des ions entrant le LTRAP.

Des simulations sur ordinateur basées sur un modèle thermodynamique ont été réalisées pour analyser les données expérimentales. De cette analyse on peut conclure que l'ensemble d'ions atteint une température d'équilibre de $0{,}0353 \pm 0{,}0025$eV en moins de 10ms. Un autre programme a été employé pour reconstruire l'espace de phase des ions dans LTRAP à partir des signaux du détecteur multicanaux. Les résultats de cette reconstruction sont conformes aux résultats obtenus à partir du modèle confirmant de ce fait le modèle thermodynamique.

L'espace de phase mesurée dans LTRAP a démontré qu'avec un "time-focusing reflectron" même ce piège peu profond aurait un $m/\Delta m = 250$. Ces résultats ont mené à la discussion des paramètres pour la construction d'un spectromètre de masse hybride à haute résolution basé sur un piège d'ion linéaire. On montre qu'une résolution de masse de presque 10 000 est prévue comme limite supérieure de ce type de spectromètre de masse.

Acknowledgements

I would like to express my heartfelt thanks to Dr. R.B. Moore, who guided me through this entire process, from start to finish. He provided the inspiration and the original concepts that resulted in this thesis as well as the timely advice and masterful touches throughout the months and years. I especially thank him for the many times during the assembly of the system when he stepped in and completed in short time what would have taken me days to do. This thesis would also not have been written if it were not for his help. Above all, I thank him for having seen the potential in me and for giving me opportunity and direction, going back as far as my undergraduate days.

I would like to thank NSERC for granting me the IPS scholarship that supported my research through the years, it would not have been possible without their help. I also thank MDS SCIEX and its Research and Development department for having taken an interest in me and this project, for their years of support and for allowing me to work with them and gain invaluable experience in the aspect of industrial research. Special thanks go to Dr. Bruce Thomson, Dr. Igor Chernushevich and Dr. Charles Jolliffe of MDS SCIEX, who gave me my first exposure to industrial R&D and made working at SCIEX a comfortable and friendly environment for me.

My gratitude goes to the many individuals at McGill University Physics department who have assisted me in my research. Firstly, I want to remember Dr. Taeman Kim, whom I studied with and who shared his great knowledge and experience with me as I learned about quadrupole mass spectrometry, computer simulations and everything else about working in a lab. I also wish to thank Dr. Leo Nikkinen for helping me with all the electronic components of my system, for designing the HVAmp, which was of utmost importance to my experiment, and for suffering all my daily questions for months on end. Special thanks go to Mr. Steve Kekani and Mr. Eddie Del Campo for helping me design each piece of the apparatus, for machining the difficult ones and for supervising me as I worked in the machine shop.

I was also greatly encouraged by the presence and support of those who saw me through from beginning to end: Jonathan Lee, John Crawford, Sid Gulick, Peter Varfalvy and Ali Alousi, who shared ideas with me as well as tools and equipment. I wish to also express my appreciation to the summer students who have assisted me in my research, Etienne Gagnon, for the translation work in this thesis, Omar Gianfrancesco, who helped me with the computer simulations and the high voltage cage; and Michael Ayles, who created all the stunning figures and diagrams in this thesis.

I dedicate this work to my family and friends, who have given me their encouragement and support without ever having been asked. My parents, my brother and his wife have all been a great source of love for me throughout the years; this thesis is primarily for them. I wish to thank my extended 'family' at the Montreal Chinese Alliance Church, for always keeping me in their thoughts and in their hearts. To Jocelyne, who accompanied me through this entire journey and who showed me more patience and understanding than I deserve, I will never be able to repay this debt of gratitude. Lastly, I thank God for never letting me go. My utmost for His highest.

Table of Contents

ABSTRACT IV

RÉSUMÉ V

ACKNOWLEDGEMENTS VII

TABLE OF CONTENTS IX

LIST OF FIGURES XI

LIST OF TABLES XVI

CHAPTER 1 INTRODUCTION 1

1.1 OVERVIEW OF DYNAMIC MASS SPECTROMETERS 4
1.1.2 Mass Filters and Transform Spectrometers 6
1.2 LITERATURE REVIEW OF TANDEM MASS SPECTROMETER/TIME-OF-FLIGHT SYSTEMS 9
1.3 BASICS OF TIME-OF-FLIGHT MASS SPECTROMETRY 14
1.4 METHODOLOGY OF THIS STUDY 19
1.4.1 Description of the LTRAP system 20
1.5 CONTRIBUTIONS OF THIS THESIS 21

CHAPTER 2 THEORY AND BACKGROUND 24

2.1 PRINCIPLES OF DYNAMIC ION MANIPULATION 24
2.2 QUADRUPOLE ION BEAM GUIDE 27
2.2.1 The Oscillating Quadrupole Field 27
2.2.2 Equations of Motion – The Mathieu Equation 30
2.2.3 The Pseudopotential Well 33
2.3 ION BEAM COOLING AND TRAPPING 36
2.3.1 Introduction to Phase Space Dynamics 36
2.3.2 Ion Temperature and Ion Cooling 44
2.3.3 Collisional Cooling, Evaporative Cooling and RF Heating 47
2.4 TIME-OF-FLIGHT SPECTROMETRY 49
2.4.1 Basic Principles of Time-of-Flight 49
2.4.2 A Phase Space Approach to Time-of-Flight Spectrometry 51
2.5 TOMOGRAPHIC PHASE SPACE RECONSTRUCTION 56
2.5.1 The Fourier Slice Theorem 56
2.5.2 Parallel Projections in Phase Space 61
2.6 TIME-OF-FLIGHT SPECTROMETRY AND LIOUVILLE'S THEOREM– A SUMMARY 63

CHAPTER 3 EXPERIMENTAL SYSTEM 64

3.1 ION SOURCE AND BEAM COOLING SYSTEM: AXF_RFQ 64
3.1.1 Ion Gun Assembly 65
3.1.2 AXF_RFQ 68
3.1.3 Miniature Quadrupole System 70
3.2 ION TRAPPING AND PULSING SYSTEM: LTRAP 71
3.2.1 Principles of an Axially Trapping Beam Guide 71
3.2.2 Segmented Rod Structure 75
3.2.3 Electrical Systems 77
3.3 TIME-OF-FLIGHT SYSTEM 80
3.3.1 Time-of-Flight Tube 81
3.3.2 Deflection Plates 81
3.3.3 Einzel Lens 82
3.4 ION DETECTION AND DATA ACQUISITION 83
3.4.1 Microchannel Plate Assembly 83
3.4.2 Signal Detection and Data Acquisition 85
3.5 VACUUM CONSIDERATIONS 88

CHAPTER 4 COMPUTER MODELING AND SIMULATIONS 90

4.1 MODELING PHASE SPACE 90
4.1.1 Field Calculations for the Pseudopotential Well 91
4.1.2 Temperature Calculations: σ_z and σ_{p_z} 92
4.1.3 Representative Particles in Phase Space 94
4.2 SIMION TRAJECTORY CALCULATIONS 97
4.2.1 On-Axis Pulse Extraction 97
4.2.2 Full 3D Pulse Extraction: Radial Measurements 99
4.3 TIME-OF-FLIGHT SIMULATION 99
4.3.1 Drift Field Calculations: Building Time Histograms 99
4.3.2 Temperature Fitting Routine 101

CHAPTER 5 RESULTS AND DISCUSSION 103

5.1 EXPERIMENTAL RESULTS: TIME-OF-FLIGHT PROFILE 103
5.2 TRAPPING AND EXTRACTING IONS IN LTRAP 104
5.2.1 General Trapping Conditions 105
5.2.2 Overall LTRAP Efficiency 113
5.2.3 Time-of-Flight Performance 114
5.3 SIMULATION RESULTS 121
5.3.1 Temperatures Measurements 121
5.3.2 Phase Space Reconstruction 125

CHAPTER 6 SUMMARY AND CONCLUSION 131

6.1 SUMMARY OF RESULTS 131
6.2 IMPLICATIONS FOR TOF MASS SPECTROMETRY 133
6.3 SUGGESTED FUTURE WORK 136

REFERENCES 139

APPENDIX A: AUTOCAD® RENDERED DIAGRAMS 144

List of Figures

Fig. 1.1 The quadrupole ion beam guide (*left*) and the quadrupole ion (Paul) trap (*right*). 2

Fig. 1.2 Schematic diagram of the Ion Trap/Time-of-Flight mass spectrometer. 10

Fig. 1.3 Schematic diagram of MDS SCIEX's QqTOF system. 11

Fig. 1.4 Schematic diagram of the Linear Ion Trap Time-of-Flight mass spectrometer. 13

Fig. 1.5 The action diagram of a simple collection of particles occupying an axial extent Δz and having a momentum spread of Δp_z. For reference, the corners of the rectangle have been labeled *a*, *b*, *c*, *d*. 14

Fig. 1.6 The action diagram, in *E-t* coordinates, of the ion collection of Fig. 1.5 upon being accelerated into a field free region. 15

Fig. 1.7 The *E-t* action diagram of the ion collection of Fig. 1.5 after having drifted to its time focus. 16

Fig. 1.8 The *E-t* action diagram of the ion collection of Fig. 1.7 after having drifted past its time focus. 16

Fig. 1.9 Schematic diagram of a reflecting TOF mass spectrometer. 17

Fig. 1.10 The *E-t* action diagram of the ion collection of Fig. 1.8 after being reflected and allowed to drift to a new time focus. 17

Fig. 2.1 Two examples of Gauss' law: *Left* – A central charge in a volume (*dashed*) forms radial electric field lines (*above*); creating a parabolic potential minimum (*below*). *Right* – In the absence of any charge, field lines entering a volume must also leave the volume (*above*); creating a potential minimum in one dimension and a maximum in another (*below*). 26

Fig. 2.2 Hyperbolic electrode structures required to generate the quadrupolar field. The equipotential field lines for such a configuration are shown in the inset $\varphi = \varphi_o\left(x^2 - y^2\right)/2r_o^2$. 28

Fig. 2.3 The Mathieu stability diagram for the ion beam guide, showing the first 3 regions of stability in the x and y directions. Areas of overlapping gray represent simultaneous stability in both directions. 31

Fig. 2.4 First stability region of the Mathieu diagram. The iso-β curves are shown for stable x and y values. 32

Fig. 2.5 Plot of transverse ion motion vs. time for a q value = 0.1. The micromotion is seen to be an RF oscillation on top of the simple harmonic macromotion oscillation. 35
Fig. 2.6 Phase space ellipses representing the paths of particles that are confined by a parabolic potential minimum. The maximum amplitude of oscillation is A and maximum momentum is $m\omega A$. 37
Fig. 2.7 Liouville's theorem: Boundary points (represented by **B**) define a volume in phase space as it evolves in time (**B'**). Interior points (**I**) must always stay within the volume (**I'**), while points exterior to the volume (**E**) remain forever outside (**E'**). 39
Fig. 2.8 General action diagram ellipse showing critical values 41
Fig. 2.9 Emittance and acceptance ellipses. 42
Fig. 2.10 Action diagram of the time evolution of particles travelling in a field free region. 43
Fig. 2.11 Action diagram of the time evolution of particles travelling in a constant field region. 44
Fig. 2.12 Density distribution as a projection in an action diagram for a particular direction in phase space. The distribution represents particles in a simple harmonic oscillator at thermal equilibrium. 46
Fig. 2.13 Schematic diagram of a Time-of-Flight system, detailing the Extraction Region, Drift Region and Detector. TOF spectrometry works on the principle that lighter masses arrive at the detector earlier than heavy masses. 50
Fig. 2.14 Example of a TOF spectrum. MS/MS of 2+ ion of Glu-fibrinopeptide B (m/z=785.8). 51
Fig. 2.15 Phase space evolution of ion ensemble in TOF system. 52
Fig. 2.16 An object $f(x, y)$ and its projection $P_\theta(t_1)$ are shown for an angle of θ. 57
Fig. 2.17 Parallel projections at different viewing angles. 58
Fig. 2.18 The Fourier Slice Theorem relates the Fourier transform of a projection to the Fourier transform of the object along a radial line (BB') 59
Fig. 2.19 Collecting projections of the object at a number of angles gives estimates of the Fourier transform of the object along radial lines. In practice, since an FFT algorithm is used to transform the data, the dots represent the actual location of estimates of the object's Fourier transform. 60
Fig. 2.20 A conceptual diagram showing how to use the backprojection technique to reconstruct the image of a circle. 61
Fig. 2.21 Detected ion signal as a phase space projection. The ion signal (*at right*) corresponds to the integration of the phase space density function at the detector (*center*, shaded area) which can be related to a volume in phase space at the trap (*at left*, shaded area). 62
Fig. 2.22 Adjusting angle of projection by varying extraction voltage. 62
Fig. 3.1 Mass spectrum of ion source taken from TOF data. The mass peaks were calibrated to $_{55}Cs^{133}$. The peaks $m/z = 85$ and $m/z = 87$ correspond to $_{37}Rb^{85}$ and its isotope $_{37}Rb^{87}$, which have relative abundances of 72.15% and 27.85% respectively [Han72]. 66
Fig. 3.2 Ion Gun assembly. 67

Fig. 3.3 Segmented Quadrupole rods. AC voltages **RFX** and **RFY** are applied to opposing pairs of rods. DC voltages **DCF** and **DCB** are applied to the front and back segments of the rods. Each segment is coupled to its neighbors by a 1kΩ resistor (*not shown*). 69

Fig. 3.4 Graph of the potential surface on the plane between two segmented rods, showing the smooth gradient on axis. The steps correspond to the bias voltage on individual rod segments. The equipotential lines reveal slight field imperfections only near the rod surfaces but are nearly parallel in the middle. 69

Fig. 3.5 Miniature quadrupole assembly. The cross-sectional view (*at left*) demonstrates how the miniature quadrupole matches the equipotential field lines without disturbing the quadrupolar field. The miniature quadrupole holder serves as the vacuum separator between to pressure regimes (*at right*). 70

Fig. 3.6 Assigning a trapping voltage $-V_{DC}$ in an axially confining rod configuration. 72

Fig. 3.7 Pseudopotential and axial trapping potential. The graph represents the potential within the region defined by $0 \le r \le r_o$ and $-z_o \le z \le z_o$. Figures **(a)** – **(d)**: Stable trapping conditions. Figure **(e)**: Critical trapping condition. Figure **(f)**: Unstable condition; the axial field causes a defocusing force greater than the pseudopotential. 74

Fig. 3.8 Schematic view of LTRAP, showing rod segments being paired by connector bands. Segments **I-VI** form the axial trap at the end of the rods. 75

Fig. 3.9 End view of the LTRAP assembly and rigid wire connectors in mock set-up. 76

Fig. 3.10 Side view of the LTRAP assembly and connectors. 76

Fig. 3.11 Circuit diagram detailing how the RF signal and DC biases were coupled and fed to each rod segment (points 1-12). 78

Fig. 3.12 Circuit diagram of 3 transformers. Center taps are controlled by HV switches that pulse the segments up/down. These transformers control the voltages for the 3 LTRAP segments (**I-VI**) 79

Fig. 3.13 Sequence of operation for LTRAP collection and extraction. 80

Fig. 3.14 A pair of deflector plates inside the flight tube. Adjusting the voltage between the plates 'steers' the ion packet as it continues down the drift tube. 82

Fig. 3.15 MCP assembly diagram. 84

Fig. 3.16 MCP detector assembly diagram. 85

Fig. 3.17 Multi-channel analyzer spectrum of pulse heights. The calibration peak is at channel 1008 while the single ion peak is at channel 149. 86

Fig. 3.18 Calibrating pulse (*left*) and adjusted single ion pulse (*right*). 87

Fig. 4.1 Spatial distribution of a randomly generated ensemble of ions. The full six-dimensional phase space volume occupied by the cloud is the product of the six probability functions and is a function of temperature *T*. 94

Fig. 4.2 Representative phase space points. 95

Fig. 4.3 1441 representative phase space points plotted with their weighting factors. 96

Fig. 4.4 SIMION extraction simulation of 1441 particles. 98

Fig. 4.5 Example of various temperature curves fitted to experimental data. The closest temperature curve was found to be $k_B T = 0.035$ eV. ____ 102
Fig. 5.1 Typical experimental TOF data recorded at the MCP detector. ____ 103
Fig. 5.2 A series of TOF peaks as a function of collection time. This was extracted with $200V_{ext}$ from an initial trap setting of q=0.6 and a well depth of 10V. ____ 106
Fig. 5.3 Number of detected ions versus Collection Time. The experiment was carried out for various RF voltages on the LTRAP rods. The interpolation lines are polynomial fits to the experimental data points. ____ 107
Fig. 5.4 Number of detected ions versus well depth voltage. All experimental data was taken with $V_{RF} = 200V_{pp}$. The trendlines were generated using a polynomial fit to the data points. ____ 108
Fig. 5.5 A graph showing the transition between ions occupying the normal LTRAP region and ions falling into the "parasitic" trap region. The axial well depth was set to –1.5V and the transition was created by increasing the DC bias voltage on the final trap segment. ____ 110
Fig. 5.6 Waterfall plot of TOF spectra as a function of extraction voltages. ____ 111
Fig. 5.7 Plot of sensitivity (*left scale*) and resolution (*right scale*) versus extraction voltage. One will always be optimized at the expense of the other in a mass spectrometer. ____ 113
Fig. 5.8 Waterfall plot of TOF spectra as a function Time-of-Flight Bias Voltage. ____ 115
Fig. 5.9 Plot of sensitivity (*left scale*) and mass resolution (*right scale*) versus the TOF bias voltage. ____ 116
Fig. 5.10 Computer simulated deflection of a parallel ion beam (*left*). The transverse deflection was used to create a calibration curve for the deflector plates (*right*). ____ 117
Fig. 5.11 Calibrated graph showing signal intensity versus deflection. The experimental data (◆) shows that the actual system is biased a little to the +x direction in this graph. The simulated data ( ) shows that the predicted radial extent of the pulse is ±60mm. ____ 118
Fig. 5.12 Distribution of ions at the plane of the detector. This simulation data was taken from 5000 randomly generated ions that were pulsed to the detector, showing the radial distribution of ions. Roughly 1/5 of the ions are within the detector surface (*outlined in black*). ____ 118
Fig. 5.13 Simulated ion trajectories being focused by the Einzel lens system. Note that the y-axis scale has been exaggerated, the actual beam divergence at the entrance mesh is about a 3° cone. ____ 119
Fig. 5.14 Distribution of 5000 simulated ions at the plane of the detector after being focused by the Einzel lens. The black circle represents the effective detector surface area. ____ 120
Fig. 5.15 Graph of initial ion temperature in LTRAP as a function of the applied extraction voltage. ____ 121
Fig. 5.16 Graph of initial ion temperature as a function of collection time. The curve is an exponential fit to the data points. ____ 122
Fig. 5.17 Graph of the initial ion temperature as a function of the buffer gas pressure in the LTRAP region. The curve is an exponential fit to the data points. ____ 125

Fig. 5.18 Representation of the parallel phase space projection of the initial ion distribution in the LTRAP system. This projection was reconstructed from actual experimental data. 126
Fig. 5.19 Another phase space projection taken at an extreme viewing angle. 127
Fig. 5.20 Composite representation of the initial ion distribution, using projections from 17 different viewing angles. 128
Fig. 5.21 Fully symmetric representation of the initial ion distribution in z-p_z phase space. The white ellipse at the base of the distribution represents the theoretical 3σ volume. 129
Fig. 6.1 Proposed hybrid trap design. *Above*-The trapping electrodes, defined by DC voltages V_1, V_{Trap} and V_2, are designed to improve axial electric field shape and enhance performance in ion confinement and extraction. *Below*-Cross-sectional view of one set of electrodes, showing the positions of both RF and DC segments. 137

List of Tables

Table 1.1 Table of dynamic mass spectrometers (Blauth [Bla66]). 5

Table 3.1 Microchannel plate characteristics. 83

Table 5.1 Default values for the operating parameters of LTRAP. 104

Table 5.2 Extraction Data Table. The first four columns summarize the data in Fig. 5.6. The last two columns show the simulation parameters used to obtain the best fit to the data. The results underneath show the averaged values for these parameters as well as their errors. 111

Table 5.3 Table of LTRAP transmission efficiency data. 114

Table 5.4 V_{TOF} Data Table. The table represents the data shown in Fig. 5.8. 115

"My God, since You are with me, and since it is Your will that I should apply my mind to these outward things, I pray that You will give me the grace to remain with You and to keep company with You. But so that my work may be better, Lord, work with me; receive my work and possess all my affections"

Brother Lawrence

Chapter 1 Introduction

In 1989, Norman Ramsey, Wolfgang Paul and Hans Dehmelt were awarded the Nobel Prize in Physics, recognizing their contributions in the field of atomic spectroscopy. These contributions were essentially new atomic standards for measurements of time and mass and, through the modern definition of the velocity of light, for measurements of space as well. Thus the Nobel committee was recognizing contributions to the most fundamental measurements that can be made; those of space, time and matter.

The importance of the contributions of Ramsey in establishing a new standard for time, i.e. the cesium clock, is easily seen in applications such as the Global Positioning System where time measurements are now used to determine positions on the surface of the Earth to within meters. The contributions of Paul and Dehmelt, primarily in the measurement of atomic properties, while a little more subtle, are just as important to modern science and technology. This is demonstrated by one of the contributions of Dehmelt, the determination of the magnetic moment of the electron to 12 significant figures. This measurement, which is 4000 times better than that of any previous measurement, tests the very limit of our understanding of one of the most basic particles of the universe; the electron.

The contributions of Paul and Dehmelt resulted from their use of electromagnetic traps, specifically the radiofrequency quadrupole trap (also named the Paul trap, after its inventor W. Paul himself) and the Penning trap (its magnetic counterpart, named after its inventor F. M. Penning). Their work was representative of a turning point in the development of electromagnetic traps and the technology associated with them. Although invented by physicists, the Penning trap in 1935 and the Paul trap in 1957, it was primarily the chemists that immediately recognized their potential as mass measurement devices for atomic and molecular analysis. The quadrupole ion trap and its linear counterpart, the quadrupole ion mass filter (Fig. 1.1), as well as the Penning trap, became extremely useful instruments to chemists, molecular biologists and the like. Eventually, a burgeoning industry developed around these instruments and the commercial demand for more and more efficient systems drove research in this area. Today, high precision mass spectrometry has become a billion-dollar industry, with a vast and expanding market in the biomedical and pharmaceutical sectors.

Fig. 1.1 The quadrupole ion beam guide (*left*) and the quadrupole ion (Paul) trap (*right*).

It was in the early 80's, around the time of Dehmelt's work, that new technologies expanded considerably the possibilities of using Paul and Penning traps. These technologies were primarily those of ultra-high vacuum systems, which allowed long storage times of samples in very pure environments, very stable high-field superconducting solenoids, which allowed extremely precise measurements of the properties of the stored ions, and, last but not least, the development of powerful microcomputers that could manipulate the parameters of the traps and observe the signals induced by ion motions at time scales that were not possible by mere human control.

This led not only to new possibilities for the use of electromagnetic traps as devices in their own right but also to the possibility of integrating traps into complex systems. For example, modern Paul traps are often used in chemical studies of molecules by operation in three stages; mass filtering, collisional induced dissociation of the filtered molecular ions by exciting them in the presence of a background gas, followed by mass analysis of the collision fragments. Typically, the whole sequence of operation takes less than a tenth of a second. Thousands of commercial instruments today employ a similar sequence of operation but use three separate radiofrequency mass filters in tandem. An extreme example of this type of ion manipulation is the ISOLTRAP facility in CERN [Bec89][Moo92][Rou92], in which high accuracy mass measurements on radioactive nuclei are made through a series of 6 sequential operations, involving three separate ion traps, on a 60keV ion beam of the radionuclides of interest. These 6 operations are repeated at up to 5 sequences per second.

Such complex systems require an extensive knowledge of the physics governing the ion ensemble and its manipulation so that they can be engineered for high performance. It is this scientific and economic environment of modern mass spectrometry that motivated the work of this thesis.

1.1 Overview of Dynamic Mass Spectrometers

Mass spectrometers refer to any class of instrument whose function is to separate atoms, ions and molecules according to their mass. In the early 1900's, these mass spectrometers were nearly all static devices that used magnetic fields to deflect ion paths and thus separate ions of different charge-to-mass ratios (m/z). By the 1950's, there was increased interest in a new breed of instruments, the dynamic analyzers, which employed time-varying electric fields to separate ions based on the time dependence of one or more of its system parameters. Blauth [Bla66] suggested that these dynamic analyzers could be further subdivided into three categories: energy-balance spectrometers, time-of-flight (TOF) spectrometers and path-stability spectrometers (Table 1.1). Of the three subcategories, the quadrupole ion beam guide and the quadrupole ion trap fall into the third group.

Energy-balance mass spectrometers refer to the class of instruments that employ time-varying fields in order to create a resonant condition. Under these conditions, the apparatus would be able to selectively deliver more energy or withdraw energy from the ions that meet the resonant criteria. In either case, the resonant ion exhibits the largest energy exchange with the time-varying fields and by using an energy analyzer, that resonant ion can be separated and detected.

Time-of-flight systems are perhaps the most straightforward in terms of basic operation. These systems are based on the principle that ions with different masses but having the same energy and starting off at the same time and place, will arrive at a detector, positioned at a specified distance away, at different times relative to the start time. Thus, by measuring the time of flight of these ions, a mass spectrum can be built up and the different times will have corresponded to different m/z values. Time-of-flight mass spectrometers will be discussed in more detail later on.

Path-stability spectrometers operate by using the time-varying fields to create stable and unstable paths in the system. These paths themselves are m/z dependent and so only ions that have a mass within a certain range will be able to traverse the system. By tuning the fields, the stability condition can be narrowed to the point where only ions within a very small range of mass will be accepted, thus making it a very selective mass spectrometer. Again, the quadrupole systems are part of this category of spectrometers and will be discussed in greater detail later.

Basic Ion Motion		Linear Direct	Linear Periodic	Circular Periodic
Energy-Balance Spectrometers	Acceleration	1. Beckman spectrometer 2. Bennett spectrometer 3. Boyd spectrometer 4. Redhead spectrometer 5. Topatron	1. Palletron spectrometer 2. Bierman spectrometer 3. Mass filter 4. Double-well spectrometer	1. Omegatron
	Deceleration	1. Hare and Margetts spectrometer		1. Deceleration cyclotron 2. Deceleration Omegatron
Time-of-Flight Spectrometers	Without Phase Relations	1. Stephens spectrometer 2. Ion Velocitron 3. Keller spectrometer 4. Wolf-Stephens spectrometer 5. Wiley-McLaren spectrometer 6. Katzenstein-Friedland spectrometer	1. Linear periodic time-of-flight spectrometer with slot electrodes	1. Chronotron 2. Circular periodic time-of-flight spectrometer without magnetic field 3. Trochoid time-of-flight spectrometer
	With Phase Relations	1. Glenn spectrometer 2. Le Poole spectrograph 3. Carre-Margoloff spectrometer	1. Tempitron 2. Alikhanov spectrometer	1. Mass synchrometer 2. Hipple-Thomas spectrometer (E variable)
Path-Stability Spectrometers	Velocity Stable	1. Smyth-Mattauch spectrometer 2. Elings spectrometer	1. Reflektron	1. Falk-Schwering spectrometer
	Phase Stable	1. Phase-Stability spectrometer 2. Rotating-Field spectrometer	1. Farvitron 2. Slot spectrometer	1. Circular periodic phase-stability spectrometer
	ω_c Stable	1. Monopole spectrometer 2. Bauer spectrometer	1. Quadrupole mass filter 2. Ion cage	

Table 1.1 Table of dynamic mass spectrometers (Blauth [Bla66]).

1.1.2 Mass Filters and Transform Spectrometers

From a functional point of view, these mass spectrometers can be categorized in another fashion as two basic types. The older and more established type comprise of the mass filters which at any one instant in time are set to favor the transmission of an atomic or molecular species of a particular mass. The most important examples in modern mass spectrometry are the magnetic sector spectrometers and the radiofrequency quadrupole mass filters, in which the transmission of a particular mass is favored by tuning an azimuthal quadrupole electric field. By varying the parameters of these instruments the mass spectrum of the source material is scanned for the presence of peaks in the spectrum one mass at a time. The presence of a particular atomic or molecular species in a sample of material is detected by the presence of a peak rising above the background, the quantity of the species being determined from the area under the peak and, if necessary, the mass of an unknown species being determined from the position of this peak in the spectrum.

The second basic type of mass spectrometer, which recently has come into wider use, is that in which a whole ion collection is manipulated in such a way that each mass species within the collection yields a signal specific to that mass. Such mass spectrometers are commonly referred to as "transform" spectrometers, an example being the modern Fast-Fourier Transform Ion-Cyclotron Resonance (FT-ICR) spectrometer, in which all the ions in a collection in a Penning trap are simultaneously excited into cyclotron motion. The cyclotron motion of each ion species then yields a signal, indicating the presence of that species within the ensemble. The power of such a transform technique is shown by the fact that the mass species within an ion ensemble can be resolved to one part in a million with only one thousand ions in the collection [Nib86][Nie99].

In this sort of classification, the TOF spectrometer falls into the category of the transform type. In essence, the times at which the various masses arrive at the detector is transformed into a mass spectrum. While this form of spectrometer does not approach the resolving power of the FT-ICR, it has been demonstrated that it can achieve resolving powers of several tens of thousands. Furthermore, it is considerably less expensive than FT-ICR systems and it can be used on ions with mass to charge ratios up to a hundred times greater than that which can be handled in FT-ICR. This is of special importance in modern biomedical research where molecules of interest, such as proteins, can have atomic masses of several hundred thousand Daltons.

A central feature of transform mass spectrometers is that all of the ions are observed, not as in the filter spectrometers where the only observed ions are those selected by the filter. The advantage of transform type mass spectrometers therefore lies in their great sensitivity, none of the ions in the collection are wasted.

On the other hand, transform spectrometers require that the material under examination be prepared as an ion collection. In the case of the FT-ICR spectrometers, this is usually accomplished by introducing the sample material into the trapping volume as a gas and ionizing this gas by a pulse of high-energy electrons. In the case of TOF spectrometers, the current method of choice is the ionization of the sample, collected and prepared on a suitable solid substrate, by a high-energy short-duration laser pulse in a vacuum [Cot94][Cot95].

It is here that the transform spectrometers suffer in comparison to the filter spectrometers, where all that is required is that the ions be delivered in a somewhat steady stream. This is particularly true for one of the widest applications of mass spectrometers in bioanalytical research, where the mass spectrometer is used to analyze the output of a High-Performance Liquid Chromatogram (HPLC). In this application the change in the mass spectrum as the various biomolecules pass through the HPLC is used as a signal of the presence of a particular molecular species. Here the material under investigation is rendered from the liquid phase to the gaseous phase, and ionized, by spraying it into a high electric field in atmosphere, whereupon the resulting ions are delivered through an orifice into the vacuum of the mass spectrometer. The result is a

relatively steady ion stream, most suitable for the filter type of mass spectrometer. Thus, whereas filter mass spectrometers are wasteful of the ions that are delivered to them, they can make use of ion sources that are much more efficient in ionizing the material available for analysis.

However, recent developments have shown that high-efficiency steady-flow ion sources can be adapted to transform mass spectrometry. This is accomplished by using a radiofrequency ion guide to cool an incoming ion beam and collect the ions of the beam in an electric trap, referred to by its inventor D. Douglas, as a "linear RFQ trap", formed at the end of the guide. The ions collected in this trap can then be extracted as a bunch for delivery to a transform spectrometer. Such a scheme is part of the ISOLTRAP facility at ISOLDE at CERN, mentioned previously, where incoming continuous beams of ions are collected and delivered as bunches to an ICR type Penning trap mass spectrometer. Overall collection and delivery efficiencies have been estimated to be as high as 20% [Her00]. The power of this system is shown by its use in a recent measurement of the mass of the highly radioactive Argon-33 isotope, which has a half-life of only 133ms. An accuracy of better than one part in 10 million was obtained using only several thousand Argon-33 ions.

The implementation of such a strategy to a TOF mass spectrometer presents a very interesting and attractive application. However, such an approach requires careful study of the dynamics of the ions collected in a linear RFQ trap. This is because of the extreme time requirements placed on the delivery of the ions to a TOF spectrometer compared to a Penning trap spectrometer. Whereas delivery to a Penning trap spectrometer can be made over time intervals of up to several microseconds, in modern TOF mass spectrometers, which achieve their resolutions through very narrow time focusing, the delivery must be made in intervals of the order of 10 nanoseconds. The feasibility of achieving such a time focusing of the extracted ions from a linear RFQ trap requires study of the dynamics of the ion ensemble within the trap.

In this respect, the use of a linear RFQ trap as an ion source for TOF mass spectrometry is like that of the modern complex systems mentioned in the introduction. Its implementation requires careful study of the physics of the system so that the necessary ion manipulation, and the apparatus to achieve it, can be engineered. The physics of the tandem linear RFQ trap-TOF mass spectrometer combination is the subject of this thesis.

1.2 Literature Review of Tandem Mass Spectrometer/Time-of-Flight Systems

The tandem mass spectrometer/Time-of-Flight system (TOFMS) is a relatively new development in precision mass spectrometry. The following is a brief review of some of the systems reported by other researchers.

Ion Trap Storage/Time-of-Flight Mass Spectrometers (IT/TOFMS)

One fairly successful technique of matching a quadrupole system to a Time-of-Flight mass spectrometer is the use of a Paul trap as the ion source for the TOF system. Among the researchers that have worked on this type of system are a group led by Lubman et al. in Michigan, another group in Würzburg, Germany led by Grotemeyer et al. and Moore and Ghalambor-Dezfuli at McGill University. Lubman has reported on many experiments carried out on this hybrid system, showing the power and versatility of the device. He quotes having achieved a mass resolution of approximately 1500, while showing the adaptability of the ion trap system by introducing different methods of ionization, viz. photoionization [Lub92], electrospray and microelectrospray [Wu96], in combination with liquid chromatography or capillary electrophoresis techniques [Qui96] as well as a Plasma source API [Lub93].

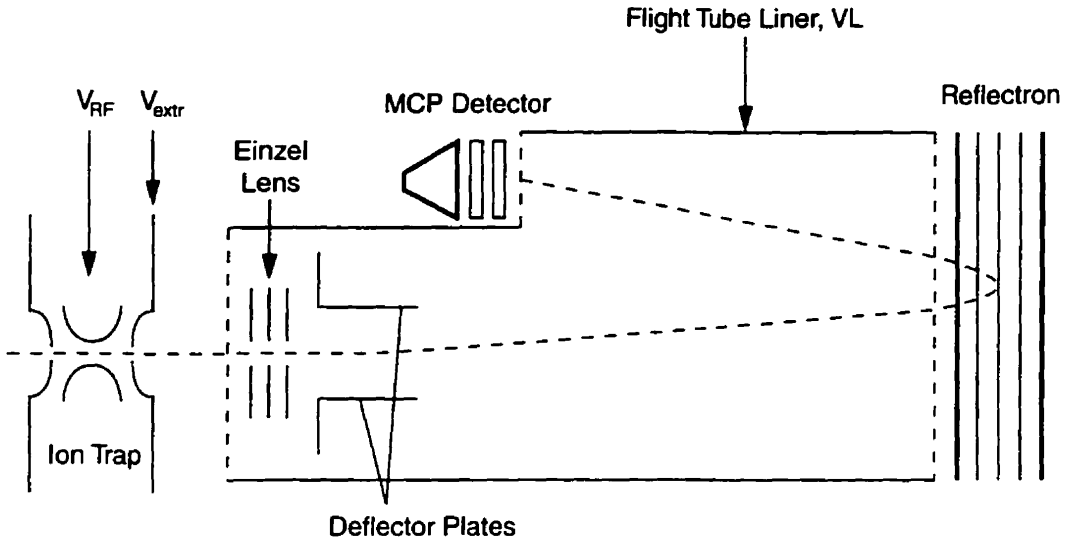

Fig. 1.2 Schematic diagram of the Ion Trap/Time-of-Flight mass spectrometer.

Grotomeyer's group also reported great success with the ion trap/Time-of-Flight system but also studied in detail the problem of using an ion trap as a device to collect a continuous stream of ions and inject them as a pulse into a TOF system. The RF motion of the ions in the ion trap, produced by the time-varying fields in the axial direction, caused the spectrometer performance to be highly sensitive to the RF phase at which the ions were pulsed into the TOF analyzer [Gro96][Gro96a]. Ghalambor-Dezfuli also reported similar results, indicating that the injection and ejection of ions in the Paul trap was highly dependent on the RF phase, limiting the time window for each procedure to only a few degrees of RF phase [Gha96].

These results pose a severe problem for a TOF system designed to handle a wide range of masses simultaneously. This is because the time window for extraction that results in good resolution in the TOF spectrometer is different for each mass. Thus for the extraction of a given collection, high resolution can only be achieved for the one particular mass for which the extraction is optimized.

Quadrupole Beam Guide/Time-of-Flight Mass Spectrometer (Q-TOFMS)

Earlier work with orthogonal extraction into a TOF spectrometer by Standing et al. [Sta94] led them to develop a tandem quadrupole ion beam guide/orthogonal Time-of-Flight mass spectrometer [Che97][She97]. In this system the ion beam flowed from the beam guide into a region where discrete segments of the beam were pulsed orthogonal to the beam axis into the TOF spectrometer. This method of beam pulsing was more effective than the quadrupole ion trap in that it avoided the problems of RF phase dependent performance, since along the beam axis, there is no RF field to modulate the ion motion.

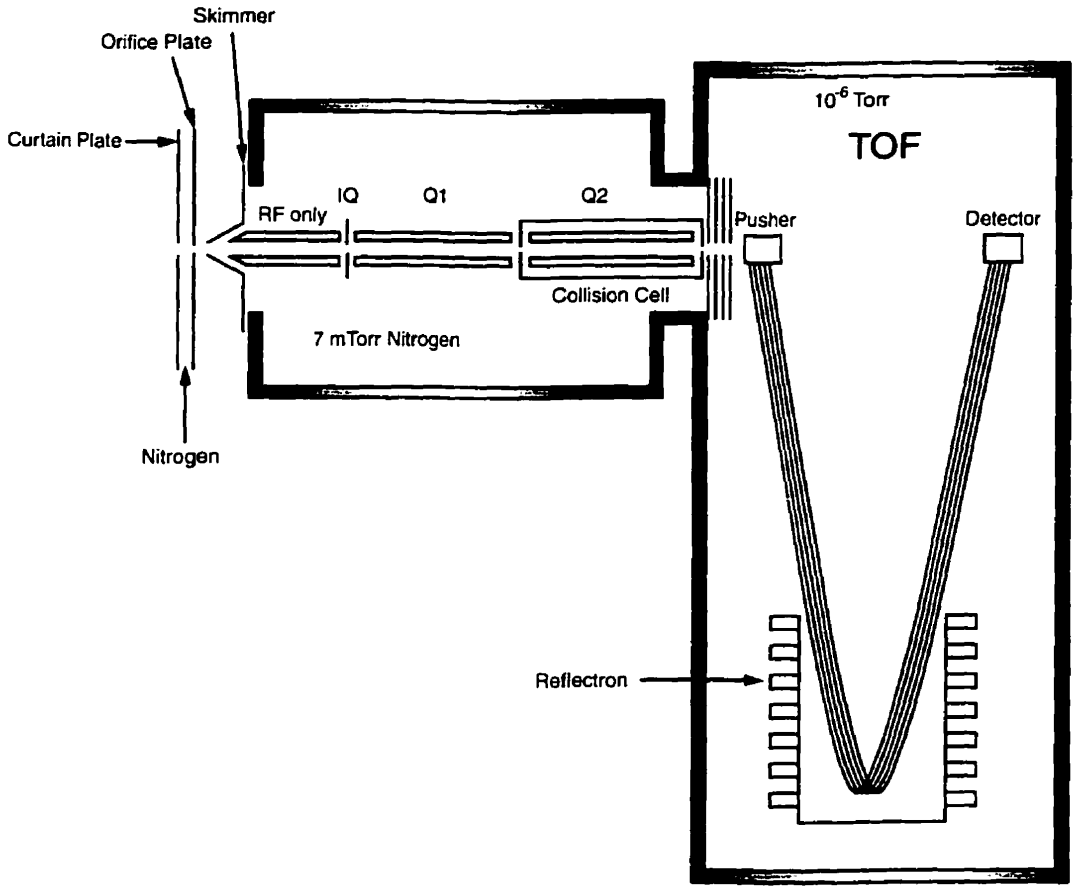

Fig. 1.3 Schematic diagram of MDS SCIEX's QqTOF system.

The success of this type of instrument speaks for itself. Early reports indicated mass resolutions in excess of 5000 for measurements of peptides and proteins (1000 – 6000 Da) using as little as femtomoles (10^{-15}) of sample [Hop99][Che99]. The system has since been adopted by commercial manufacturers MDS SCIEX and Micromass Ltd. as part of their line of high precision mass spectrometer products [Mor96][Che99a].

However, impressive as this performance is in terms of femtomoles of sample, the number of molecules used is still of the order of 1 billion, whereas TOF mass spectrometers typically process less than 100,000 ions for a full mass spectrum. Thus with efficient delivery of the available material to the TOF spectrometer, there could still be a gain of several thousand in sensitivity of the instrument.

Linear Ion Trap/Time-of-Flight Mass Spectrometer (LIT/TOFMS)

A further modification to the ion beam guide/Time-of-Flight system was to alter the quadrupole rod system into what Douglas referred to as a linear ion trap (LIT). The LIT was used to trap and hold the ions between pulses of the time-of-flight extraction so that there would be an overall improvement in duty cycle. In addition to increasing the duty cycle, the LIT delivers a higher density, slower axial energy beam into the pulsing region so that the sensitivity of the spectrometer is enhanced. Finally, by trapping the beam in a buffer gas environment, the ions are forced to cool radially, thus producing a narrower beam into the time-of-flight system and improving the resolution of the mass spectrum [Dou98].

However, even this system is very wasteful of the ions delivered by the ion beam guide and a system which collects these ions in a well defined region in space from which they can be extracted into a TOF system would present considerable advantages in overall sensitivity.

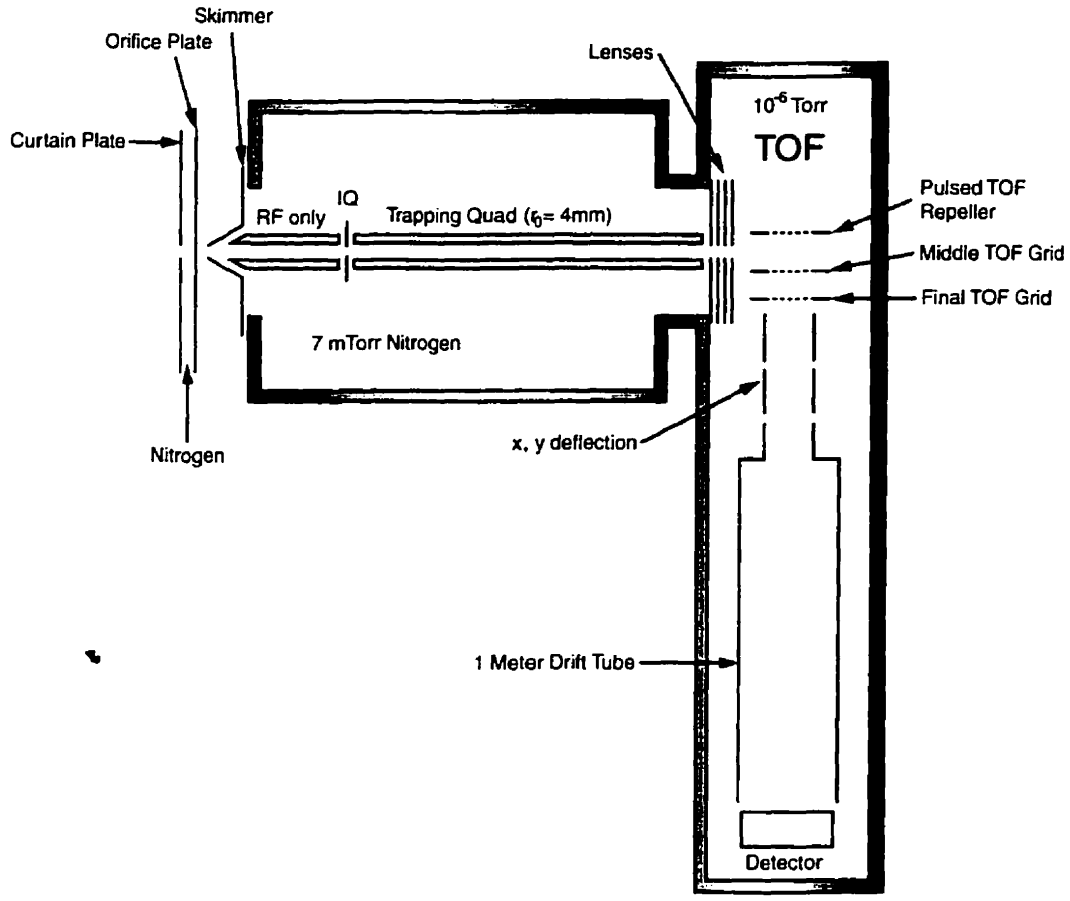

Fig. 1.4 Schematic diagram of the Linear Ion Trap Time-of-Flight mass spectrometer.

In summary, none of the present systems using RFQ fields to prepare an ion collection for TOF mass spectrometry have met the full potential of the TOF system. This is because the spatial and momentum distributions of the ions that are collected are not ideal for delivery to the spectrometer. What indeed are the ideal spatial and momentum distributions for TOF mass spectrometry and can a linear RFQ trap provide collections with these characteristics?

1.3 Basics of Time-of-Flight Mass Spectrometry

To understand the basics of TOF mass spectrometry and the ion collections needed for it, consider an idealized collection of ions with unit charge which occupy an extent Δz in the direction of the axis of a TOF analyzer and which has a momentum spread Δp_z in that direction (i.e. from $-1/2\Delta p_z$ to $+1/2\Delta p_z$). This distribution occupies a simple rectangle in the $z - p_z$ action space, as shown in Fig. 1.5.

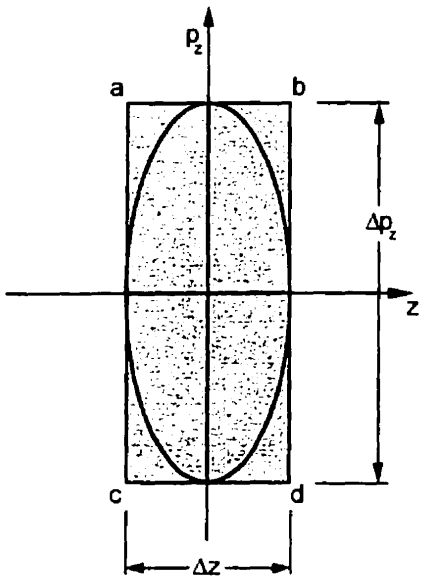

Fig. 1.5 The action diagram of a simple collection of particles occupying an axial extent Δz and having a momentum spread of Δp_z. For reference, the corners of the rectangle have been labeled *a, b, c, d.*

Now suppose that a uniform electric field **E** in the z direction is applied to this collection and that this field extends to a distance z_o where the ions are allowed to pass through a grid into the field free region of a TOF mass spectrometer. Furthermore, assume that the momentum gained by the acceleration of the particles in this field is considerably greater than their momenta before the field was applied. Elementary mechanics of uniform acceleration over a specified distance show that immediately after entry into this field free region the rectangle representing the ion distribution transforms

into a parallelogram in energy-time coordinates, where the energy coordinate is the axial kinetic energy of a particle upon entering this region and the time coordinate is the time at which that particle enters the region. This parallelogram is shown in Fig. 1.6

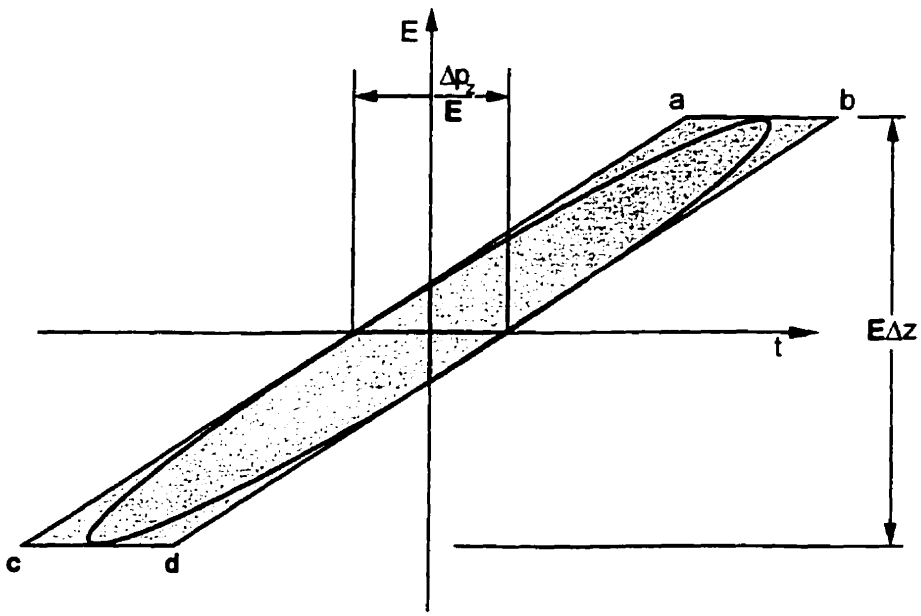

Fig. 1.6 The action diagram, in *E-t* coordinates, of the ion collection of Fig. 1.5 upon being accelerated into a field free region.

It can be seen that the area of this parallelogram is the same as that of the momentum-space rectangle of the original collection.

Now consider what happens to this distribution as the ions penetrate into the drift field region. The high energy particles, which initially lagged behind the low energy particles (the parallelogram is tilted to the right), catch up and the parallelogram quickly turns into a rectangle (Fig. 1.7), preserving its area as it does so. Again, elementary mechanics will show that this occurs at a distance from the grid that is twice the distance of the grid from the initial collection. At this point the ion ensemble is said to have come to a "time focus", a fixed location in space where all the ions arrive within the shortest possible time interval, i.e. $\Delta p_z/\mathbf{E}$. Although this time focus will occur at the same position for all masses, the time at which ions arrive at this focus will depend on their mass.

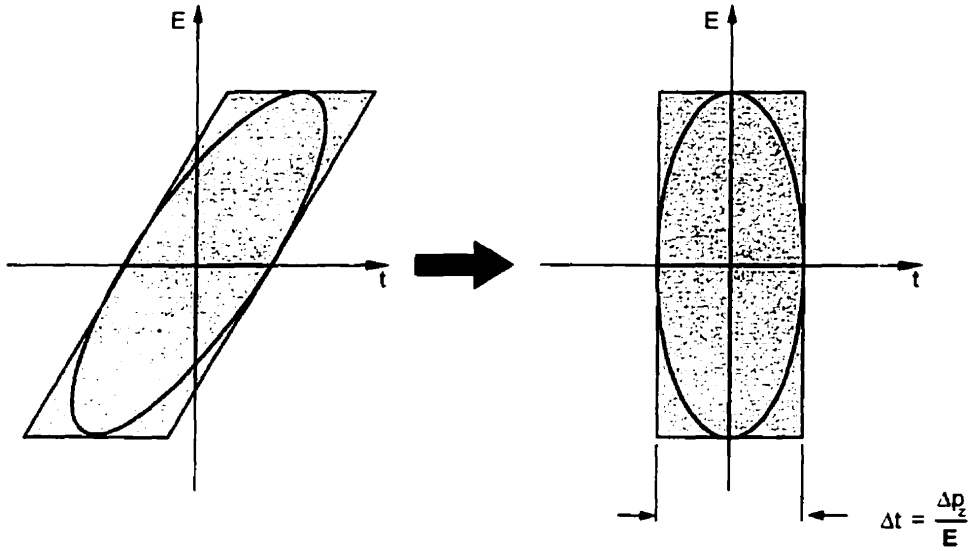

Fig. 1.7 The *E-t* action diagram of the ion collection of Fig. 1.5 after having drifted to its time focus.

The significance of this action diagram can be seen in its time evolution as the ions pass through a modern TOF spectrometer. The ion collection is first allowed to drift undisturbed for a specified distance, which can approach up to a meter. At this point, the action diagram then becomes an elongated parallelogram that is sharply tilted to the left, as shown in Fig. 1.8

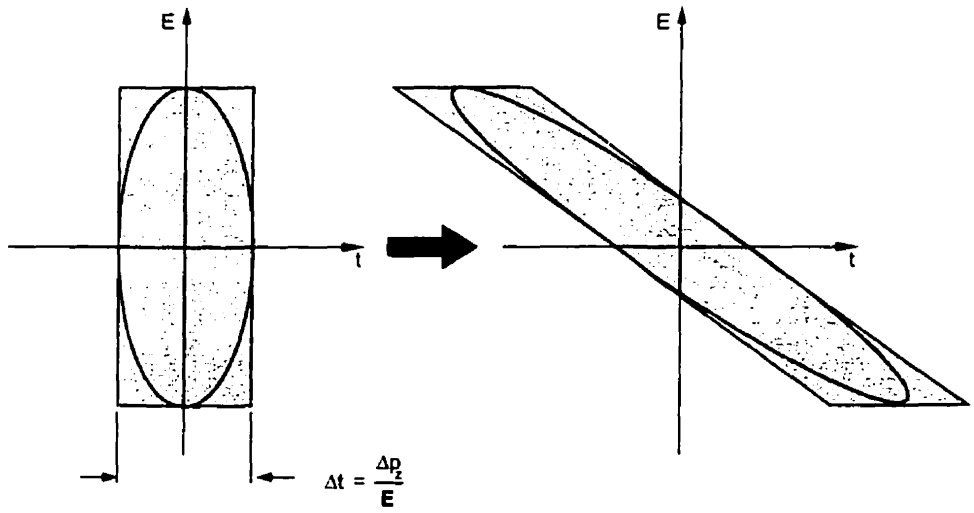

Fig. 1.8 The *E-t* action diagram of the ion collection of Fig. 1.7 after having drifted past its time focus.

At this point, the spread in the time of arrival of the collection is determined largely by the energy spread of the ensemble rather than its time spread at the time focus. However, in a modern TOF spectrometer the collection is not detected at this point but rather enters a region with a decelerating electric field sufficient to reflect the ensemble backwards at an angle relative to its original direction which is only sufficient to allow the insertion of a detector beside the original time focus (Fig. 1.9).

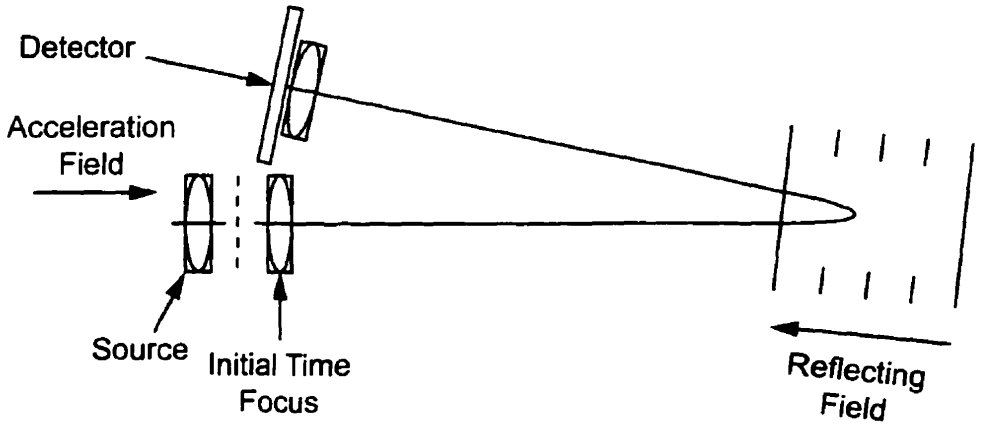

Fig. 1.9 Schematic diagram of a reflecting TOF mass spectrometer.

This reflecting field reverses the action parallelogram so that it is again tilted to the right. By the appropriate adjustment of the reflecting field, this new parallelogram can be made to be just a mirror image of the action diagram of the ensemble upon entering the reflecting field (Fig. 1.10).

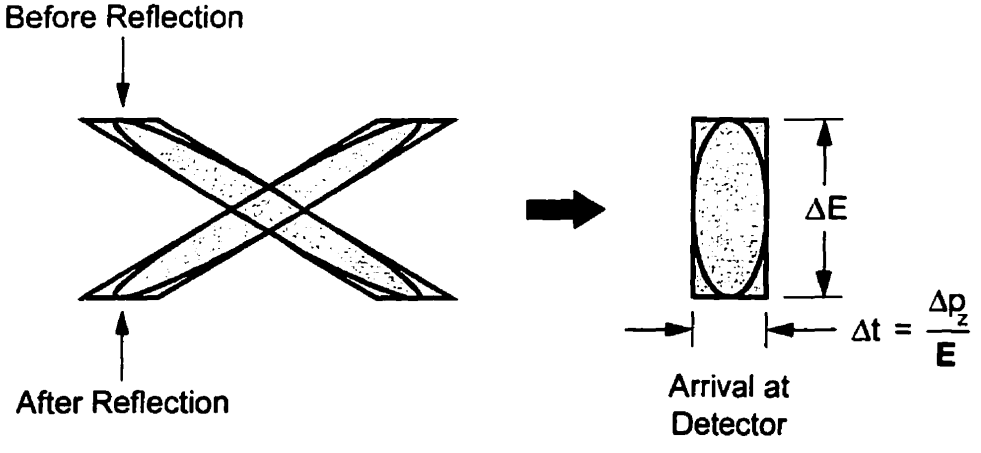

Fig. 1.10 The *E-t* action diagram of the ion collection of Fig. 1.8 after being reflected and allowed to drift to a new time focus.

The ion ensemble can now be allowed to drift to a new time-focus that, because of the symmetry of the configuration, will be the same as that of the original at the spectrometer entrance. Thus the reflection acts as a converging mirror with a source and an image of that source at equal distances. In such a configuration the time width of the source and the focus will be identical.

Again, while all of the ions will be brought to a time-focus at the same point, i.e. at the detector, the time at which this focus occurs will depend on the mass of the ions. Because the drift time t is proportional to the square root of the ion mass m, the mass resolving power R, defined as the mass m divided by the mass resolution Δm, will be half the time resolving power:

$$R = \frac{m}{\Delta m} = \frac{1}{2}\frac{t}{\Delta t} = \frac{1}{2}\frac{t|\mathbf{E}|}{\Delta p_z} \tag{1.1}$$

This relationship can be expressed in terms of the parameters of the mass spectrometer and the ion source by noting that the energy spread of the ions ΔE is $\mathbf{E}\Delta z$ and that $\Delta p_z \Delta z$ is the area A_z of the action diagram for the z direction within the source. The mass resolving power then becomes

$$R = \frac{1}{2}\frac{t\Delta E}{A_z} \tag{1.2}$$

The numerator in this relationship is determined by the spectrometer design. Thus the longer the time it takes for the ions to traverse the spectrometer and the greater the energy spread of the ions that can be accommodated by the spectrometer, the greater the resolution. On the other hand, the denominator in this expression relates solely to the properties of the ion source. Thus, for a given drift time and energy spread of the extracted ion collection, the mass resolution is simply inversely proportional to the area of the axial action diagram of the source.

The importance of action diagrams of the ion source extends to those for the transverse directions as well. The extent of the transverse displacement of ions from the axis and the extent of their transverse momenta determine the feasibility of containing the ions within the flight tube and focusing them onto the detector.

Thus the suitability of an ion source for TOF mass spectrometry and, if applicable, the design of an optimum time-of-flight system to utilize that source depend critically on the action diagrams of the source. As discussed in the theory section to follow, these diagrams are orthogonal projections of the ion ensemble in a 6-dimensional momentum-displacement coordinate system referred to as "phase space". This thesis is therefore a study of the phase space distribution of ions in a linear RFQ trap, with the goal of determining how such a trap can be integrated into a TOF system for high-sensitivity high-resolution mass spectrometry.

1.4 Methodology of this Study

In general the phase space distribution of a collection of particles is impossible to obtain from direct measurements of the spatial and momentum coordinates. This is because it is not feasible to observe these coordinates directly. Rather, the whole ensemble must be manipulated in some controlled fashion so that a particular aspect of the distribution can be detected. The parameters of this manipulation are then varied so that the collection can be "viewed" from different aspects.

In the case of the linear RFQ trap, the manipulation chosen to probe the phase space distribution was that of suddenly extracting the ion ensemble and observing the distribution in the times of arrival at the detector; essentially a TOF system itself but not one designed to be a mass spectrometer but rather an "action diagram microscope". A trap, here referred to as LTRAP, was designed and built specifically for this purpose. The variation of this distribution with different extraction fields was then recorded. The distribution of the axial action diagram of the confined ions was then deduced from these observations by setting up a model of this action distribution and using computer simulations to determine what such a model would produce as a time distribution at the

detector for the various extraction fields. The parameters of this model were then adjusted until a satisfactory simulation of the observed distributions was achieved.

In this way models of the ion distributions were established for various operating parameters of the trap. These models then showed how the trap should be designed for operation with a high-resolution TOF mass spectrometer.

It should be noted that the work of this thesis follows the methodology used by D. Lunney [Lun92] and M. Ghalambor-Dezfuli [Gha96] in their studies of the phase space distributions of ions in a Paul trap and more details of the methodology can be found in the references to their work.

1.4.1 Description of the LTRAP system

The hybrid Linear RFQ Trap/Time-of-Flight spectrometer that was built and tested in this study comprised of a linear ion trap much like the one used by Douglas, and was coupled axially to a time-of-flight mass spectrometer like that of Lubman et al. The purpose of designing such an apparatus was to have a system capable of investigating the thermodynamic properties of the ion ensemble within the LTRAP system in order to understand the behavior of the ensemble in terms of phase space variables. As already implied, and discussed more fully in the theory section, phase space is the representation of choice for considering the evolution of a collection of particles in a region where the fields and potentials are well defined. This is, of course, the case of an ion ensemble within the LTRAP system and therefore discussions about the physical characteristics of these ensembles will most naturally be referred to in their phase space representations.

In Chapter 2, the theory governing the motion of ions in radiofrequency quadrupole devices will be discussed, as well as the general principles of phase space dynamics and the underlying thermodynamic model that relates it to ion temperature. A brief summary of the application of such concepts to TOF mass spectrometry will also be presented.

Chapter 3 will discuss the actual apparatus and its various components, detailing design considerations and methods of ion detection, in order to gain a better understanding of how the ensemble's phase space properties are detected and measured. The analysis of the experimental data required extensive computer analysis as well as detailed computer simulations, which will be outlined in Chapter 4. Finally the results of this study will be presented in Chapter 5 and Chapter 6 will conclude the thesis with suggestions for how the results of this thesis can be used in designing a working TOF mass spectrometer based on a linear RFQ trap as a source.

1.5 Contributions of this Thesis

- A new hybrid Linear RFQ Trap/Time-of-Flight mass spectrometer was developed and tested.

The LTRAP system was the first system to be designed with the express purpose of analyzing the phase space characteristics of a linear ion trap and determining the performance that can be expected of a TOF mass spectrometer when such a trap is used as its source. The unique features in the design of LTRAP include a segmented quadrupole rod system that has independent control of both RF and DC voltages on each electrode, a fast ion extraction method from the LTRAP system through the pulsing of certain trap electrodes and its adaptation to a standard TOF system whose axis is collinear to the ion beam guide.

- A theoretical model for the phase space distribution of confined ion ensembles in the linear trapping quadrupole beam guide (LTRAP) was developed, based on the Boltzmann distribution.

The theoretical model developed in this thesis is unique to the LTRAP's method of operation, detailing the concepts involved in ion manipulation of this sort from a phase space approach. The RF confining fields of the system were expressed in terms of a pseudopotential well model which was then combined with the DC axially trapping field to create a representation for the fully confining 3 dimensional trapping potential. This then allowed the ion ensemble to be characterized in terms of both spatial and momentum distributions in this confining field, thus giving a clearer understanding of the phase space behavior in the system. The power of the model lies in the fact that the ion behavior in LTRAP and in the Time-of-Flight system has been related to one single quantity, the temperature of the ion ensemble, so that all phase space distributions are determined by this one quantity.

- A SIMION© simulation was developed to run in conjunction with C-based programs to model the ion behavior in the trapping, cooling and pulsing process. The temperature of the trapped ion ensemble was established through this simulation.

In order to properly analyze the experimental data, it was necessary to develop a computer simulation based on the theoretical model that could recreate the ion behavior at every stage inside the system. The computer simulations recreated the true experimental conditions as closely as possible in terms of trapping and pulsing processes, and the only parameter that could be varied was the ion temperature. The experimental results were then compared to the results predicted by the computer and the temperature of the ion ensemble was defined as the temperature at which the simulation gave the best fit to the experimental results.

- A phase space reconstruction algorithm based on the Fourier slice projection theorem, was implemented to use actual experimental data to "image" the phase space distribution of the confined ions in the LTRAP system.

First suggested by D. Lunney [Lun92], the Fourier slice theorem was used to tomographically "image" the phase space density distribution of the ion ensemble in LTRAP using collected experimental data at various extraction voltages. It is the first time that such a technique has been used to reconstruct an ion distribution in phase space. It should be noted that this reconstruction does not depend on any adjustable parameters, such as the ion temperature. However, over the range of slices that could be obtained in the present work the precision of the reconstruction was not nearly as great as that of the thermodynamic model. It was therefore used as a confirmation that the thermodynamic model was indeed applicable.

Chapter 2 Theory and Background

This chapter will present the theoretical framework on which this thesis is based. The physics presented in this chapter will cover the theory of operation of the beam guide, the principles behind the cooling and collection of the ion cloud in LTRAP and the extraction and analysis of the ion pulse in the time-of-flight section. The subjects covered fall within the general principles of dynamic ion manipulation.

2.1 Principles of Dynamic Ion Manipulation

The goal of ion manipulation is to use static and dynamic electromagnetic fields to control all aspects of a charged particle's position, momentum and energy; making it possible to distinguish ions according to their mass, velocity or other observable characteristics. In this thesis, the magnetic aspect of ion manipulation will not be discussed, as it is not included in this work.

The basic concept of ion manipulation in purely electric fields is that all charged particles are accelerated in the direction of the electric field lines, positive ions toward lower electric potentials and negative ions toward higher potentials. The equation of motion for a charged particle under the influence of an electric field is then expressed simply as

$$m\ddot{\mathbf{x}} = e\mathbf{E} \tag{2.1}$$

where m is the mass, $\mathbf{x}$ is the position vector, e is the charge of the ion and $\mathbf{E}$ is the electric field vector at the point in space occupied by the ion. From Gauss' theorem, the electric field vector $\mathbf{E}$ must obey

$$\nabla \cdot \mathbf{E} = \frac{\rho}{\epsilon_o} \tag{2.2}$$

where ρ is the charge per unit volume and ϵ_o is the permittivity of free space

$$\epsilon_o = 8.85 \times 10^{-12} \quad \text{farad/m} \tag{2.3}$$

The vector $\mathbf{E}$ itself can be expressed in terms of the electric potential φ as

$$\mathbf{E} = -\nabla \varphi \tag{2.4}$$

From equation (2.1), it is seen that the simplest ion trap configuration is one where there is a charge center such that all electric field lines are radial to this center. In such a case, a potential minimum is set up at the charge center and an ion with some tangential velocity would orbit the center and be effectively trapped in space. This of course is the situation of an electron cloud around an atomic nucleus. However, such an electric field configuration does not form a useful trap since the center of the trap is already occupied by a charged object.

In the absence of any charge centers, equation (2.2) reduces to the familiar Laplace's equation

$$\nabla \cdot \mathbf{E} = 0 \tag{2.5}$$

In terms of the electric potential φ, Laplace's equation is

$$\nabla^2 \varphi = 0 \tag{2.6}$$

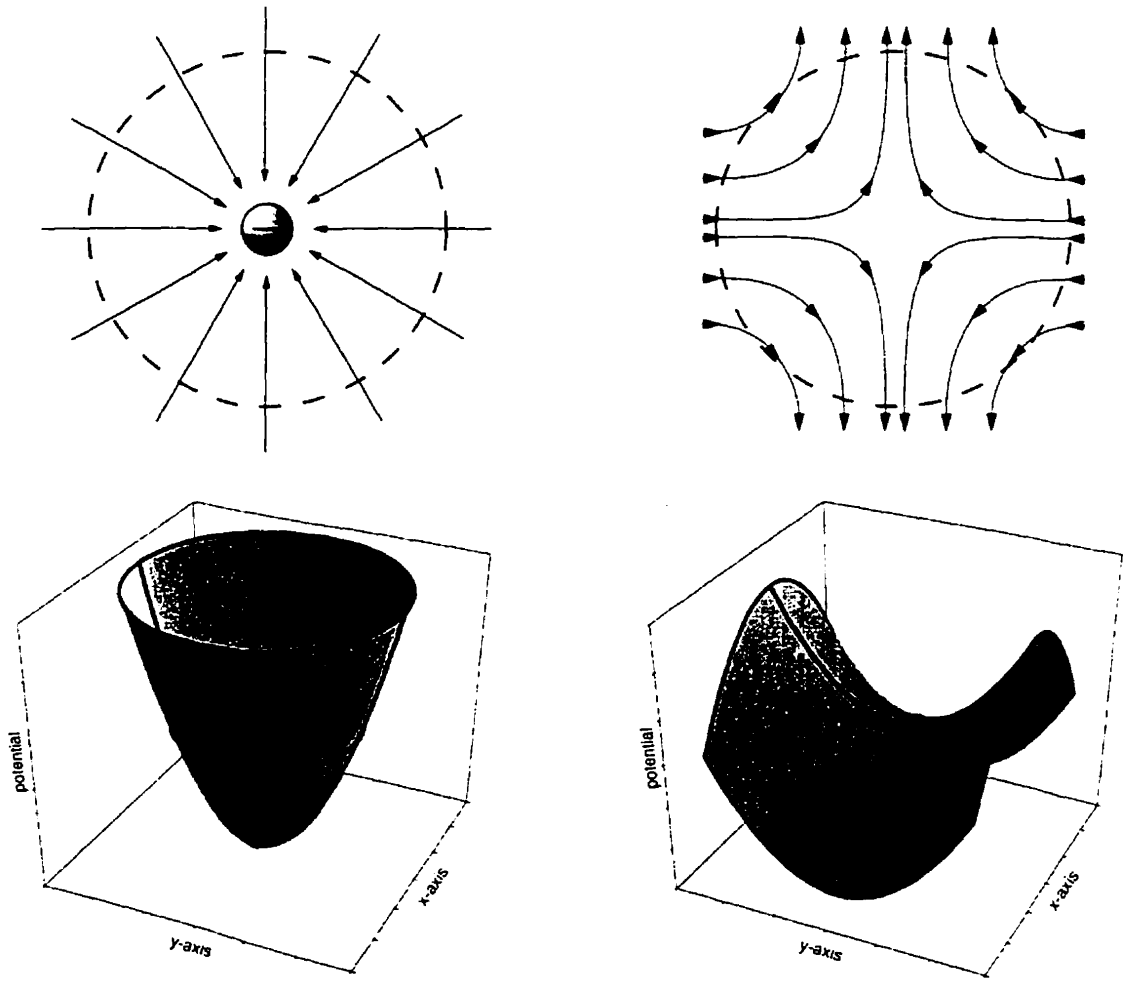

Fig. 2.1 Two examples of Gauss' law: *Left* – A central charge in a volume (*dashed*) forms radial electric field lines (*above*); creating a parabolic potential minimum (*below*). *Right* – In the absence of any charge, field lines entering a volume must also leave the volume (*above*); creating a potential minimum in one dimension and a maximum in another (*below*).

Unfortunately, Laplace's equation forbids the existence of a potential minimum in a vacuum. The equation forces the electric field lines to be conserved in such a volume, thus any field lines entering the volume must also leave the volume. If a potential minimum were created in one dimension, Laplace's equation dictates that this produces a potential maximum in at least one other dimension. (Fig. 2.1)

This inability to create a three dimensional electrostatic trap has led researchers to consider dynamic trapping devices, employing oscillating electric fields to achieve confinement. Of the many methods developed, the quadrupole trap and the quadrupole ion beam guide are the simplest and most elegant of systems for such confinement.

2.2 Quadrupole Ion Beam Guide

Quadrupole traps and quadrupole beam guides are able to trap and confine ions using oscillating electric fields. At any one instant in time, there is a potential minimum in one dimension and thus a potential maximum in an orthogonal dimension. This situation reverses itself after half a cycle of oscillation, when the minimum is turned into a maximum and vice versa. At certain frequencies of oscillation, the net effect of such a dynamically changing electric field results in an average confining potential in the center of the trap or beam guide. For ions the appropriate frequencies of oscillation occur at radio frequencies, hence the often used name Radio Frequency (RF) Quadrupole ion traps.

2.2.1 The Oscillating Quadrupole Field

Within the volumes of these traps, the potential φ must obey Laplace's equation, as seen in (2.6). Since a parabola is the mathematically simplest form of a potential minimum/maximum, it is useful to define a potential φ that is parabolic in all three spatial dimensions.

In Cartesian coordinates, this potential can be written as

$$\varphi = \varphi_o(\alpha x^2 + \beta y^2 + \gamma z^2) \tag{2.7}$$

which is the suitable form for the quadrupole beam guide. An analogous form for the potential can be cast in cylindrical coordinates

$$\varphi = \varphi_o(\rho r^2 + \sigma z^2 + \tau\theta^2) \tag{2.8}$$

which is associated with quadrupole ion traps such as the Paul trap. Note that the discussion that follows holds true whether in Cartesian coordinates or cylindrical coordinates, but for the purpose of this thesis, only the Cartesian system will be used, as it is the natural system for the ion beam guide.

Expressing the electric field **E** in terms of these coordinates leads to the following

$$\begin{aligned}\mathbf{E} &= -\nabla\varphi \\ &= -2\varphi_o(\alpha x\mathbf{i} + \beta y\mathbf{j} + \gamma z\mathbf{k})\end{aligned} \tag{2.9}$$

Now, applying the condition of Laplace's equation to such a quadrupolar field gives rise to restrictions on the values of α, β and γ

$$\alpha + \beta + \gamma = 0 \tag{2.10}$$

For an ion beam guide, the z-axis is chosen to be the beam axis and the confining fields are produced in the x-y plane. Therefore

$$\alpha = -\beta \quad \text{and} \quad \gamma = 0 \tag{2.11}$$

This reduces (2.7) and (2.9) to

$$\varphi = \varphi_o\alpha(x^2 - y^2) \tag{2.12}$$

$$\mathbf{E} = -2\varphi_o\alpha(x\mathbf{i} - y\mathbf{j}) \tag{2.13}$$

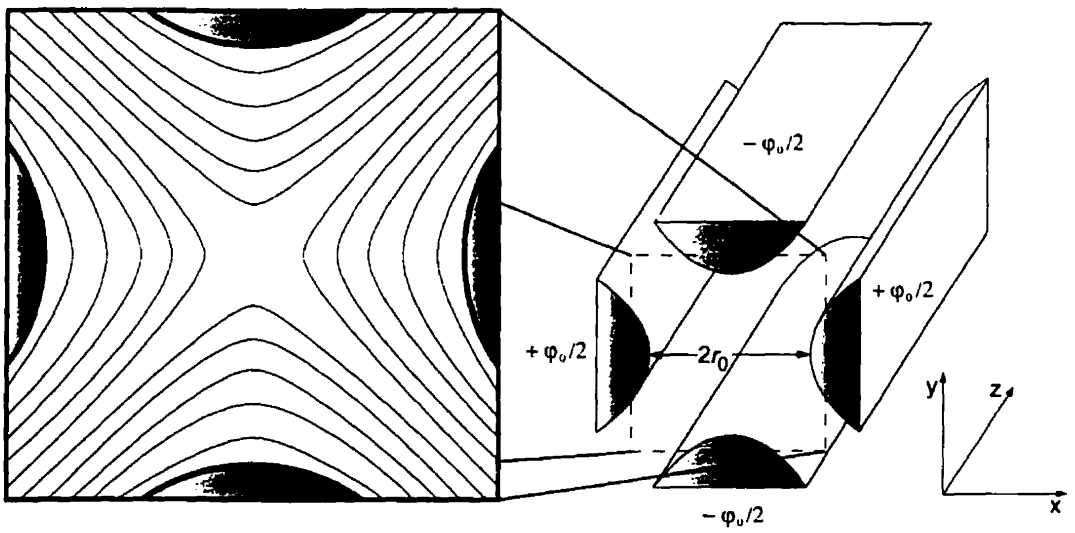

Fig. 2.2 Hyperbolic electrode structures required to generate the quadrupolar field. The equipotential field lines for such a configuration are shown in the inset $\varphi = \varphi_o\left(x^2 - y^2\right)/2r_o^2$.

Such a quadrupolar field can be created using four hyperbolic cylindrical rods arranged in such a way that their hyperbolic surfaces are along the equipotential lines in the x-y plane. (Fig. 2.2) In practice however, hyperbolic rod surfaces are not easily manufactured and so purely cylindrical rods are used instead. This introduces slight perturbations to the pure quadrupolar field but it has been shown that these are insignificant near the axis of the beam [Day54][Den71] and can be minimized with the proper selection of rod radius r

$$r = 1.148 r_o \tag{2.14}$$

where $2r_o$ is the minimum distance between opposing rods.

If the potential difference between neighboring rods is φ_o, then (2.12) becomes

$$\varphi = \frac{\varphi_o}{2r_o^2}(x^2 - y^2) \tag{2.15}$$

In order to achieve the oscillating quadrupolar field that is necessary to confine ions into a beam, all that remains is to allow φ_o to oscillate, which is most easily done in a sinusoidal fashion. In general, φ_o can have both an AC component and a DC component as well

$$\varphi_o = U - V\cos\omega t \tag{2.16}$$

where U is the DC voltage and V is the amplitude of the RF oscillation with angular frequency ω.

Inserting (2.16) into (2.12) and (2.13), the complete oscillating quadrupole field can now be expressed as

$$\varphi(x, y, t) = \frac{(U - V\cos\omega t)}{2r_o^2}(x^2 - y^2) \tag{2.17}$$

$$\mathbf{E} = \frac{-(U - V\cos\omega t)}{r_o^2}(x\mathbf{i} - y\mathbf{j}) \tag{2.18}$$

2.2.2 Equations of Motion – The Mathieu Equation

Given the function for the electric field **E**, the equation of motion for an ion of mass m and charge e can now be expressed as

$$\begin{aligned} \ddot{x} + \frac{e}{mr_o^2}(U - V\cos\omega t)x = 0 \\ \ddot{y} - \frac{e}{mr_o^2}(U - V\cos\omega t)y = 0 \end{aligned} \tag{2.19}$$

Performing a change of variables by defining two dimensionless quantities

$$a_u = a_x = -a_y = \frac{4eU}{m\omega^2 r_o^2} \tag{2.20}$$

$$q_u = q_x = -q_y = \frac{2eV}{m\omega^2 r_o^2} \tag{2.21}$$

and also expressing time in terms of a dimensionless quantity

$$\xi = \frac{\omega t}{2} \tag{2.22}$$

equation (2.19) now takes on the form

$$\frac{d^2u}{d\xi^2} + (a_u - 2q_u\cos 2\xi)u = 0 \tag{2.23}$$

where u is either the x or y coordinate.

Equation (2.23) is known as the Mathieu equation as expressed in its canonical form. This equation is actually a special case of a more general class of equations known as the Hill equations, where the oscillating component can have any form, not just sinusoidal.

The Mathieu equation has been discussed in many books concerning RF ion confinement, e.g. [Daw76], and only the solutions to the equation will be presented here:

$$u = \alpha' e^{\mu\xi} \sum_{n=-\infty}^{\infty} C_{2n}\, e^{2in\xi} \quad + \alpha'' e^{-\mu\xi} \sum_{n=-\infty}^{\infty} C_{2n}\, e^{-2in\xi} \tag{2.24}$$

where α' and α'' are integration constants depending on the initial conditions $u_o, \dot{u}_o$ and ξ_o. The constants C_{2n} and μ, however, depend only on the values of a and q and not on the initial conditions. Therefore, the nature of the ion motion is determined solely on the basis of its (a, q) value, regardless of initial conditions.

The solutions represented by (2.24) can further be divided into two sub-categories: stable and unstable, depending on the behavior of μ, which can be real, imaginary or complex. Stable solutions arise only when μ is purely imaginary such that $\mu = i\beta$ and β is not an integer. Integer values of β form a series of solutions which are periodic but unstable, called the Mathieu functions of integral order, and they form the boundaries in (a, q) space between the stable and unstable regions. In practice, only the first stability region $(0 < \beta < 1)$ is used for ion beam guides. (Fig. 2.3 and Fig. 2.4)

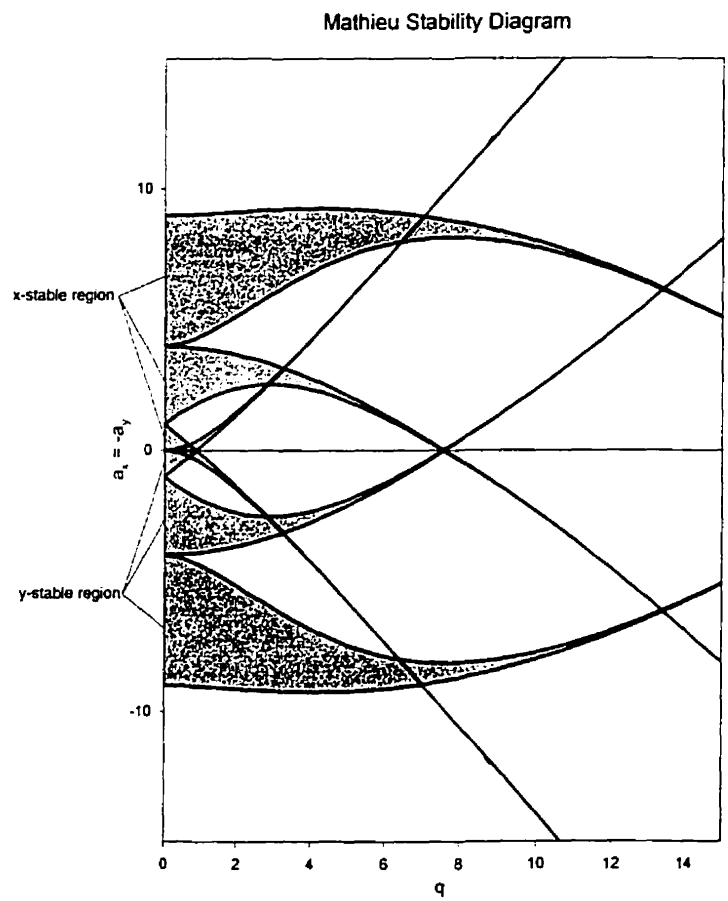

Fig. 2.3 The Mathieu stability diagram for the ion beam guide, showing the first 3 regions of stability in the x and y directions. Areas of overlapping gray represent simultaneous stability in both directions.

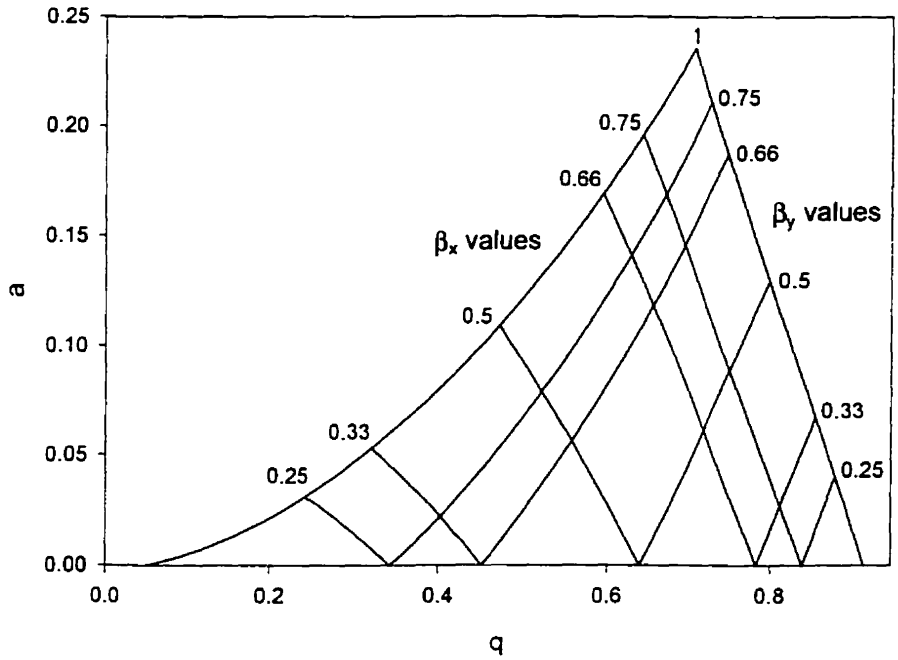

Fig. 2.4 First stability region of the Mathieu diagram. The iso-β curves are shown for stable x and y values.

Substituting $\mu = i\beta$ into (2.24) gives the equation of motion for stable ions

$$u = \alpha' \sum_{n=-\infty}^{\infty} C_{2n}\, e^{(2n+\beta)i\xi} \quad + \alpha'' \sum_{n=-\infty}^{\infty} C_{2n}\, e^{-(2n+\beta)i\xi} \tag{2.25}$$

which can be further simplified into

$$u = A \sum_{n=-\infty}^{\infty} C_{2n} \cos(2n+\beta)\xi \quad + \quad B \sum_{n=-\infty}^{\infty} C_{2n} \sin(2n+\beta)\xi \tag{2.26}$$

where

$$A = \alpha' + \alpha'' \quad \text{and} \quad B = i(\alpha' + \alpha'') \tag{2.27}$$

Equation (2.26) shows that the stable equation of motion is periodic with oscillation frequencies ω_n given by

$$\omega_n = (2n+\beta)\frac{\omega}{2}, \quad n = 0, 1, 2, 3, \ldots \tag{2.28}$$

For small values of β, only the low frequency terms are significant to the motion of the ion. The lowest term in the expansion (n = 0) is called the β-oscillation or macromotion oscillation. It is a large scale motion and has a frequency ω_o. For $\beta \leq 0.4$, the macromotion frequency can be approximated by

$$\omega_o = \frac{\beta\omega}{2} \cong \frac{q}{2\sqrt{2}}\omega \tag{2.29}$$

This macromotion can be thought of as an oscillation in a potential well created by the beam guide, referred to usually as the pseudo-potential. The higher frequency oscillations (micro-motion) can then be considered as perturbations on top of this large-scale motion of the ion. [Wue59][Deh67][Maj68][Daw76]

2.2.3 The Pseudopotential Well

Assuming that the total contribution of the higher frequency oscillations to the macromotion is small, the full motion of the ion in the beam guide can then be approximated by

$$u = \delta + \Lambda \tag{2.30}$$

where u is full motion of the ion in either the x or the y coordinate, δ is the micromotion oscillation and Λ is the large macromotion component.

Assuming that $\delta << \Lambda$ and $d\delta/dt >> d\Lambda/dt$, both variables can then be inserted into the Mathieu equation (2.23) to yield

$$\frac{d^2\delta}{d\xi^2} = -(a_u - 2q_u \cos 2\xi)\Lambda \tag{2.31}$$

Furthermore, if the ion guide is operated without any DC component, then $a_u = 0$. Integrating twice, (2.31) yields

$$\delta = -\frac{q_u \Lambda}{2}\cos 2\xi \tag{2.32}$$

This shows that the micromotion δ has the same frequency as the oscillating RF field, but its motion is 180° out of phase with it. It also has an amplitude proportional to the operating parameter q and increases with increasing macromotion Λ. Replacing this relation back into the definition of u gives

$$u = \Lambda - \frac{q_u \Lambda}{2} \cos 2\xi \tag{2.33}$$

The Mathieu equation (2.23) then becomes

$$\frac{d^2 u}{d\xi^2} = 2q_u \Lambda \cos 2\xi - q_u^2 \Lambda \cos^2 2\xi \tag{2.34}$$

Now, since the micromotion oscillation follows the RF frequency, averaging $d^2\delta/d\xi^2$ over one period of RF equals zero. Consequently, the macromotion oscillation averaged over the same period of RF is then given by

$$\left\langle \frac{d^2 \Lambda}{d\xi^2} \right\rangle_{average} = \frac{1}{\pi} \int_0^{\pi} \frac{d^2 u}{d\xi^2} d\xi \tag{2.35}$$

Evaluating the integral using (2.34), the equation of motion for Λ over one RF period becomes

$$\frac{d^2 \Lambda}{d\xi^2} = \frac{-q_u^2}{2} \Lambda \tag{2.36}$$

Rewriting (2.36) in terms of time then yields

$$\frac{d^2 \Lambda}{dt^2} = \frac{-q_u^2 \omega^2}{4} \Lambda \tag{2.37}$$

As can now be seen, (2.37) represents merely simple harmonic motion in Λ with an oscillation frequency of ω_o

$$\frac{d^2 \Lambda}{dt^2} = -\omega_o^2 \Lambda \tag{2.38}$$

Substituting q_u with its definition (2.21), so that Λ is expressed in terms of the physical trap parameters, (2.38) becomes

$$\frac{d^2\Lambda}{dt^2} = -\left(\frac{e^2V^2}{2m^2\omega^2 r_o^4}\right)\Lambda \tag{2.39}$$

which resembles the equation of motion of an ion of charge e in a potential well of depth $\overline{D_u}$, where

$$\overline{D_u} = \frac{eV^2}{4m\omega^2 r_o^2} = \frac{qV}{8} \tag{2.40}$$

This is in fact the pseudopotential well, where the depth referred to is relative to the "surface" at distance r_o from the well center.

It has therefore been shown that the motion of an ion in an RF quadrupole beam guide behaves as if it were in a parabolic potential well of depth $\overline{D_u}$. It also has an added micromotion that oscillates at the RF frequency (as pointed out above at 180° phase relative to the electric field) and has an amplitude which, for small values of q, is equal to the macromotion displacement multiplied by $q/2$ (Fig. 2.5) [Deh67].

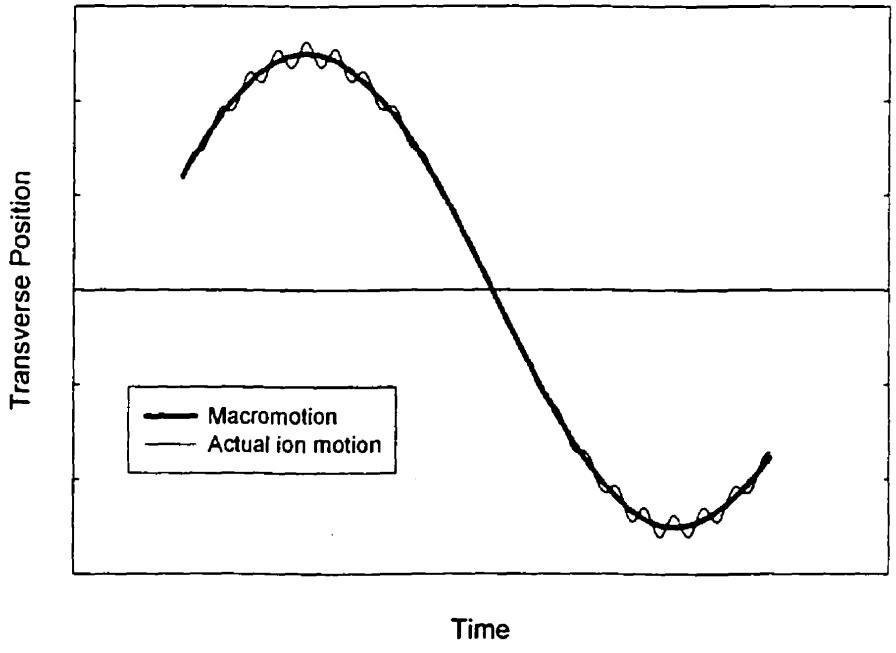

Fig. 2.5 Plot of transverse ion motion vs. time for a q value = 0.1. The micromotion is seen to be an RF oscillation on top of the simple harmonic macromotion oscillation.

2.3 Ion Beam Cooling and Trapping

Having established the equation of motion for a single ion in a typical RF quadrupole ion beam guide, it is now possible to discuss the behavior of collections of ions in such a system. The goal of this section is to introduce the theoretical tools necessary to study the processes involved with such a collection of confined ions, establishing definitions for characteristics such as temperature, beam emittance and acceptance and an assortment of other parameters. With these quantities, it will then be possible to discuss the performance of an ion beam guide, and ultimately, a hybrid trap-TOF spectrometer.

2.3.1 Introduction to Phase Space Dynamics

Phase space dynamics is a powerful tool in the study of ion beam guides and ion traps. It allows one to easily visualize the time evolution of a collection of particles in which each particle has a different trajectory. Specifically, it is a description of the individual trajectories in terms of the position (x, y, z) and momentum (p_x, p_y, p_z) coordinates at any point in time. Collectively, these six coordinates (x, y, z, p_x, p_y, p_z) are known as the coordinates of the particles in six-dimensional phase space.

The Central Potential – Phase Space Ellipses

Beginning with the Hamiltonian formalism for a central force field, which is appropriate for a confining potential such as an RF quadrupole field,

$$\begin{aligned} H &= T(p_1, p_2, \ldots p_n) + V(q_1, q_2, \ldots q_n) \\ &= \sum_{i=1}^{n} \frac{p_i^2}{2m} + \frac{kq_i^2}{2} \end{aligned} \tag{2.41}$$

where n represents the total number of degrees of freedom in an ensemble of particles and k is the effective spring constant of the central potential.

The associated Hamilton's equations, as expressed in canonical form, are

$$\dot{q}_i = \frac{\partial H}{\partial p_i} = \frac{p_i}{m} \tag{2.42}$$

$$\dot{p}_i = -\frac{\partial H}{\partial q_i} = -kq_i \tag{2.43}$$

Defining the ratio $k/m = \omega^2$, the solutions to the Hamilton's equations are

$$q_i = A_i \cos(\omega t + \phi) \tag{2.44}$$

$$p_i = -A_i m\omega \sin(\omega t + \phi) \tag{2.45}$$

A_i is the amplitude of oscillation of the i^{th} particle in the ensemble and ϕ is the phase angle that is determined by the initial conditions of the i^{th} particle. These are the familiar equations of the simple harmonic oscillator and are represented in phase space by a family of ellipses. (Fig. 2.6)

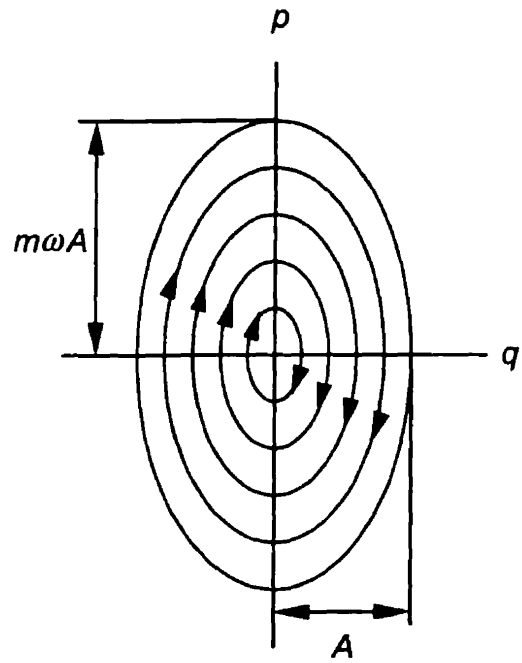

Fig. 2.6 Phase space ellipses representing the paths of particles that are confined by a parabolic potential minimum. The maximum amplitude of oscillation is A and maximum momentum is $m\omega A$.

Liouville's Theorem

As already pointed out in the previous chapter, it is usually not possible to uniquely identify each point in phase space of a collection of a large number of particles. Also, it is impossible to determine the exact initial condition of this ensemble. Statistical mechanics therefore approaches the problem by dealing with average quantities of such a collection of particles, such as pressure or temperature.

Having established that a single particle is represented as a point in phase space, an ensemble of particles must therefore correspond to a cloud of points in phase space. In addition to this, each point has its own unique time evolution, which can be determined from the Hamiltonian for the force field, if the initial condition for that point were known.

Now, consider the infinitesimal volume immediately surrounding a point in phase space. It is defined by a boundary surface consisting of phase space points neighboring the point in question. As time progresses, the boundary points move about and the volume it defines changes shape in phase space. It is clear that the number of points within the volume must remain constant, all points within the boundary can never get out. If a point were to cross the boundary, then at some instant in time, that point would have occupied the exact same phase space position as one of the boundary points. Since the phase space path that a point takes is uniquely determined by its location in phase space at a particular point in time, the subsequent path of that particle must necessarily be the same as that of the boundary point. Therefore, a particle can never escape the boundary of a volume in phase space. Conversely, a particle initially outside the boundary can never enter the volume. (Fig. 2.7) [Gol59]

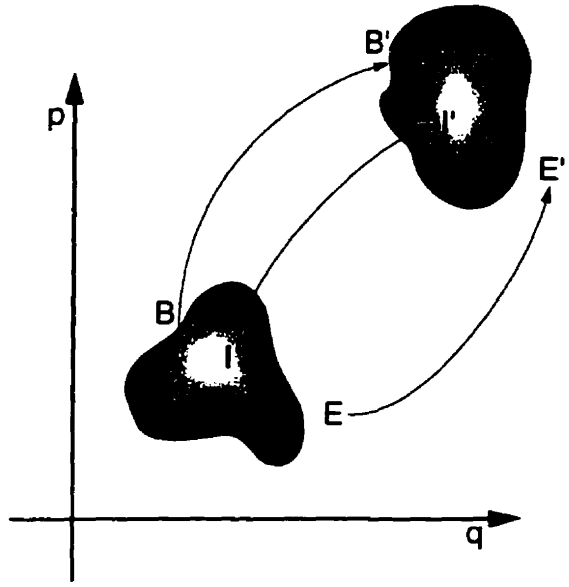

Fig. 2.7 Liouville's theorem: Boundary points (represented by **B**) define a volume in phase space as it evolves in time (**B'**). Interior points (**I**) must always stay within the volume (**I'**), while points exterior to the volume (**E**) remain forever outside (**E'**).

Thus, both the number of points in an infinitesimal region dN and the volume dV are constants, and therefore the density $D = dN/dV$ must also be constant. This leads to Liouville's theorem, which can be expressed in the following way [Law83]:

> *"The particles in phase space form an incompressible gas. The shape of the surface surrounding a group of particles may change, but the density of particles remains constant. This property is the origin of the term 'water bag' ... the analogy is made with incompressible water contained in a hypothetical elastic bag which has zero elasticity so that it exerts no force on the fluid."*

When the three canonical pairs of coordinates in phase space can be uncoupled, as in the case of a central potential, then Liouville's theorem applies to each of the associated *action areas* (momentum × displacement) separately.

$$\iint_{V_1} dx\,dp_x = C_x$$
$$\iint_{V_2} dy\,dp_y = C_y \qquad (2.46)$$
$$\iint_{V_3} dz\,dp_z = C_z$$

where V_1, V_2 and V_3 are the regions containing the ensemble of particles in the $x-p_x$, $y-p_y$ and $z-p_z$ spaces respectively. The natural units to use for ions in accelerator physics are mm for position and $\text{eV}-\mu\text{s/mm}$ for momentum. Therefore, the areas in the action diagrams have units of $\text{eV}-\mu\text{s}$. (In accelerator physics the unit commonly used is $\text{MeV}-\mu\text{s}$, but that is, of course, because of the much higher energies involved).

Action Diagrams, Emittance and Acceptance

From the considerations of the previous section it can be seen that the phase space volume in six-dimensional space associated with particles in a potential well can be decoupled into three elliptical paths in the action diagrams. In the case of an ensemble of confined particles, the entire system is represented by a boundary ellipse whose area contains all the paths of the individual particles. In (q, p) coordinates, a boundary ellipse (Fig. 2.8) can be written as

$$\gamma q^2 + 2\alpha qp + \beta p^2 = \varepsilon \qquad (2.47)$$

where ε is given by

$$\varepsilon = \frac{\text{area of the ellipse}}{\pi}$$
$$= q_{\max} \times p_{\text{int}} \qquad (2.48)$$
$$= q_{\text{int}} \times p_{\max}$$

The angle θ that the major axis of the ellipse forms with the q axis is give by

$$\tan 2\theta = \frac{-2\alpha}{\beta - \gamma} \qquad (2.49)$$

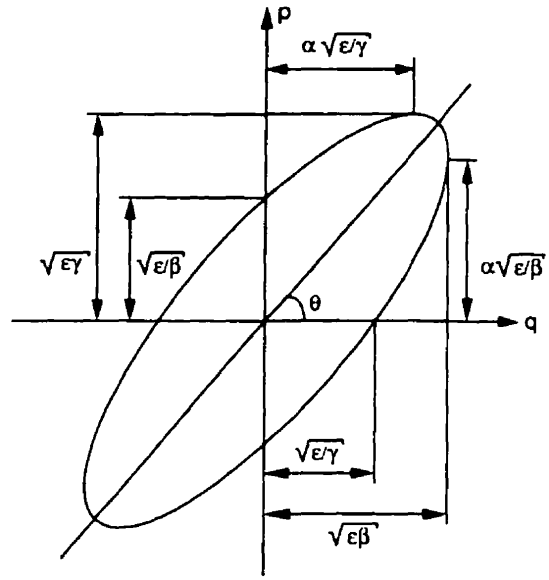

Fig. 2.8 General action diagram ellipse showing critical values

The area of the boundary ellipse can be viewed in two ways. In a beam transport system, the set of three orthogonal action diagrams representing the boundaries of the ensemble of particles are called *emittance* ellipses of the system. In this way, the area of the ellipse or ε is used to characterize the emergent beam or pulse from the transport system.

Another way to think of the boundary ellipses is to view them as the limiting values of q and p for which a transport system will transmit incoming particles. Beyond these limiting values, the particles would have either momenta or positions that were too large or too small to have entered the system correctly. These ellipses then define the total phase space volume that the system will accept, and are referred to as *acceptance* ellipses.

Together with the area of the ellipse, the acceptance and emittance ellipses have important applications in determining performances in ion transport systems. Simply by considering the emittance and acceptance between two systems, it is possible to know exactly how many particles are transported undisturbed, and with what positions and momenta. (Fig. 2.9)

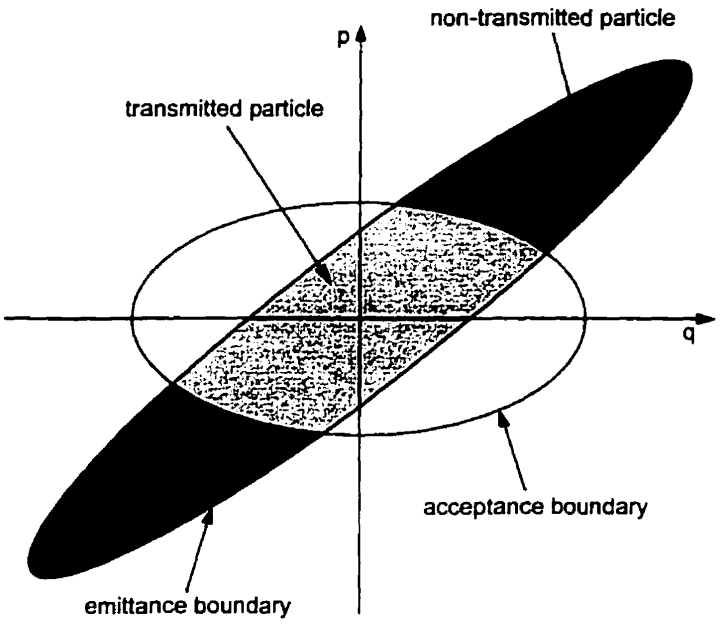

Fig. 2.9 Emittance and acceptance ellipses.

Time Evolution of Action Diagrams

Besides the normal elliptical path of confined particles as discussed previously, there are two more types of time evolution in action diagrams that are important in the discussion of this thesis. One is the propagation of particles in a field free region, which is crucial to the understanding of Time-of-Flight behavior. The other is the extraction of particles in a uniform electric field, which occurs during the pulsing of the ion cloud out of LTRAP.

The field free region is the simpler of the two situations and will be discussed first. Consider an ensemble of identical particles occupying a rectangular region in phase space with a width Δq and a height Δp. Since there are no fields present in this region, the time evolution of each particle is given by

$$q(t) = q_i + \frac{p_i}{m}t \quad \text{and} \quad p(t) = p_i \tag{2.50}$$

where q_i and p_i are the initial position and momentum coordinates at time $t = 0$.

As can be seen in (Fig. 2.10), the original rectangular area is transformed into a parallelogram after time t. The momentum spread Δp remains the same, as it should in the absence of any force, while the spatial spread increases proportionally with Δp.

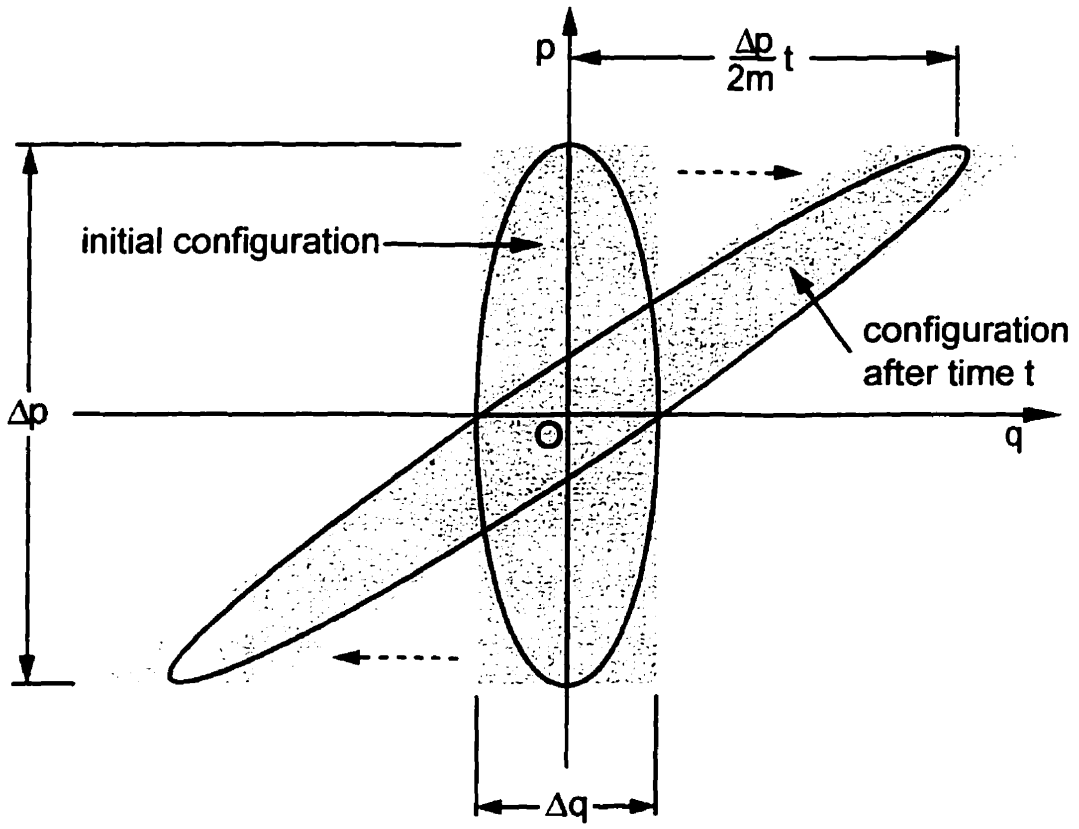

Fig. 2.10 Action diagram of the time evolution of particles travelling in a field free region.

In the second situation, under the influence of a uniform electric field, the ensemble will experience a change in momentum as well as a spatial translation. Consider once again a system of identical particles occupying a rectangular area in phase space with width Δq and a height Δp, experiencing a force $\mathbf{F} = e\mathbf{E}$ in the positive q direction. In this case, the time evolution can be expressed as the following

$$q(t) = q_i + \frac{p_i}{m}t + \frac{e|\mathbf{E}|}{2m}t^2 \tag{2.51}$$

$$p(t) = p_i + e|\mathbf{E}|t \tag{2.52}$$

Again, as seen in Fig. 2.11, the rectangular action area is transformed into a parallelogram. Also, because a force $e\mathbf{E}$ has been introduced, the center of the ensemble has also shifted an amount $dq = e|\mathbf{E}|t^2/2m$ and $dp = e|\mathbf{E}|t$.

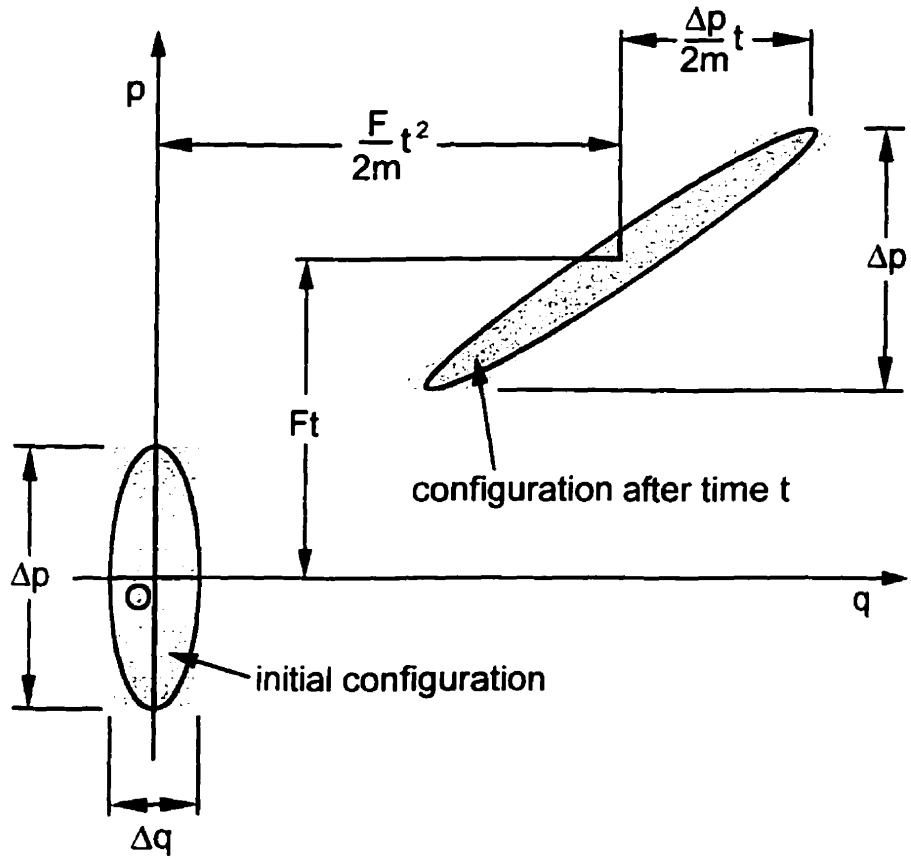

Fig. 2.11 Action diagram of the time evolution of particles travelling in a constant field region.

2.3.2 Ion Temperature and Ion Cooling

In theory it is possible to discuss n particles in phase space and manipulate quantities such as position, momentum and energy. In practice, when dealing with an ensemble of particles, one must inevitably turn to statistical mechanics in order to understand quantities such as spatial and velocity distributions and more importantly, temperature. Note that for the purposes of this experiment, it is sufficient to deal only with the pseudopotential well model of the RF quadrupole ion beam guide as the micromotion of particles plays only a secondary effect to the results.

Beginning with the Gibb's distribution for the definition of temperature of a system of particles, the number of particles N that occupy a volume S in phase space can be written as

$$\frac{d^6N}{dS} = C\, e^{\frac{-E}{k_B T}} \tag{2.53}$$

where T is the temperature of the system and k_B is the Boltzmann constant

$$\begin{aligned} k_B &= 8.617 \times 10^{-5}\ \text{eV/K} \\ (k_B T \text{ at } 300\text{K} &= 0.02582\ \text{eV}) \end{aligned} \tag{2.54}$$

If the system is such that the motion in the three coordinates can be decoupled, then it is possible to deal with each canonical pair of coordinates separately. For a simple harmonic oscillator in one dimension, the total energy E is

$$E = \frac{p^2}{2m} + \frac{1}{2} m\omega^2 q^2 \tag{2.55}$$

Replacing (2.55) into (2.53) and integrating over the two other pairs of canonical coordinates, the number distribution can then be written as

$$\frac{d^2N}{dqdp} = \frac{N_o \omega}{2\pi k_B T} e^{\frac{-m\omega^2}{2k_B T}\left(q^2 + \left(\frac{p}{m\omega}\right)^2\right)} \tag{2.56}$$

where N_o is the total number of particles in the ensemble.

Performing an integration over dq from $-\infty$ to ∞ yields

$$\frac{dN}{dp} = \frac{N_o}{\sqrt{2\pi m k_B T}} e^{\frac{-p^2}{2mk_B T}} \tag{2.57}$$

Performing an integration over dp on (2.56) from $-\infty$ to ∞ yields

$$\frac{dN}{dq} = N_o \sqrt{\frac{m\omega^2}{2\pi k_B T}}\, e^{\frac{-m\omega^2 q^2}{2k_B T}} \tag{2.58}$$

As is expected for a simple harmonic oscillator, the particle distributions in both position and momentum are Gaussian, with standard deviations σ_q and σ_p equal to

$$\sigma_q = \frac{1}{\omega}\sqrt{\frac{k_B T}{m}} \tag{2.59}$$

$$\sigma_p = \sqrt{m k_B T} \tag{2.60}$$

In an action diagram, this would correspond to a two dimensional Gaussian distribution of particles, where an ellipse corresponding to 1σ would contain about 40% of the all the particles, 2σ about 87% and 3σ about 99%. (Fig. 2.12)

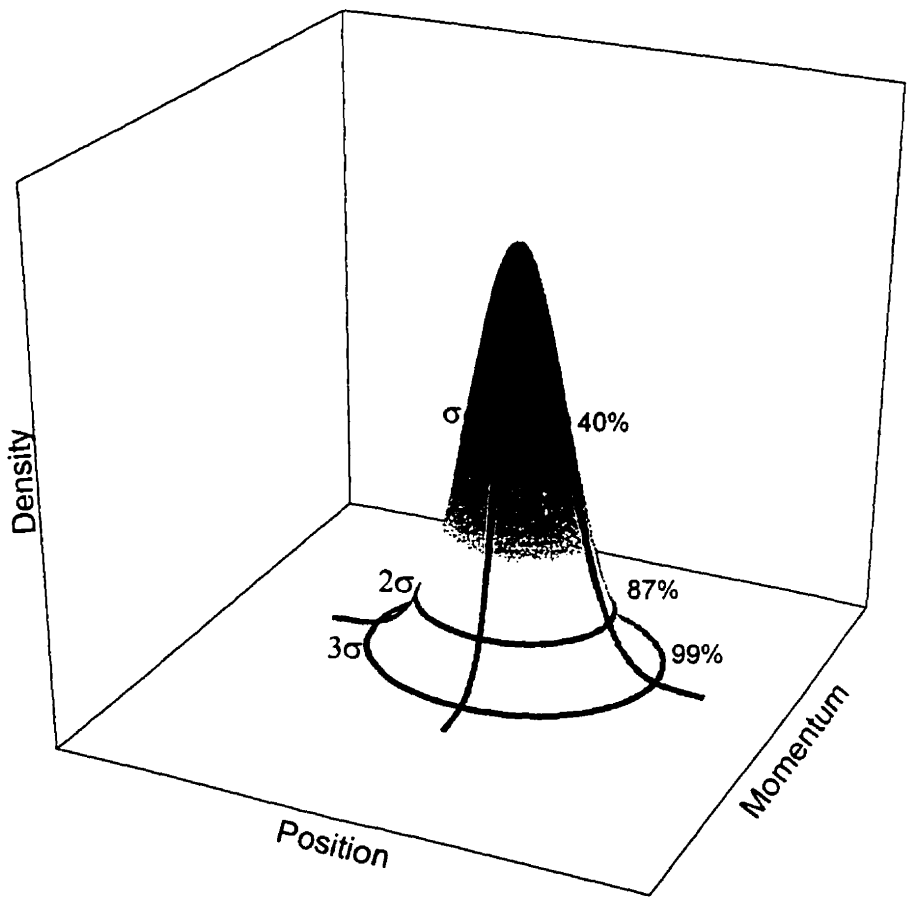

Fig. 2.12 Density distribution as a projection in an action diagram for a particular direction in phase space. The distribution represents particles in a simple harmonic oscillator at thermal equilibrium.

Thus, it has been shown that the spatial and velocity distributions of confined ions are critically dependent on the temperature of the system. By lowering the temperature of the ensemble, it is therefore possible to reduce the spatial and velocity spread of the particles and confine them in a smaller and smaller volume of phase space. Conversely, any system that will heat the ions will result in the ensemble occupying a larger volume in phase space.

2.3.3 Collisional Cooling, Evaporative Cooling and RF Heating

In considering the temperature of the ion ensemble, it is also important to introduce the mechanisms through which the ion temperature can change. In the field of ion trapping and beam confinement, the principle mechanisms involved are cooling due to collisions with the background buffer gas molecules, evaporative cooling due to loss of hot ions from the trap, and RF heating, caused by part of the micromotion kinetic energy being added statistically to the random energy of the particles by collisions of the ions with the gas. Only a brief overview of each will be presented here.

Collisional Cooling

Major and Dehmelt [Maj68] identified three distinct cases of ion-neutral collisions. They began by considering all ion collisions as being perfectly elastic with neutral gas particles that are at rest. In the first case, the ion mass (m_i) is smaller than the neutral mass (m_n). For this case, they showed that the elastic scattering of the ions due to the RF micromotion of the ions resulted in an overall increase in kinetic energy of the ion ensemble. Thus, there was evidence of collisional heating when $m_i << m_n$. In the second case, $m_i = m_n$, and the net effect of the elastic collisions was to leave the average ionic kinetic energy unchanged. The third case was for $m_i >> m_n$, and in this case, they showed that the neutral particles created a viscous drag effect, which reduced the kinetic energy of the ions. This viscous drag was in fact the result of many soft collisions of the light neutral gas particles with the larger ion. This effect was termed collisional cooling.

Evaporative Cooling

Evaporative cooling is another process that happens to ion ensembles within a trapping system or a beam focusing system. In thermal equilibrium, the ions will reach a certain spatial extent determined by the ensemble's temperature. This maximum extent can at times reach beyond the physical size of the trap or focusing system and thus the outermost ions will collide with the electrodes and be removed from the ensemble. Of course, the ions that are energetic enough to reach the outer limits of the ensemble's spatial extent are the ions that carry the most energy, and with their removal from the system, the temperature of the ensemble decreases. This temperature decrease will continue until the entire spatial extent of the ensemble becomes less than the physical restrictions of the system. In essence, the process is similar to evaporation, since the "hot" ions leave the ensemble and leave only the "cold" ions behind, and the process is therefore termed evaporative cooling.

RF Heating

If the neutral gas particles were indeed static, as in the model by Major and Dehmelt, then the ion ensemble would continue to cool asymptotically to zero temperature. However, in a real system, the buffer gas particles themselves have a kinetic energy distribution, determined by the temperature of the gas, notably room temperature. Therefore, the ion ensemble must have a temperature at least the same as this room temperature. From other observations, it has been shown that the ion temperature was in fact greater than the buffer gas temperature, and the mechanism identified for this heating was the RF motion of the ions. Beyond the pseudopotential well model, which established the ions' phase space distributions and related it to its temperature, the RF motion of the ions has to be taken into consideration. This RF motion increases the mean kinetic energy of the ions However, this motion is coherent to the RF field and so itself is not a part of the statistical distribution associated with temperature. Yet collisions with the gas can transfer part of the coherent RF motion energy into incoherent motion, which does then later add to the incoherent thermal motion. This exchange of energy increases the overall temperature of the ions to above that of the background gas and is called RF heating.

In the case of a large ensemble of particles, the situation is even more complicated because of the space charge repulsion present in the system. The spatial extent of the ion ensemble is enlarged due to the internal space charge forces and the ions reach further out in the pseudopotential well, where the RF motion is greater and the RF heating more severe. As a result, by many ion-neutral collisions, this increase in energy gets transferred back into the center of the ensemble and the temperature of the system increases [Lun92][Kim97].

2.4 Time-of-Flight Spectrometry

In this section, the theory governing the operation of Time-of-Flight (TOF) mass spectrometry will be covered, outlining the basic principles and concepts that control a TOF instrument's capabilities, performance and resolution.

2.4.1 Basic Principles of Time-of-Flight

Mass measurements based on Time-of-Flight show a simplicity and an elegance of design that makes TOF an attractive technique. Ions of differing masses start their flight all roughly at the same point in space (called the *extraction region*) (Fig. 2.13). At the starting time t_o, they experience an electric field E that accelerates them all to the same kinetic energy

$$\frac{mv^2}{2} = zeEs \tag{2.61}$$

where m is the mass of the ion, v its velocity, z is the number of charges on the ion, e is the electron charge and s is the spatial extent of the extraction region.

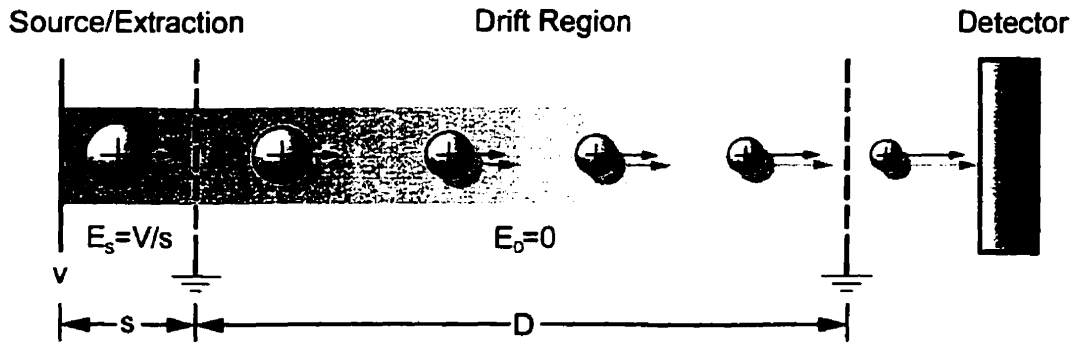

Fig. 2.13 Schematic diagram of a Time-of-Flight system, detailing the Extraction Region, Drift Region and Detector. TOF spectrometry works on the principle that lighter masses arrive at the detector earlier than heavy masses.

As the ions pass through the extraction region, typically defined by an exit grid or mesh, the ions attain a velocity that is inversely proportional to the square root of its mass

$$v = \left[\frac{2zeEs}{m}\right]^{1/2} \tag{2.62}$$

After leaving the extraction region, these ions then pass into a much longer *drift region* whose length is D. Since this drift region is much larger than the extraction region, the time it takes for the ions to reach the detector at the end of the drift region is approximately

$$t = \left[\frac{m}{2zeEs}\right]^{1/2} D \tag{2.63}$$

Thus, the time of flight of the ions becomes an effective method of measuring the different masses of the ions (Fig. 2.14). In fact, the mass distribution can be directly related to the time-of-flight spectrum of the ions as they arrive at the detector

$$\frac{m}{z} = 2eEs\left(\frac{t}{D}\right)^2 \tag{2.64}$$

In practice however, the time spectrum is calibrated using at least two known masses that can then determine the following empirical relationship

$$\frac{m}{z} = at^2 + b \tag{2.65}$$

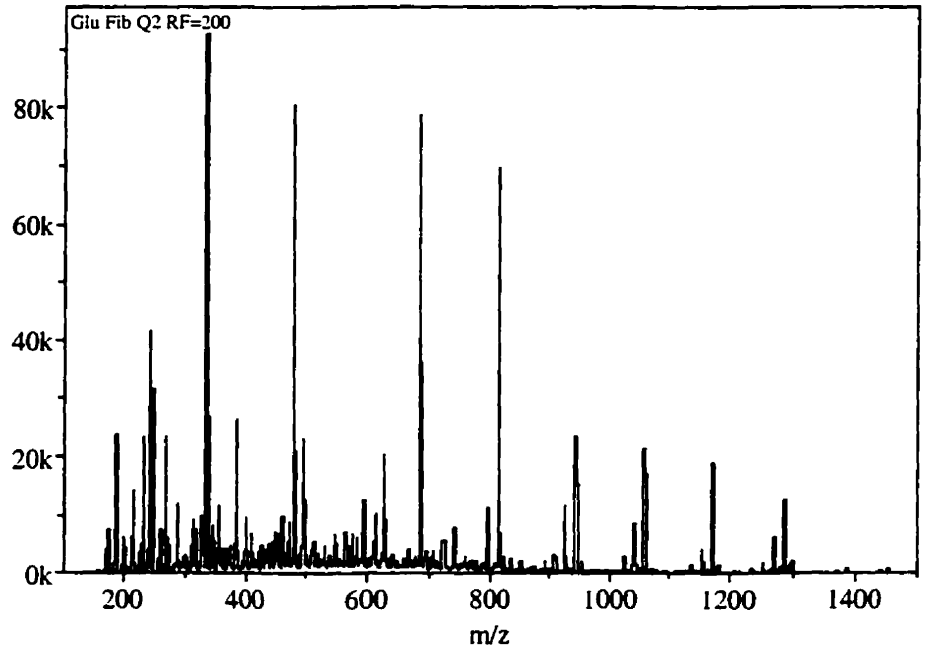

Fig. 2.14 Example of a TOF spectrum. MS/MS of 2+ ion of Glu-fibrinopeptide B (m/z=785.8).

2.4.2 A Phase Space Approach to Time-of-Flight Spectrometry

In considering the dynamics of an effective time-of-flight system, it is helpful to take a phase space approach to understanding the mechanics of the spectrometer. Since the TOF system works in only one dimension, only the axial action diagram will be considered.

First, consider a gaussian distribution of ions at the source/extraction region of the time-of-flight spectrometer. This ensemble of ions can be represented by an action ellipse in the z-p_z plane, as in Fig. 2.10 and Fig. 2.11, in contrast to the parallelogram distribution assumed in Chapter 1.

At the start of the time-of-flight, the ions are extracted by a uniform electric field in the positive z direction, causing the entire ensemble to progress forward. Upon reaching the mesh that defines the end of the extraction region, the ions at the front of the ensemble no longer experience any accelerating force and continue their time evolution according to field-free motion. However, the ions at the tail end of the distribution continue being accelerated until they too cross the mesh and start their field-free motion in the drift region. The net effect of this is to cause the ellipse to rotate over itself by nearly 90°, depending on the strength of the extraction field. After the entire ion cloud has passed through the extraction mesh, the ensemble then progresses along the drift region in field-free motion until it reaches the detector. This time evolution of the ion ensemble can be summarized by Fig. 2.15.

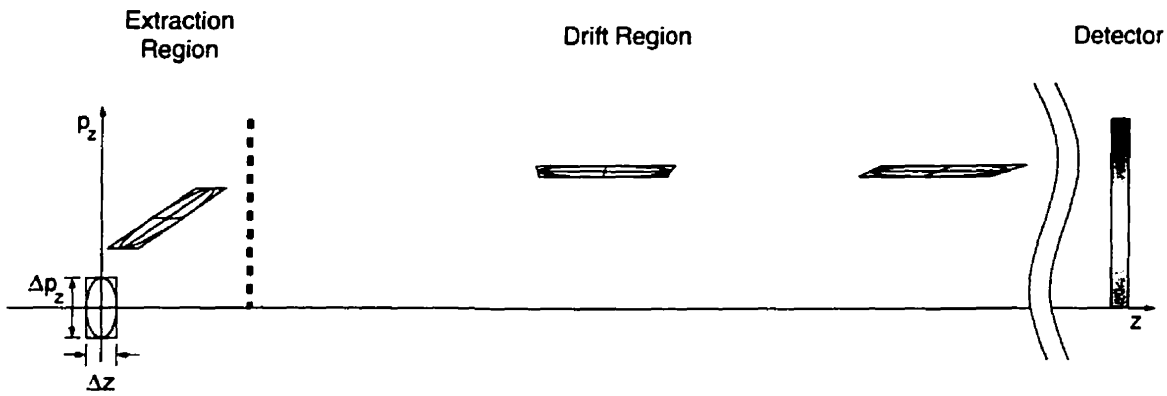

Fig. 2.15 Phase space evolution of ion ensemble in TOF system.

It can be seen that the evolution of the elliptical action diagram is as if it were contained within the parallelogram that evolved from the rectangle surrounding the initial ellipse.

As in the simple parallelogram, characteristic of all time-of-flight spectrometers, what determines the time width of the detected pulse at the end of the spectrometer is the spatial width of the ion ensemble and the velocity spread among them as they pass the plane of the detector. It is, of course, this time spread that ultimately determines the mass resolution of the spectrometer once the conversion is done between a time spectrum of the detected ions to a mass spectrum. It must be noted that as a result of Liouville's theorem, the spatial and momentum spreads of the action diagrams (and thus the velocity spread) are strongly related to each other. This can easily be seen by considering the action parallelograms of Fig. 2.15, which must always have a constant area of $\Delta z \cdot \Delta p_z$, as required by Liouville's theorem.

In order to achieve the smallest Δz at the detector, it is desirable to force the Δp_z to be as large as possible, thus stretching the action diagram in the momentum direction and at the same time, forcing the spatial spread to a minimum. This, of course is the $z - p_z$ equivalent of increasing the energy spread to improve time-of-flight resolution, as discussed in Chapter 1.

Momentum-displacement action diagrams present a very clear picture of how the signal arises in a TOF spectrometer. At any instant the signal level is simply proportional to the number of ions in a vertical (momentum) slice of the action diagram at the value of z corresponding to the position of the detector. The evolution of this signal is determined by the number of ions in each such slice as the action diagram moves onto the detector. The detector signal is therefore a profile of the density distribution of the action diagram viewed in the direction of the momentum coordinate.

Any model of the ion collection in the trap will also result in a specific density distribution in the action diagram at the detector. If this density distribution results in the same signal as that observed in the experiment then one has some basis for believing that the model does represent the actual ion distribution in the trap, particularly if, as in the thermodynamic model used in this thesis, there is only one adjustable parameter in the model, i.e. the temperature.

However, the detector is insensitive to the particle momenta and so does not probe the density distribution in the momentum direction of the action diagram. Hence the model could have an erroneous momentum distribution and still duplicate the detected signal. To check on this possibility, different extraction potentials can be used, resulting in different action diagrams at the detector for the same action diagram for the trap collection. If the model of the trap collection duplicates the observed signals for all of these extraction potentials, then it becomes more certain that it represents the actual collection.

While such a procedure can give very precise results, as the work of this thesis will show, it would be more satisfying to have a model-independent procedure for discerning the actual action diagram of the trap collection. In principle this is possible. The ions in each slice of the action diagram at the detector occupy a slice in the original action diagram for the trap. In general, this slice will not be aligned with either the momentum or the displacement axis of the diagram but will be at an angle determined by the extraction parameters, with smaller angles relative to the displacement axis for higher extraction fields. Thus the detector signal presents the density profile of the action diagram in the trap when viewed from a particular angle in the diagram and this angle can be varied by changing the extraction field. Just as flying around a mountain allows one to discern the shape of the mountain, the different views of the action diagram allows one to discern its density distribution in both momentum and displacement.

The mathematical procedure for extracting a density distribution using data from different views is based on the so-called Fourier slice projection theorem and is most commonly known for its application in Computerized Axial Tomographic (CAT) scanning in medicine. Its application to scanning action diagrams was first suggested by D. Lunney [Lun92] in the context of the action diagrams for a Paul trap but the time resolution of the system for processing the signals from his work was insufficient to actually resolve the views of the action diagrams. However, because LTRAP was designed to be weaker so as to get a larger action diagram and because the TOF detection system was designed to have better resolution, it is of interest to try to confirm the temperature model of the ion collection in LTRAP using this technique. The theory of slice projection is therefore outlined here.

2.5 Tomographic Phase Space Reconstruction

The following sections outline the theory of tomography, which is the technique used to "image" the phase space diagram, and how the time-of-flight spectra obtained in this thesis are in fact projections of the ion density function in phase space.

2.5.1 The Fourier Slice Theorem

The Fourier Slice Theorem was developed in the study of tomography. Tomography is the science of imaging an object from multiple cross-sectional views from different directions. It enables one to mathematically model the original object from the individual projections, combining each projection back into a whole picture. Where this is most used today is in medical imaging, where x-rays, ultrasounds and NMR's provide different views of the interior of the human body, allowing doctors and researchers a better understanding of it. It is almost coincidental that the technique of tomography would be able to be applied in the area of this thesis, for the 'imaging' of a phase space cloud.

Parallel Projections

Regardless of the method in which a projection is obtained, a projection of an object can be thought of as simply a collection of line integrals of a two dimensional function. Consider an object defined on the Cartesian plane as $f(x, y)$. The parallel projection of this object would then be given as

$$P_\theta(t) = \int_{(\theta,t)line} f(x, y)ds \tag{2.66}$$

where t is the parameterization of the projection along a line at angle θ to the x-axis (Fig. 2.16 and Fig. 2.17).

Alternatively, t can be expressed as

$$t = x\cos\theta + y\sin\theta \tag{2.67}$$

Using this definition and the delta function, equation (2.66) can then be written as

$$P_\theta(t) = \int_{-\infty}^{\infty}\int_{-\infty}^{\infty} f(x, y)\delta(x\cos\theta + y\sin\theta - t)\,dx\,dy \tag{2.68}$$

which is normally referred to the Radon transform of $f(x, y)$.

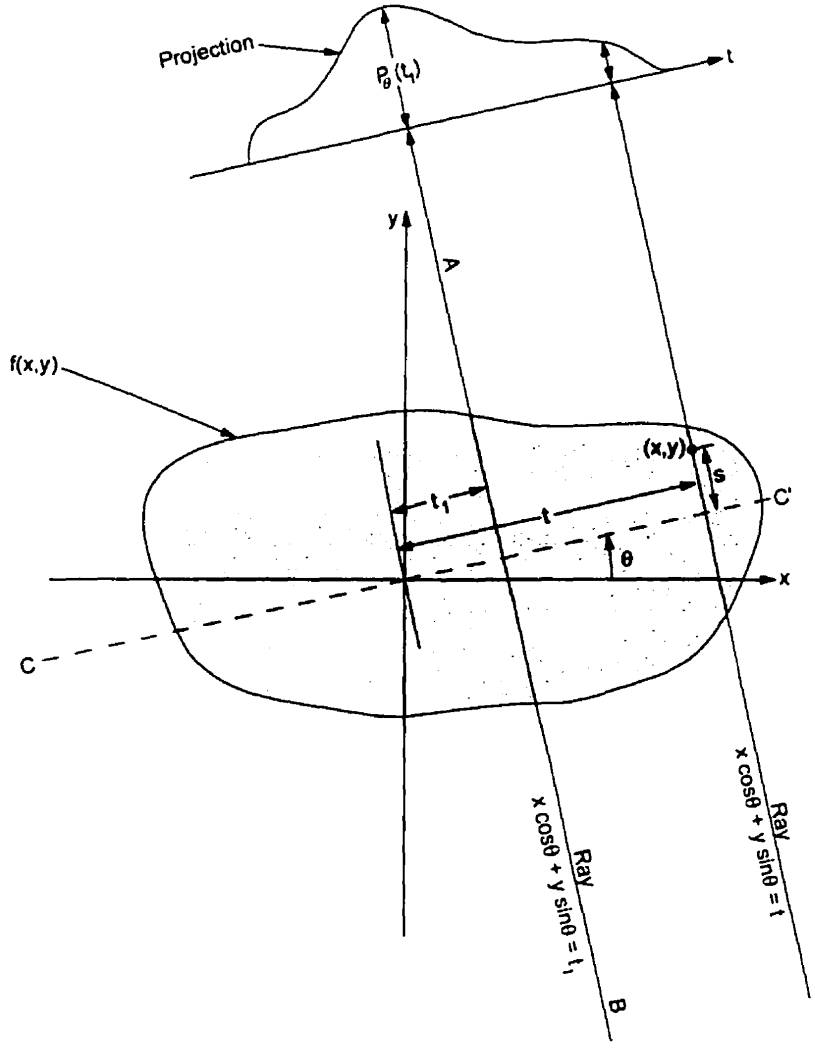

Fig. 2.16 An object $f(x, y)$ and its projection $P_\theta(t_1)$ are shown for an angle of θ.

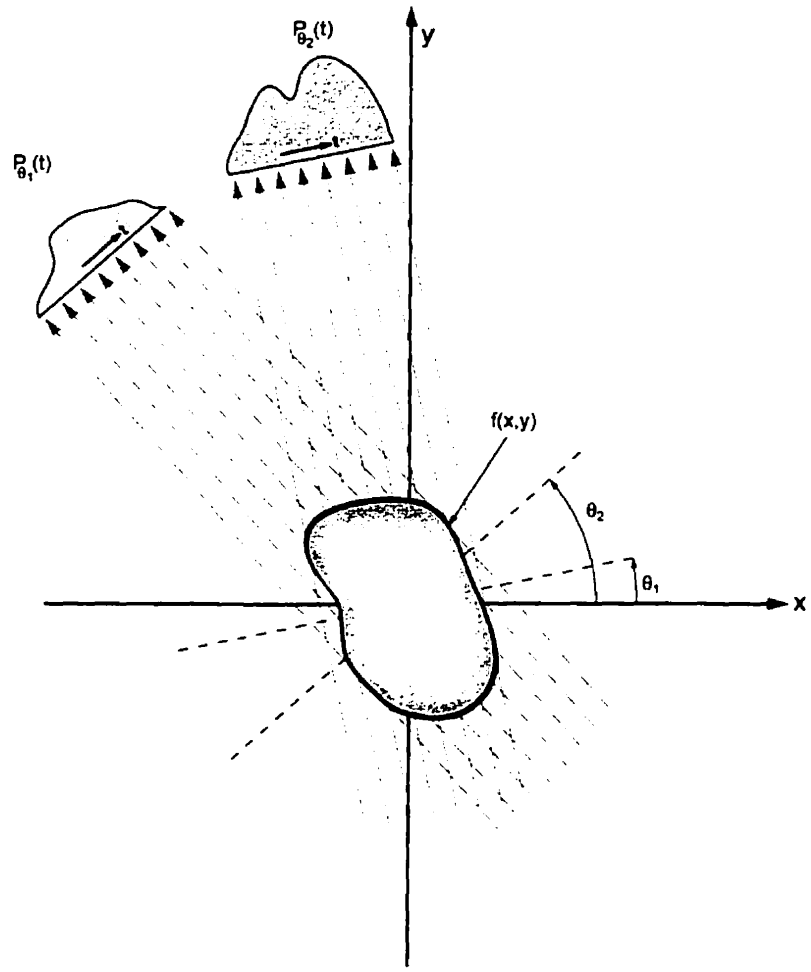

Fig. 2.17 Parallel projections at different viewing angles.

Fourier Slice Theorem

Simply put, if it were possible to take these projections from all angles of θ, it would be possible to completely reconstruct the object function $f(x, y)$. The Fourier Slice Theorem enables one to recombine all the different parallel projections $P_\theta(t)$ by noting that the Fourier transform of the one-dimensional projection is in fact equal to a slice of the two-dimensional Fourier transform of the object function. The technique of reconstruction then lies in simply sampling enough of the two-dimensional Fourier space and then performing an inverse transform to obtain the original function.

Let $F(u, v)$ be the two-dimensional Fourier transform of the object defined by

$$F(u,v) = \int_{-\infty}^{\infty} \int_{-\infty}^{\infty} f(x, y) e^{-2\pi i(ux+vy)} dxdy \tag{2.69}$$

Similarly, the one-dimensional transform of the projection function is

$$S_\theta(\omega) = \int_{-\infty}^{\infty} P_\theta(t) e^{-2\pi i \omega t} dt \tag{2.70}$$

Using equations (2.66), (2.67) and (2.68), $S_\theta(\omega)$ can be rewritten in terms of an integral in (x, y) coordinates

$$S_\theta(\omega) = \int_{-\infty}^{\infty} \int_{-\infty}^{\infty} f(x, y) e^{-2\pi i \omega (x\cos\theta + y\sin\theta)} dx dy \tag{2.71}$$

This double integral can now be seen as the two-dimensional Fourier transform of the object function where the spatial frequencies (u, v) are now $(\omega\cos\theta, \omega\sin\theta)$. Therefore

$$S_\theta(\omega) = \overline{F}(\omega, \theta) = F(\omega\cos\theta, \omega\sin\theta) \tag{2.72}$$

This leads to the Fourier Slice Theorem [Kak88], which states

> *The Fourier transform of a parallel projection of an image $f(x, y)$ taken at angle θ gives a slice of the two-dimensional transform, $F(u, v)$, subtending an angle θ with the u-axis.*

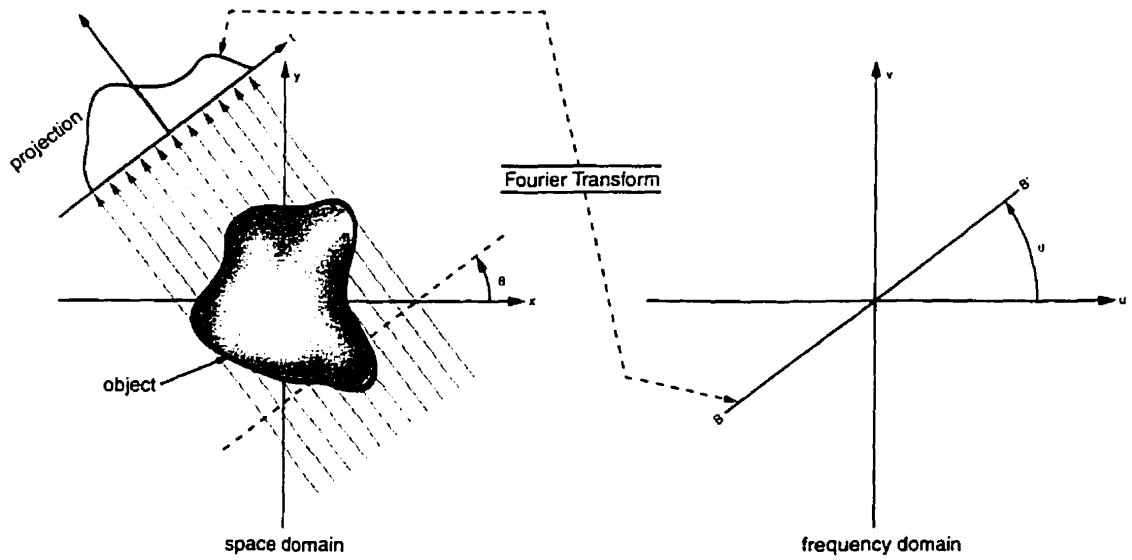

Fig. 2.18 The Fourier Slice Theorem relates the Fourier transform of a projection to the Fourier transform of the object along a radial line (BB')

Backprojection

Backprojection is the technique used to reconstruct the object function from the two-dimensional Fourier transform. Combining projections from different viewing angles becomes the task of filling out the two-dimensional Fourier space along radial lines (Fig. 2.19). The more projections that can be taken, the more the Fourier space is defined. Then by taking a two-dimensional inverse Fourier transform of this space, the reconstructed object function can be determined.

$$f(x,y)=\int_0^{2\pi}\int_{-\infty}^{\infty}\overline{F}(\omega,\theta)e^{2\pi i\omega(x\cos\theta+y\sin\theta)}\,\omega\,d\omega\,d\theta \tag{2.73}$$

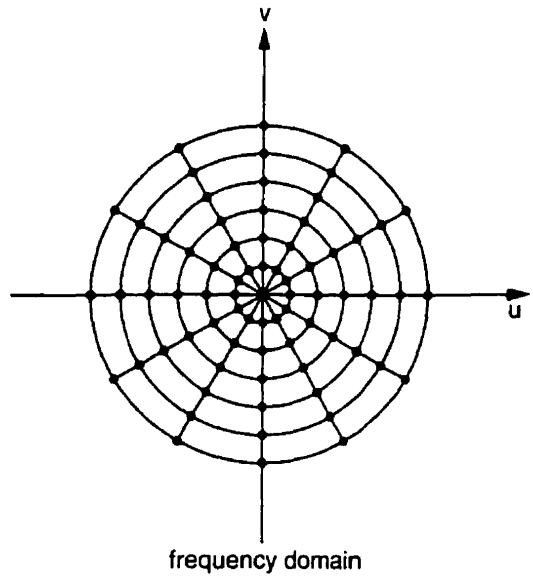

Fig. 2.19 Collecting projections of the object at a number of angles gives estimates of the Fourier transform of the object along radial lines. In practice, since an FFT algorithm is used to transform the data, the dots represent the actual location of estimates of the object's Fourier transform.

Again using the definition (2.67), and the Fourier Slice Theorem

$$\begin{aligned} f(x,y)&=\int_0^{2\pi}\left[\int_{-\infty}^{\infty}\overline{F}(\omega,\theta)\omega e^{2\pi i\omega x}\,d\omega\right]d\theta \\ &=\int_0^{2\pi}\left[\int_{-\infty}^{\infty}S_\theta(\omega)\omega e^{2\pi i\omega x}\,d\omega\right]d\theta \end{aligned} \tag{2.74}$$

which demonstrates how to recover the object function from the one-dimensional Fourier transforms of the parallel projections $P_\theta(t)$ (Fig. 2.20).

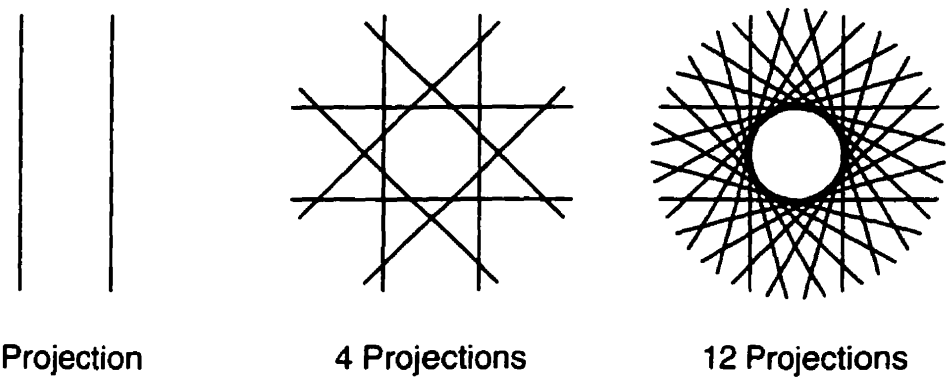

Fig. 2.20 A conceptual diagram showing how to use the backprojection technique to reconstruct the image of a circle.

2.5.2 Parallel Projections in Phase Space

It may not be immediately obvious how the science of tomography can be related to this study in phase space dynamics, but it can be shown that the data collected from the time-of-flight analysis can indeed be thought of as a parallel projection of the initial phase space configuration.

Every point in phase space evolves in time according to the theory outlined in section 2.3.1. The detector in the time-of-flight system is essentially a fixed plane in space that this phase space cloud is evolving towards. As the phase space cloud passes the plane, the density of particles is recorded by the detector, effectively performing a line integration of the density function along the line $z = z_{detector}$. These successive line integrals create the density plot that is the detected signal and represents the parallel projection of the evolved phase space distribution. In order to relate this projection to a slice projection of the initial phase space cloud, all that is required is to map each phase space point at the detector to a phase space point in the initial trap. Thus a viewing angle can then be associated with the detector signal, which can be considered as a parallel projection of the initial phase space distribution (Fig. 2.21).

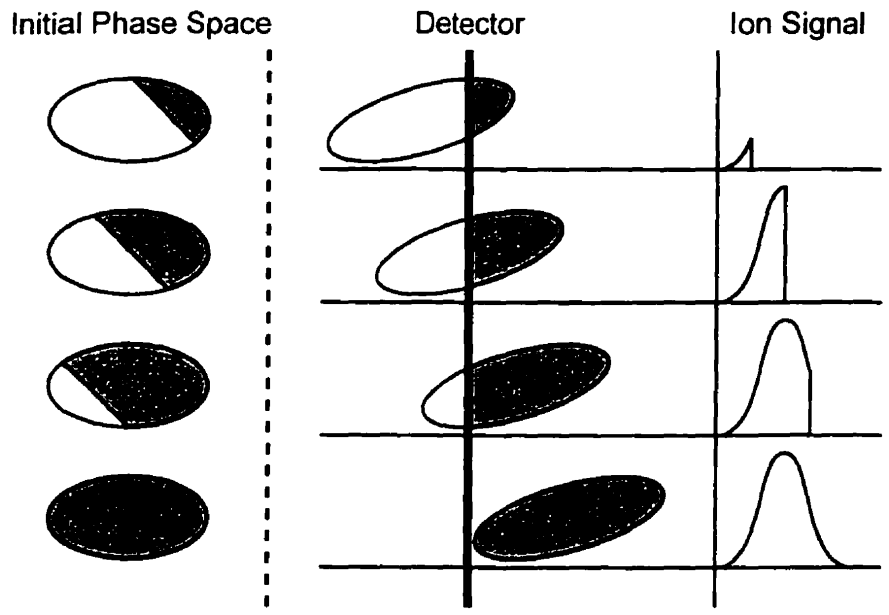

Fig. 2.21 Detected ion signal as a phase space projection. The ion signal (*at right*) corresponds to the integration of the phase space density function at the detector (*center*, shaded area) which can be related to a volume in phase space at the trap (*at left*, shaded area).

To vary viewing angles, one needs to adjust the way in which the phase space points evolve in time. By changing extraction potential in the trap, the particles are basically accelerated to different velocities and therefore arrive at the detector at a different state in its time evolution. This then corresponds to a change in the viewing angle and thus a different projection is obtained at the detector (Fig. 2.22).

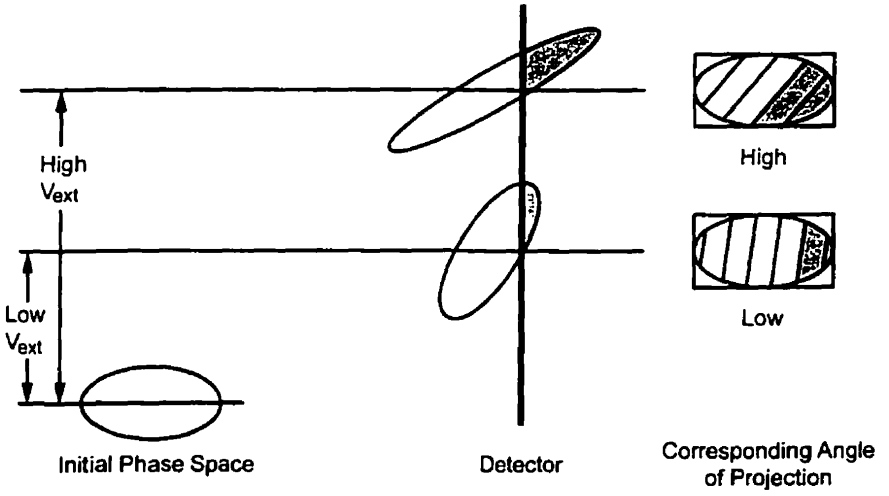

Fig. 2.22 Adjusting angle of projection by varying extraction voltage.

2.6 Time-of-Flight Spectrometry and Liouville's Theorem – A Summary

From the perspective of general phase space considerations, it can be seen that the preservation of the areas of the parallelograms in the action diagrams associated with Time-of-Flight mass spectrometry is simply a consequence of Liouville's theorem. Thus it is not only parallelogram distributions that remain parallelograms with the area preserved; the elliptical distribution in the linear RFQ trap also remain elliptical with the area preserved and the properties of this ellipse when the ions arrive at the detector determines the spectrometer performance.

However, there is a caveat. While the density of the ions and hence the phase space volume they occupy remain constant as the collection proceeds through the spectrometer, the preservation of the elliptical shape and the ion density in the individual action diagrams depends on the spatial and momentum components in a particular direction being independent of the spatial and momentum components in the orthogonal directions. In other words, the manipulating forces must be "linear", meaning that the electric field doing the manipulation must be expressible in first order terms of each spatial coordinate. The presence of higher order terms, which are always present to some degree in real systems, distort the action diagram distributions so that they are no longer exactly elliptical (or as parallelogram with straight sides). The degree to which these distortions, or "aberrations", are avoided is a measure of the quality of the mass spectrometer and sets limits on what is feasible. In practice, the optimum design for a spectrometer can only be established by extensive computer simulations of the evolution of the action diagrams as a given ion collection passes through it.

Chapter 3 Experimental System

As pointed out in the introduction, the purpose of this thesis was to study the dynamics of a collection of ions in a linear RFQ trap for the purpose of using such a device as a source for TOF mass spectrometry. The experimental setup for this study can be thought of as three distinct stages: an ion source and beam cooling system for delivering the ions for collection in the trap, the trap itself (referred to here as LTRAP) and the TOF system used for analysis of the ion dynamics. This chapter will describe these three stages in more detail.

3.1 Ion Source and Beam Cooling System: AXF_RFQ

The ion source and beam cooling system was in fact the one used in the Ph.D. work of Taeman Kim [Kim97] at McGill University, in his study of the effect of buffer gas cooling of ions in a beam guide. The source was a surface ionization type with cesium zeolite as the source of cesium ions (Cs^+; $m/z = 133$). The beam cooling system consisted of a segmented quadrupole rod structure that was contained in a low pressure environment of N_2 buffer gas. Only a brief introduction to each component will be presented here to give an adequate understanding of their functions. For further details the reader is referred to prior works. [Gha96][Kim97]

3.1.1 Ion Gun Assembly

The ion gun is a surface ionization source. The basic mechanism of surface ionization involves bringing the target atoms into contact with a surface characterized by a high work function. In this case, the Cs atoms are evaporated from a Cesium Zeolite sample and the ionizing surface is platinum, chosen for its high work function $(\phi = 5.32\,\mathrm{eV})$.

Atoms incident on a heated metallic surface will leave the surface either as an atom or as an ion. The degree of ionization is often quantified as α:

$$\alpha = \frac{n_i}{n_a} \tag{3.1}$$

where n_i and n_a are the number of ions and atoms leaving the surface respectively.

Generally, α varies with several factors; the surface temperature T, the ionization potential of the incident atom E^i and the work function ϕ of the metallic surface. This relationship can be expressed as follows:

$$\alpha = Ae^{\left[\frac{z_i(\phi - E^i)}{k_B T}\right]} \tag{3.2}$$

where $A = g_i/g_a$ is the statistical weight ratio of the ionic to the atomic state of the species leaving the surface ($g_i = 1$ and $g_a = 2$ for alkali metals) and z_i is the charge state of the ion. [Kin24] It is obvious then, from (3.2) that the optimum situation is the combination of a metallic surface with high work function ϕ and a species of atom with low ionization energy E^i. Lower temperatures also increases α, but the rate of release of the ions from the aluminosilicate is also dependent upon the temperature and so if the temperature is too low, the ions will not leave the ionizing surface.

Cesium was chosen as the ion source for several reasons. It has the lowest ionization energy ($E^i = 3.89\,\text{eV}$) as well as being a higher mass alkali metal. Also, it was relatively easy to prepare the Cs-zeolite sample using a standard ion exchange with a commercial molecular sieve (Varian VACSORB). The detailed theory of cation exchange of aluminosilicates can be found in the reference by Breck [Bre74]. A simple mass spectrum taken of the total ion beam (Fig. 3.1) revealed that the beam was almost completely composed of Cs, with only a trace amount of another ion. When the Cs peak was assigned the value $m/z = 133$ and simplifications were made, the other species was found to be Rubidium, also an alkali metal. Rb is very abundant, easily ionized ($E^i = 4.17\text{eV}$) and bonds naturally to cesium [Han72]; thus it is understandable that trace amounts of it showed up in the spectrum.

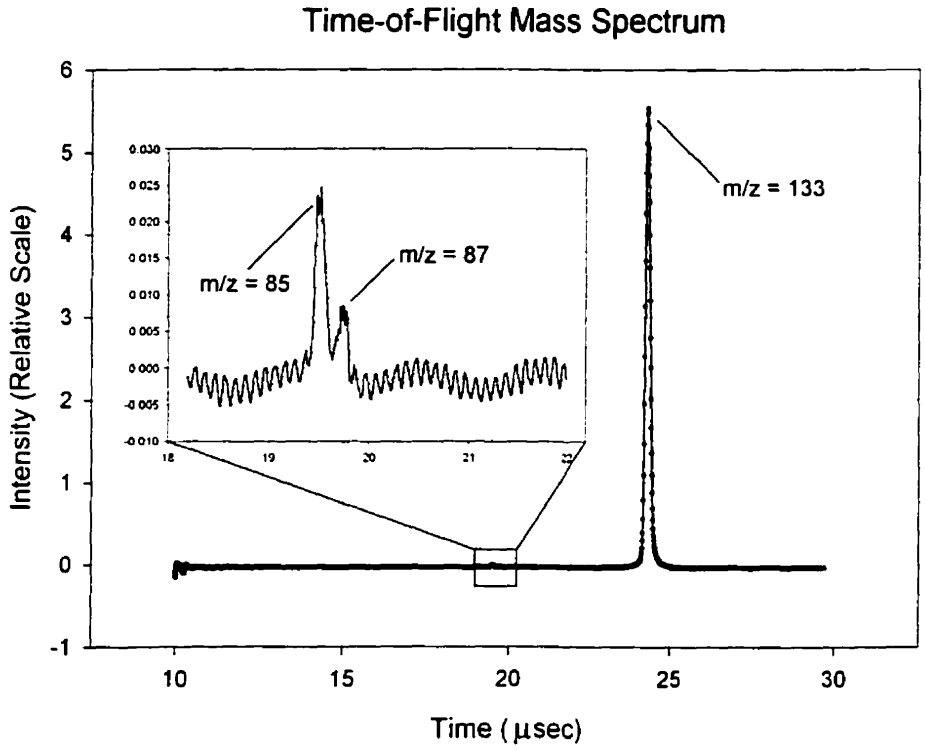

Fig. 3.1 Mass spectrum of ion source taken from TOF data. The mass peaks were calibrated to ${}_{55}Cs^{133}$. The peaks $m/z = 85$ and $m/z = 87$ correspond to ${}_{37}Rb^{85}$ and its isotope ${}_{37}Rb^{87}$, which have relative abundances of 72.15% and 27.85% respectively [Han72].

The final and not insignificant aspect of cesium ions that led to choosing them for this work is that they are very stable in not exchanging their charge state with any impurity molecules in the background gas of the beam cooling and trapping system. This meant that in easily available high-purity nitrogen and with normal vacuum system cleanliness the cesium ions would remain charged for up to seconds, allowing sufficient time to observe even very slow ion cooling.

The Cs-zeolite powder sample was held in a metallic cylinder and fine platinum wires (0.127mm diameter, 99.99% pure) were embedded into the column. The cylinder was made of an alloy, Inconel 601HF, which has a high electrical resistivity and a high melting point. Thus, by passing a DC current (typically 65Amps, approximately 40W of power) through the cylinder, the holder was heated to a high enough temperature where the surface ionization of the Cs on platinum could take place.

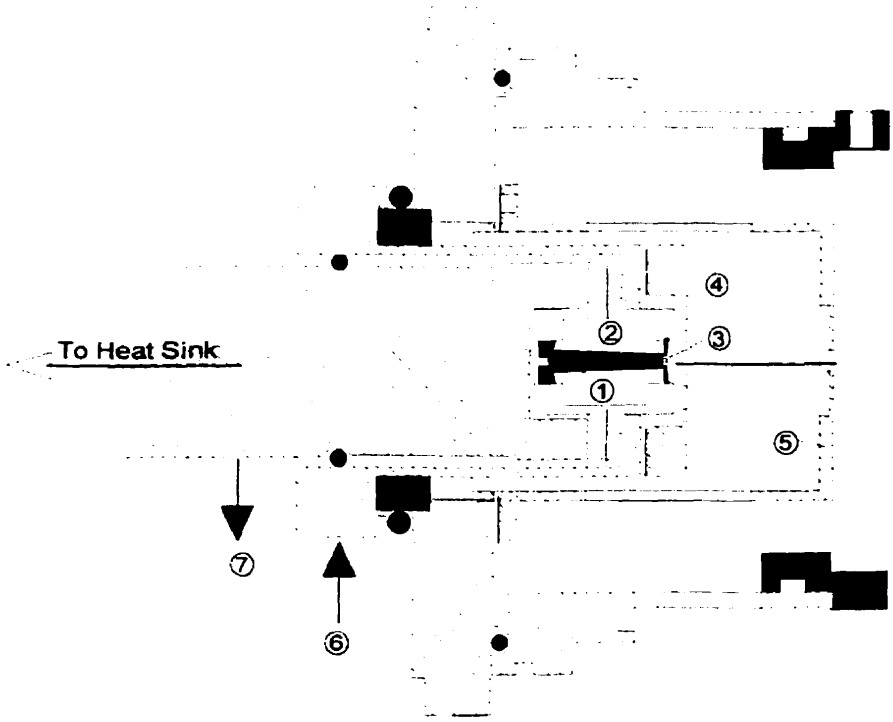

1. Heater
2. Zeolite material
3. Platinum wires
4. Extraction lens (L1)
5. Extraction lens (L2)
6. Heater current in
7. Heater current out

Fig. 3.2 Ion Gun assembly.

After the heater, the ions were accelerated in the beam direction by a series of two lens electrodes, which served to extract the ions from the heater and collimate the beam through a 3mm aperture in the second lens. Emerging from the second electrode, the ion beam had a typical kinetic energy of 25eV. After this lens, the ion beam then entered the high buffer gas region of the first cooling quadrupole system (Fig. 3.2). Rudimentary current measurements were made at this stage by grounding the electrodes of the quadrupole rods and measuring the current through a Keithley 614 Electrometer, showed that the typical incoming current is of the order of 25pA under normal operating conditions.

3.1.2 AXF_RFQ

The cooling quadrupole system was developed by Kim and Moore in 1997. An axial field was introduced into the regular quadrupole beam guide in order to push the ions along the beam axis while in a relatively high buffer gas pressure regime (typically 10^{-2} Torr). The axial field was achieved by taking advantage of the degree of freedom in the z direction of the electric field, which can be seen in Laplace's equation (2.6) when applied to the quadrupole beam guide (eq. (2.11) and (2.12)). Having this freedom, the quadrupole rods were then segmented in order to apply a DC bias voltage on each segment, using a resistive network chain to couple a segment with its neighboring segments (Fig. 3.3). In this way, an axial field was created and dragged the ions along the axis (Fig. 3.4), while the high buffer gas effectively cooled the ions to nearly room temperature, i.e. 0.025 eV.

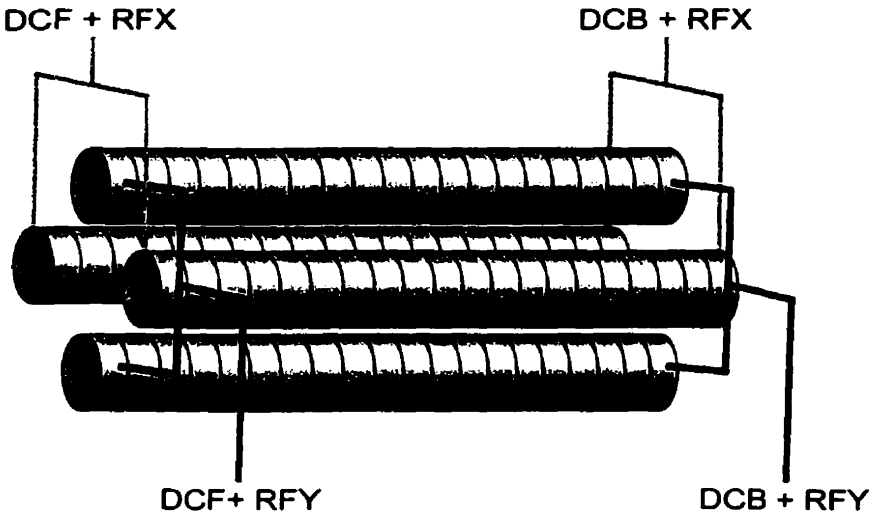

Fig. 3.3 Segmented Quadrupole rods. AC voltages **RFX** and **RFY** are applied to opposing pairs of rods. DC voltages **DCF** and **DCB** are applied to the front and back segments of the rods. Each segment is coupled to its neighbors by a 1kΩ resistor (*not shown*).

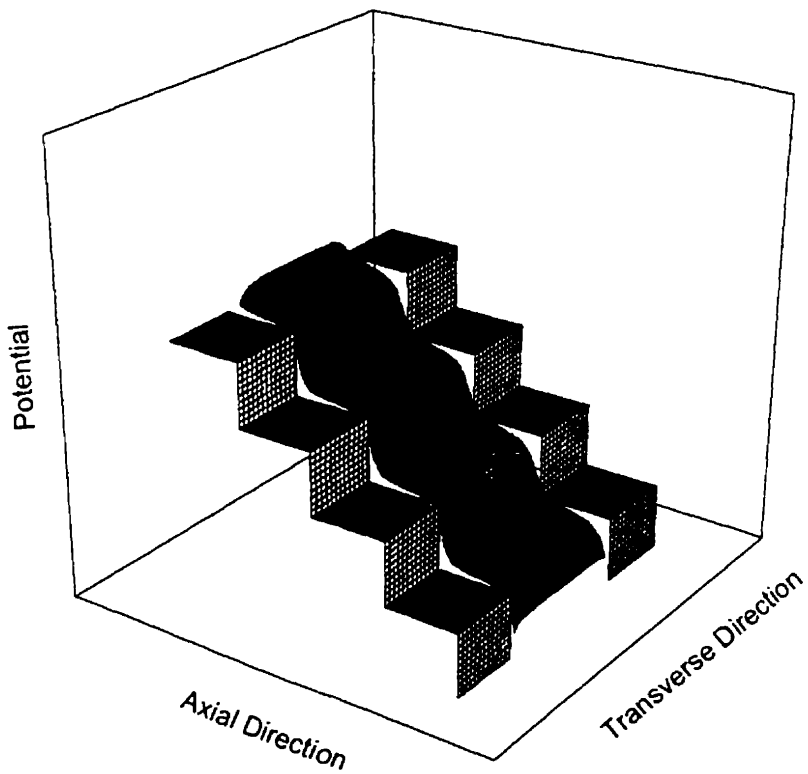

Fig. 3.4 Graph of the potential surface on the plane between two segmented rods, showing the smooth gradient on axis. The steps correspond to the bias voltage on individual rod segments. The equipotential lines reveal slight field imperfections only near the rod surfaces but are nearly parallel in the middle.

3.1.3 Miniature Quadrupole System

The miniature quadrupole system is an ingenious device developed by Kim and Moore [Kim97] to transport ions from one vacuum stage into another with only minor disturbances to the quadrupolar field in which the beam is confined. Essentially, this is done by inserting small hyperbolic vanes into the end of the first set of quadrupole rods. These small vanes are mounted on a holder that forms a vacuum interface between two pressure regimes; hence any gas flow is restricted to within the aperture created within the four vanes.

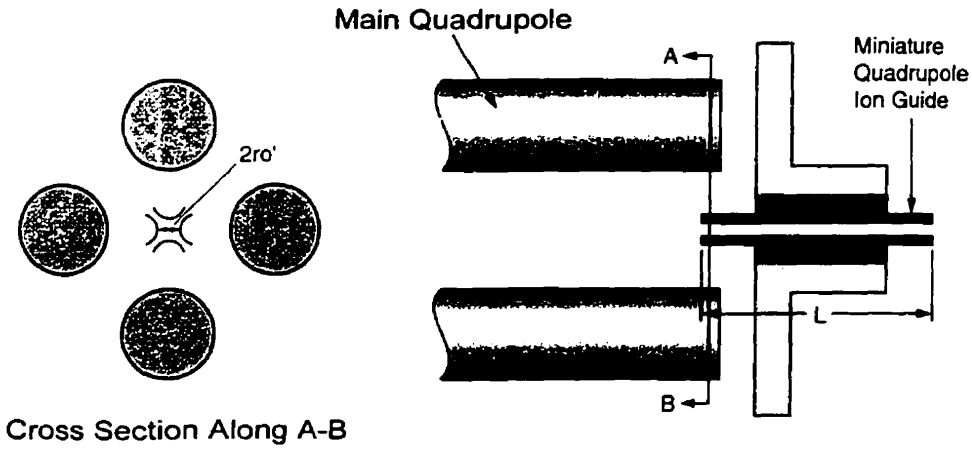

Fig. 3.5 Miniature quadrupole assembly. The cross-sectional view (*at left*) demonstrates how the miniature quadrupole matches the equipotential field lines without disturbing the quadrupolar field. The miniature quadrupole holder serves as the vacuum separator between to pressure regimes (*at right*).

The quadrupolar field is maintained through this aperture by applying appropriately scaled AC voltages to the hyperbolic vanes, which themselves follow the equipotential lines at that radius. In this way, the quadrupole field at the vane entrance is only minimally disturbed and the ion beam passes through the miniature quadrupole and emerges in a new pressure regime, always remaining confined by the nearly quadrupolar field.

3.2 Ion Trapping and Pulsing System: LTRAP

As mentioned in the previous section, the quadrupole beam guide offers a degree of freedom in the shape of the axial electric field. Again, taking advantage of this fact, the LTRAP system was designed to shape the axial field into a trapping potential, causing the ion beam to collect into a cloud. The LTRAP rods were also placed in a low pressure buffer gas environment so that the low energy collisions between Cs^+ and N_2 would assist in cooling the beam into a cloud in the center of the axial trap. Finally, after a sufficient collection time, LTRAP would then pulse the cloud out in with a fast, primary extraction voltage (30V to 200V).

A basic design criterion for LTRAP was that it be weak enough to result in the ion collection being of sufficient volume to be probed by a TOF system with reasonable time resolution. This is a lesson from the work of Lunney [Lun92] where the TOF system was designed to probe an ion collection that was, based on previous publications of studies of such collections, much larger than it actually turned out to be. Thus the design of LTRAP differs from that of a working TOF mass spectrometer, where the trap would be made as strong as possible so as to render the ion collection into the smallest possible volume.

3.2.1 Principles of an Axially Trapping Beam Guide

Continuing with the pseudopotential well model for the radial confinement of a quadrupole ion beam guide, an axial potential well can be easily introduced. Starting from the equation for the pseudopotential (2.39), the effective potential can be expressed as

$$V(x)=\frac{qV_{RF}}{8}\frac{x^2}{x_o^2} \quad \text{and} \quad V(y)=\frac{qV_{RF}}{8}\frac{y^2}{y_o^2}$$
$$V(r)=\frac{qV_{RF}}{8}\frac{r^2}{r_o^2}, \quad \text{where } x_o = y_o = r_o \tag{3.3}$$

Thus near the axis of the quadrupole beam guide the pseudopotential can be viewed as a radially confining system and the transverse (x, y) coordinates replaced by the radial r coordinate.

In the same manner as the axial field in section 3.1.2, an axially trapping potential can be introduced by biasing specific rod segments in order to form a parabolic potential on axis. Consider the simplest case of biasing three segments in a row, assigning voltages 0, $-V_{DC}$, 0 respectively. To first order the potential created on-axis expressed in terms of the distance z from the center of the middle segments can be expressed in terms of a parameter a as

$$V(z) = aV_{DC}z^2 \tag{3.4}$$

This relationship can be expressed in a more easily visualized form by expressing the a parameter in terms of z_o, an effective axial length of the well:

$$V(z) = \frac{V_{DC}}{z_o^2}z^2 \tag{3.5}$$

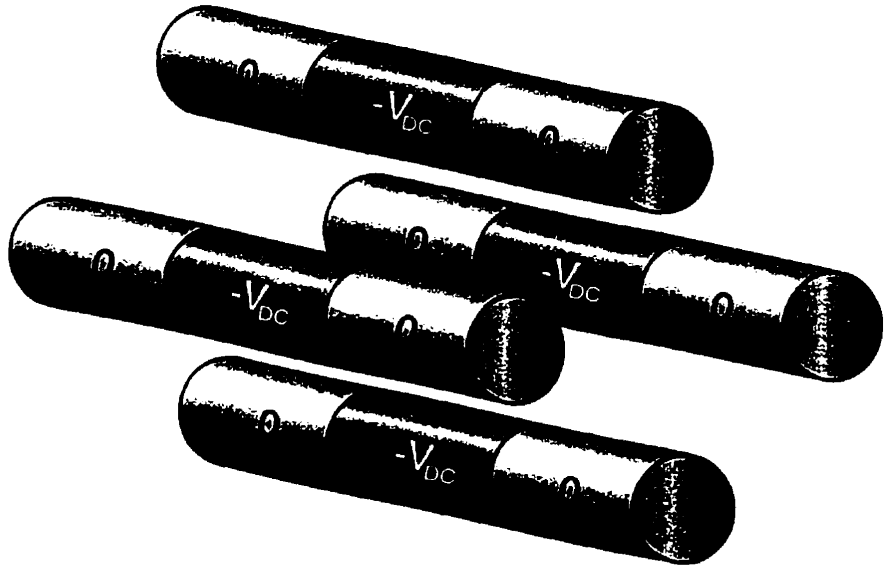

Fig. 3.6 Assigning a trapping voltage $-V_{DC}$ in an axially confining rod configuration.

However, this is only true for the potential on-axis. Moving slightly off-axis, it becomes necessary to consider the effect of Laplace's equation, since a focusing field in the axial direction necessarily causes a defocusing field in the radial direction.

$$\nabla^2 V(r,z)=0$$
$$V(r,z)=\frac{V_{DC}}{z_o^2}\left(z^2-\frac{r^2}{2}\right) \tag{3.6}$$

Combining the effects of this axially trapping potential with the radial pseudopotential from (3.3), the overall potential can be expressed as

$$V_{LTRAP}(r,z)=\frac{V_{DC}}{z_o^2}z^2+\left(\frac{qV_{RF}}{8r_o^2}-\frac{V_{DC}}{2z_o^2}\right)r^2 \tag{3.7}$$

As can be seen, this equation introduces a new condition for stability for the LTRAP system, since it is possible for the defocusing force of the axially trapping potential to overpower the confining force of the pseudopotential. This stability condition for the minimum V_{RF} needed is

$$[V_{RF}]_{\min}=\frac{\omega r_o^2}{z_o}\sqrt{\frac{2mV_{DC}}{e}} \tag{3.8}$$

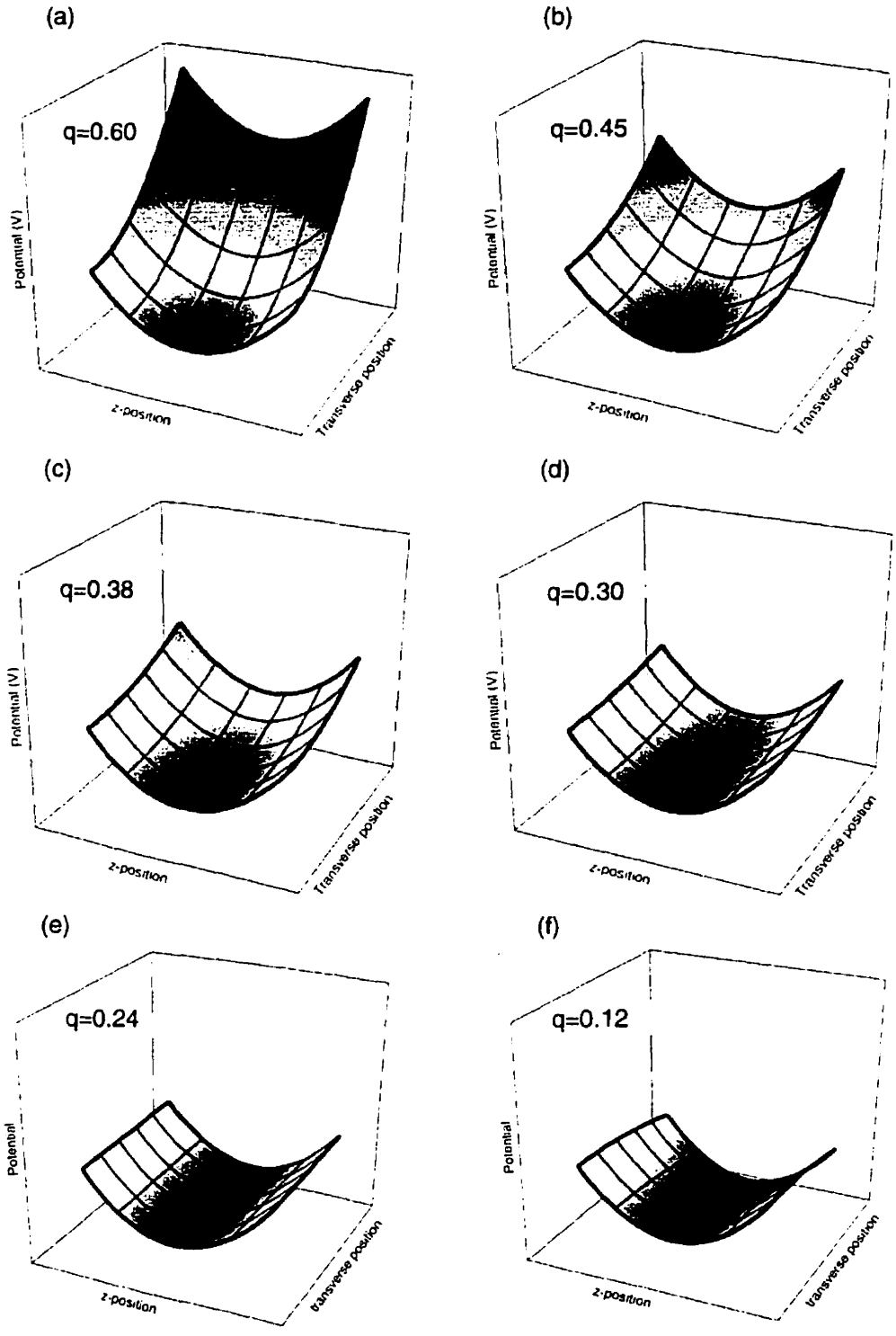

Fig. 3.7 Pseudopotential and axial trapping potential. The graph represents the potential within the region defined by $0 \leq r \leq r_o$ and $-z_o \leq z \leq z_o$. Figures **(a)** – **(d)**: Stable trapping conditions. Figure **(e)**: Critical trapping condition. Figure **(f)**: Unstable condition; the axial field causes a defocusing force greater than the pseudopotential.

3.2.2 Segmented Rod Structure

The segmented quadrupole rod structure that makes up LTRAP was constructed out of 36 segments (9 per rod) of stainless steel cylinders, 15.85mm outer diameter, 9.8mm inner diameter and 15mm in length, in a configuration as shown in Fig. 3.8. The segments themselves were held in place by an insulator rod that ran through the middle of the cylinders and a 0.1mm mica washer separated each segment from its neighbors. A breakdown voltage across adjacent segments was tested and found to be $500V_{DC}$ in atmosphere. The rods were mounted on a support structure so that the minimum distance between opposite pairs was 14mm, resulting in an r_0 of 7mm.

Each segment was electrically shorted to its paired segment, situated at the same location on the opposing rod, by a 2.5mm wide strip of 0.002" stainless steel shim. Individual voltage feeds were introduced to the segment pairs by rigid steel wires (1.6mm OD) so that the DC and AC voltage of each segment pair could be controlled separately. The wires were bent and shaped in such a way as to maximize the inter-wire distances in 3 dimensions, while maintaining enough rigidity to prevent vibrations of the wires in the vacuum from causing momentary shorts. Photographs showing the rods and the wiring configuration are shown in Fig. 3.9 and Fig. 3.10.

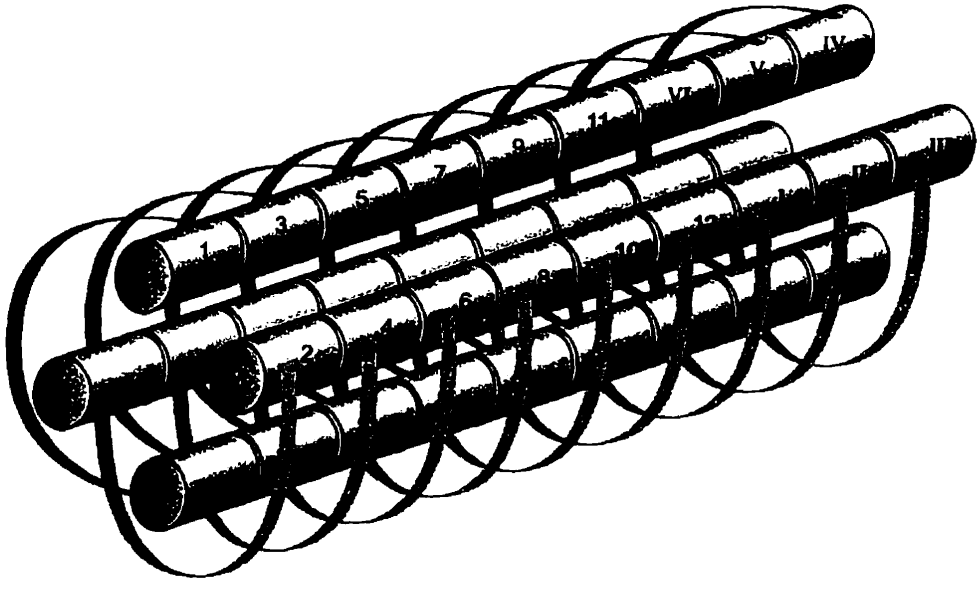

Fig. 3.8 Schematic view of LTRAP, showing rod segments being paired by connector bands. Segments I-VI form the axial trap at the end of the rods.

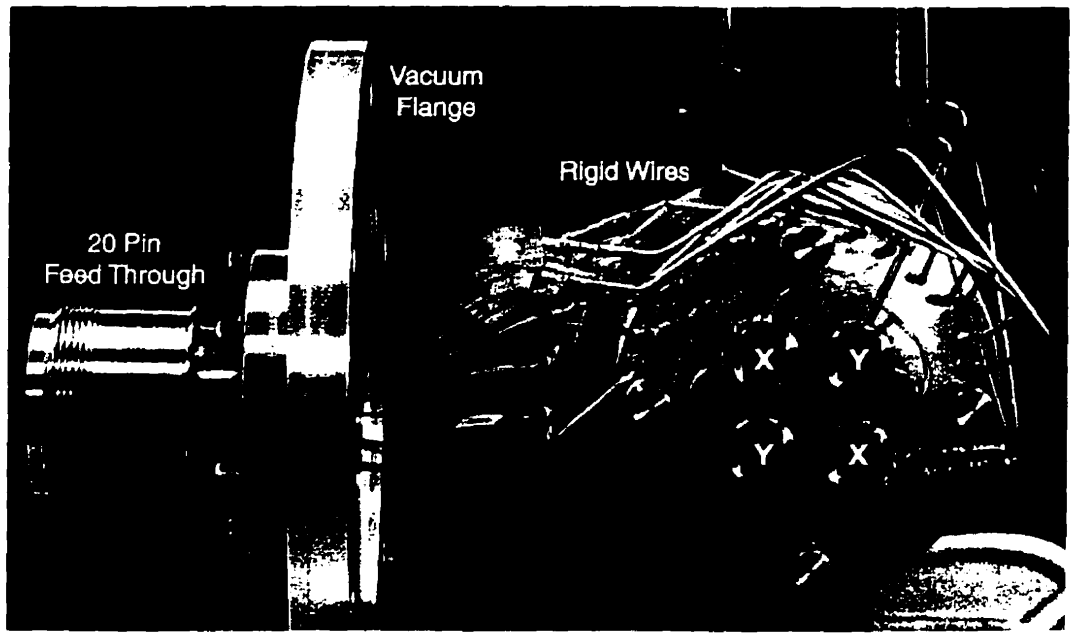

Fig. 3.9 End view of the LTRAP assembly and rigid wire connectors in mock set-up.

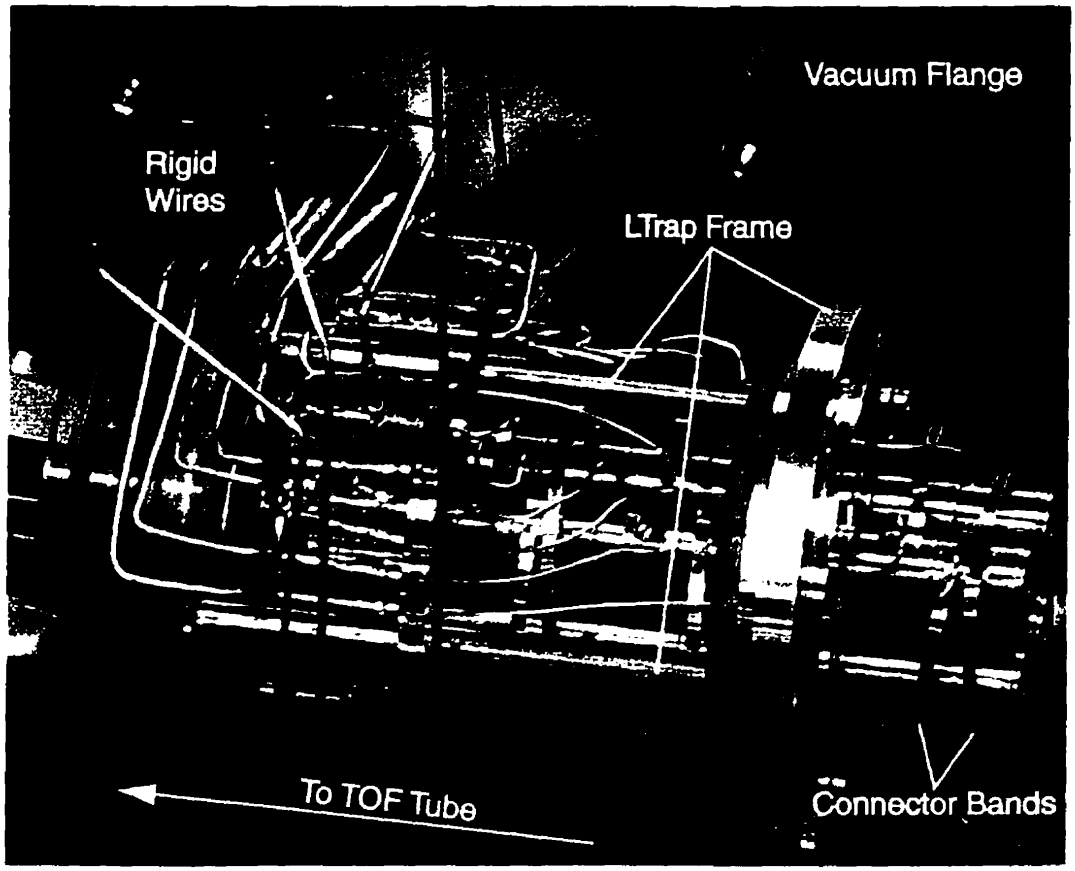

Fig. 3.10 Side view of the LTRAP assembly and connectors.

3.2.3 Electrical Systems

In order to achieve the RF quadrupole field in the rod structure it was necessary to feed in two sinusoidal RF voltages to the segment pairs, one for the x rods and one for the y rods running 180° out of phase with that for the x rods. This resulted in all of the segments running together as four continuous quadrupole rods. On top of this AC signal, it was necessary to couple a DC bias onto each segment pair, the bias level being determined by the segment pair's location along the axis. Lastly, for the trapping and pulsing of the ion cloud, the final three segment pairs had to be specially coupled to a pulsing system.

RF and DC Signals

For the first six rod segment pairs, the AC signal was generated by an SRS DS345 synthesized function generator, creating a –5V to 5V sine wave, which was then fed into a custom designed Nikkinen HVAmp RF power amplifier, outputting the full strength sine wave. This signal was then sent into a high Q center-tapped transformer, which was used to split the signal into two opposite phased sine waves. These two RF signals (typically $200V_{pp}$ at 800kHz) were then fed in parallel to each of the segment pair through 0.1μF capacitors to block out any DC bias from entering the RF line. This resulted in an RF amplitude of 200V between adjacent rods.

The DC bias voltages were generated from a 28V DC power supply that was floated 22V below ground. This DC power supply then fed six 150kΩ potentiometers in parallel, which could each vary its output voltage between –22V to 6V. In this way, the individual segment pairs could have its DC bias voltage controlled separately for optimum field shaping. Note that the x and y segment pairs are DC linked so that the same DC bias voltage were sent to both the x and y pairs that have the same position along the rod. Finally, the bias voltages were connected to the segments through 2.4mH inductors to block out any RF voltage from entering the DC line. (Fig. 3.11)

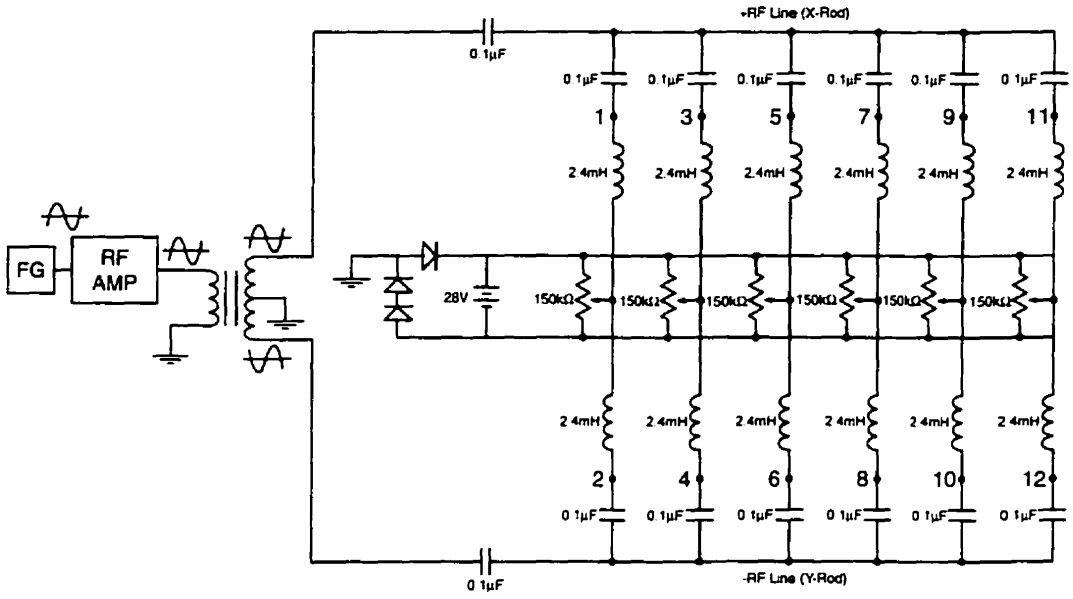

Fig. 3.11 Circuit diagram detailing how the RF signal and DC biases were coupled and fed to each rod segment (points 1-12).

Pulsing and Timing Circuits

For the last three segment pairs on the *x* and *y* rods which formed the axially trapping potential, it was necessary to have electronic systems which could handle both the collection mode and the extraction mode of the LTRAP device. In trapping mode, the segments needed to have RF potentials that were the same as for the rest of the rod segments and DC voltages that were appropriate for trapping. In extraction mode the RF must be turned off while the DC was set to pulse out the trapped ion cloud.

The RF signal for the trap segments were generated by a second SRS DS345 function generator whose timing circuit was coupled to the first to allow for the synchronous operation of the two. The sine wave was then sent to an ENI 325LA RF amplifier to increase the power of the signal. That signal then drove the primary coils of three high *Q* transformers, fed in parallel, to generate the opposite phased signal as before. Each transformer was set to run only one *x* and one *y* pair of segments, and the DC bias for that segment was set by the DC voltage of the center-tap of the transformer. The transformers were wound by hand and tuned so that each of the cores would have the same response to the primary signal and the amplification of all three agreed to within 10%. (Fig. 3.12)

The center-taps of the three transformers were what defined the behavior of the trap during the extraction phase. The first and third transformers had their center-taps connected to two Nikkinen HVSwitch supplies (20ns risetime, 15ns falltime) that pulsed up or down when the trigger pulse was set. The first switch was normally set to low voltage (-1V) to allow ions into the trap and then pulsed high (+10V to +90V) to generate a soft primary extraction field. The second switch, which controlled the third segment pair, was normally set high (+5V) to prevent ions from overshooting the trap, and was pulsed low (-20 V to –110V) to complete the primary extraction gradient. The middle transformer core had its center-tap biased to a constant voltage during collection and extraction, which set the axial well depth of the trap (–10V). In addition, the plate electrode immediately after the trap segments which formed the entrance to the secondary extraction stage was also pulsed from 0V during collection to –410V during extraction by a high voltage pulser.

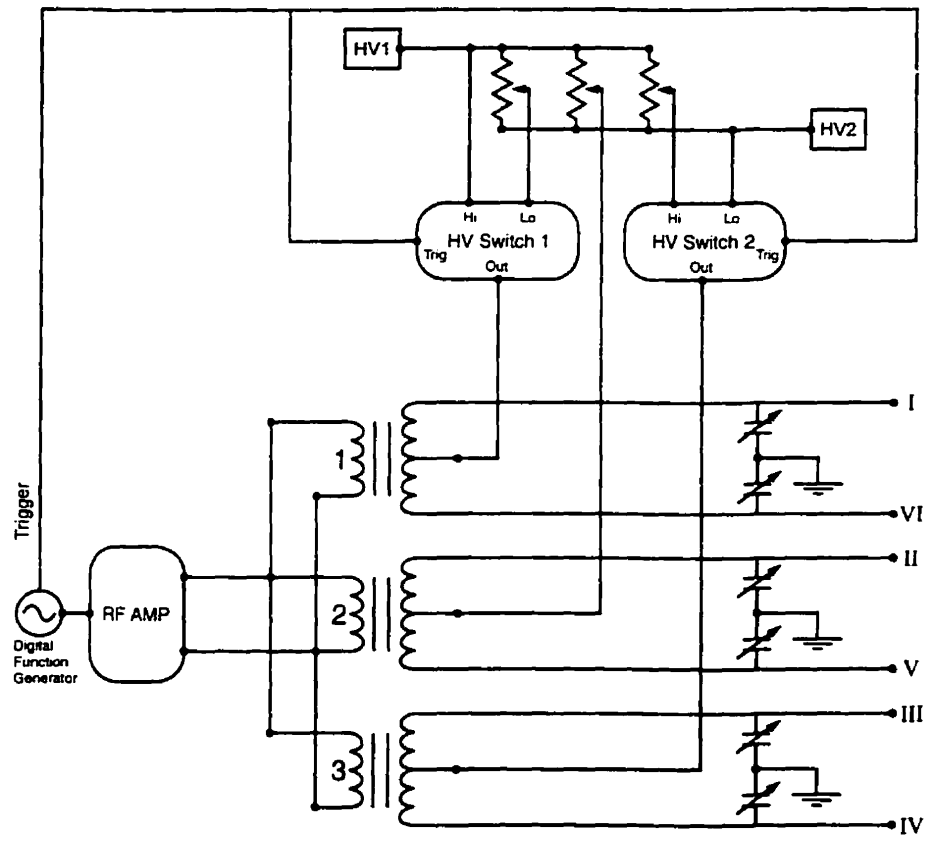

Fig. 3.12 Circuit diagram of 3 transformers. Center taps are controlled by HV switches that pulse the segments up/down. These transformers control the voltages for the 3 LTRAP segments (I-VI)

The timing of the system was controlled by the primary SRS DS345 function generator, using the output trigger signal to control the other devices. The function generator was set to trap ions for a duration that varied between 5ms to 50ms and then to create a 10μs extraction pulse. The RF signals were set to zero just before the extraction pulse began because the transformers continued to ring a little after the primary signal dropped to zero. This configuration ensured the cleanest possible extraction pulse to avoid field imperfections from affecting the time-of-flight. The two high voltage switches and the high voltage pulser were similarly triggered to their extraction modes by the primary trigger signal.

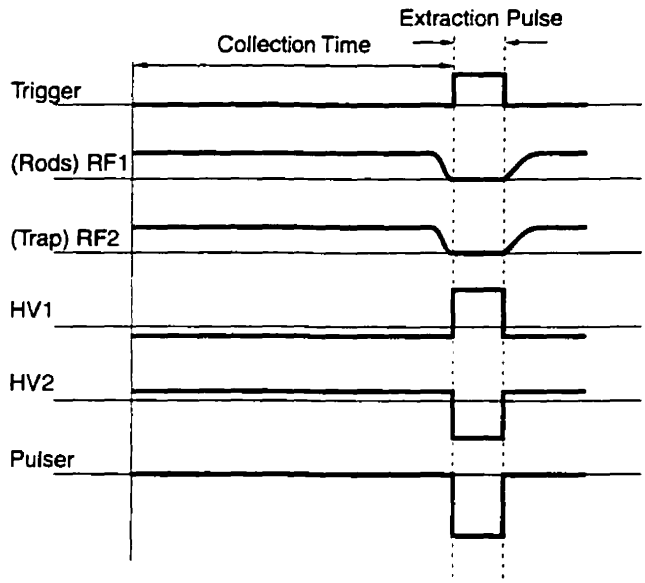

Fig. 3.13 Sequence of operation for LTRAP collection and extraction.

3.3 Time-of-Flight System

The Time-of-Flight system was essentially a diagnostic tool for probing the action diagram of the collection of ions extracted from LTRAP. The TOF tube was situated immediately after the last LTRAP rod segment and consisted of a secondary extraction region followed by a 1m drift tube. A custom-made chevron-stacked multichannel plate assembly was placed at the end of the TOF tube to detect the ion collection at the end of its flight. The following sections will detail each component of the time-of-flight system.

3.3.1 Time-of-Flight Tube

The flight tube entrance consisted of a secondary extraction region, defined by the entrance plate and an extraction mesh. This secondary extraction was placed at the theoretical time–focus (section 1.3) of the ion packets as they were extracted from LTRAP. This entrance plate was located 15mm away from the last set of segments from the LTRAP rods and had a 3mm aperture. It served as a vacuum separation between the LTRAP system, which had a buffer gas pressure of 0.4mTorr, and the TOF tube, which was at 2.5μTorr. This entrance plate was normally held at 0V during the collection phase to inhibit any fringing fields from the TOF tube from pulling the ions out of the trap. It was pulsed down to –410V during the extraction phase to provide the front voltage for the secondary extraction region.

The extraction mesh used was made from 2μm stainless steel wires with a grid spacing of 20μm. The extraction mesh was positioned 15mm after the entrance plate and it was electrically coupled to the time-of-flight tube, which had a voltage of –2.5kV. After the extraction mesh, the ions entered the drift region, which was defined by a stainless steel tube (70mm OD, 66mm ID) that was approximately 1m in length.

3.3.2 Deflection Plates

Given the accuracy to which the axes of LTRAP, the extraction field and the flight tube could be aligned, it was necessary to install deflection plates to steer the extracted beam exactly along the flight tube. For this, two sets of parallel plates were positioned inside the flight tube immediately after the extraction mesh (Fig. 3.14). After the first set of deflection plates, the second pair was set orthogonal to the first, to allow for the steering of the ion packet in all transverse directions during its flight. Each plate was 40mm (axial) by 50mm (transverse) and was held at a separation of 24.5mm from its partner. A $28V_{DC}$ supply was floated on top of the flight tube bias potential (-2.5kV) and a potentiometer divided this voltage between the two deflection plates so that the mid-plane between them had the same voltage as the flight tube bias. This was to ensure that the ions passing exactly on axis did not experience any acceleration in the axial direction.

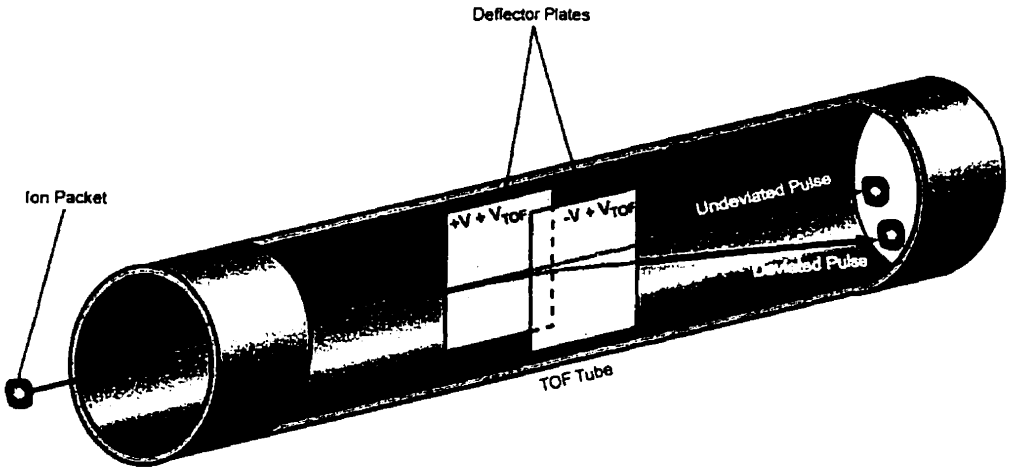

Fig. 3.14 A pair of deflector plates inside the flight tube. Adjusting the voltage between the plates 'steers' the ion packet as it continues down the drift tube.

3.3.3 Einzel Lens

An einzel lens was added to the TOF system to achieve better focusing of the ion packet onto the detector. The lens itself consisted of a hollow aluminum cylinder (ID 42mm, OD 48.5mm) 50mm in length situated after the second pair of deflector plates. This is unfortunately not the ideal location for an einzel lens because the focusing properties of the lens would now counteract, to some extent, the deflection due to the plates. While both the deflector plates and the einzel lens systems work just as well in this configuration, it becomes more difficult to decouple the effects of both systems to recover the original packet. Thus, logically, it would have made more sense to have the einzel lens before the deflector plates but the choice of configuration was dictated more by wiring and mounting considerations than by purity of separation of function.

Note that the axial component of the packet's motion, and hence the actual time-of-flight, is unaffected by the einzel lens and the deflector plates, only the radial extent of the pulse is affected. Further discussion of how the two systems were used will be presented in the following chapter.

3.4 Ion Detection and Data Acquisition

High time-resolution ion detection was of central importance to this time-of-flight work, as every measurement hinged on the accurate determination of when and how many ions arrived at a fixed point in space, the detector. The choice of detector was a chevron-stacked microchannel plate (MCP) detector, which had the desired characteristics of fast rise-time for accurate timing, and high amplification for detecting small amounts of ions, even for single-ion counting. The electron shower resulting from the ion collection entering the MCPs was collected and the resulting signal was treated and amplified for analysis. Most of the experiment was done with a digital oscilloscope, while single-ion counting for detector calibration was done with a multi-channel analyzer. The following sections will present the details of each component and their functions.

3.4.1 Microchannel Plate Assembly

Two Galileo microchannel plates were used for this experiment. Their physical characteristics are summarized below:

Characteristics	MCP1	MCP2
Outside Dimension	32.74mm	32.74mm
Minimum Quality Area	25.00mm	25.00mm
Channel Diameter	10μm	10μm
Center to Center spacing	12μm	12μm
L/D Ratio	40:1	40:1
Bias Angle	12°	12°
Thickness	0.43mm	0.43mm
Gain at 900V	7.7×10^3	7.0×10^3

Table 3.1 Microchannel plate characteristics.

The plates were mounted on a custom-made MCP assembly, designed to have as small an axial profile as possible. This avoided the possibility of any signal delay from the end of the MCP to the stainless steel anode detector and reduced noise that could enter from surrounding sources. To accomplish this, a sandwich-type of assembly was designed, where the plates were placed in between stacks of stainless steel connector rings, copper contact rings and ceramic insulator rings. (Fig. 3.15)

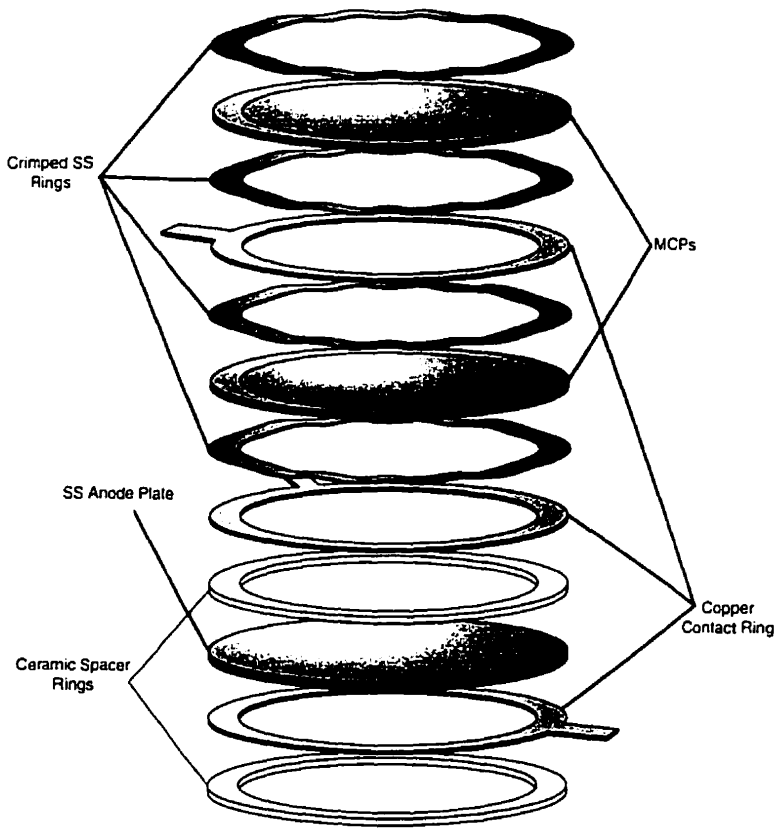

Fig. 3.15 MCP assembly diagram.

The connector rings were made from 0.2mm stainless steel shim and were crimped in a radial pattern to introduce a slight spring quality to the connectors. This was to protect the mechanically brittle MCPs, which tended to crack if a slight unevenness in pressure arose during the stacking of the assembly. The entire stack, including the stainless steel anode and three stainless steel mounting plates, was no more than 8.5mm thick (Fig. 3.16). This is one of the thinnest such detector arrays that has ever been reported.

An entrance mesh defined the field just before the first MCP, which was biased to the voltage of the flight tube, so the ions experienced minimum field disturbance as they drifted towards the detector. The MCPs were biased so that there was a +1kV difference between front and back surfaces of each plate for optimum signal detection.

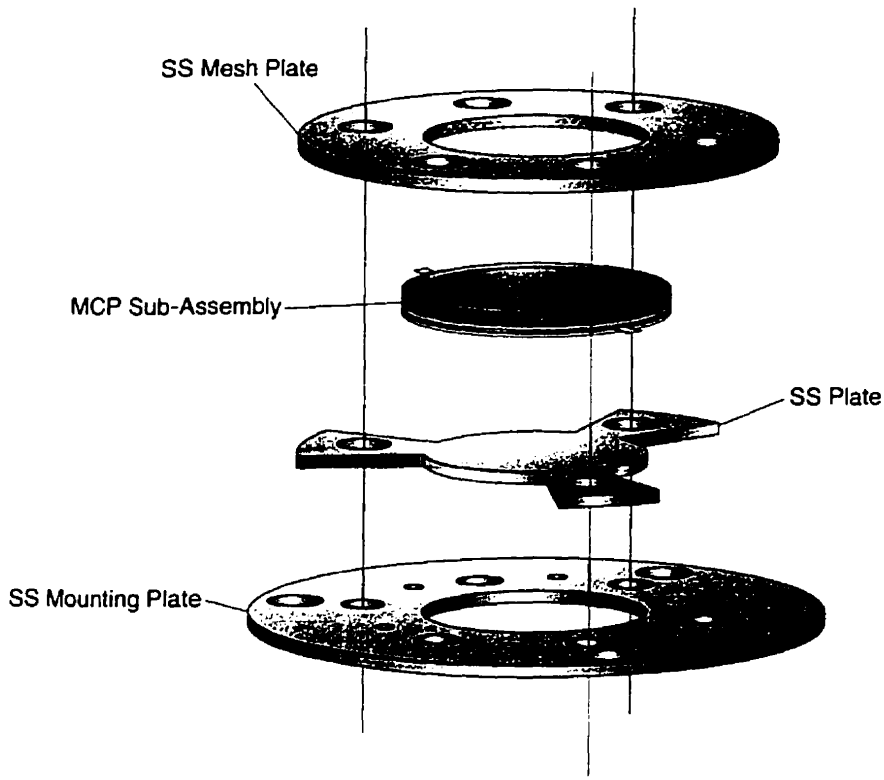

Fig. 3.16 MCP detector assembly diagram.

3.4.2 Signal Detection and Data Acquisition

Following the MCPs, the stainless steel anode collected the electron shower produced by the incoming ion packet and created a signal suitable for processing. Usually, this meant sending it to ISOAMP, which amplified the signal by a factor of 10. Depending on the number of ions arriving at the detector these signals would then either pass through an attenuator (6dB or 12dB) or continue unattentuated to the digital oscilloscope. The scope was a LeCroy 9310M 300MHz digital scope, capable of digitizing a signal with 10ns resolution in Normal mode, or 0.1ns resolution in Random Interleaved Sampling (RIS) mode. For normal time-of-flight work, this was the method of signal detection, and most of the data presented in this thesis was taken in this manner.

To calibrate the gain of the MCPs, it was necessary to modify the detector system to record single-ion counts on a multi-channel analyzer (MCA). To do this, the signal from the anode was sent to a Canberra 1415 ×50 pulse amplifier which triggered a NE Pulse Generator. The pulses from the generator had heights that were proportional to the input pulse from the amplifier, and so were suitable for processing in the Canberra Omega 1 multi-channel analyzer. Delivering a calibration pulse of a known voltage from a function generator allowed the pulse height channels to be calibrated to voltages. In turn, this helped identify the voltage height of an individual ion pulse amplified through the MCPs and to calculate their gain.

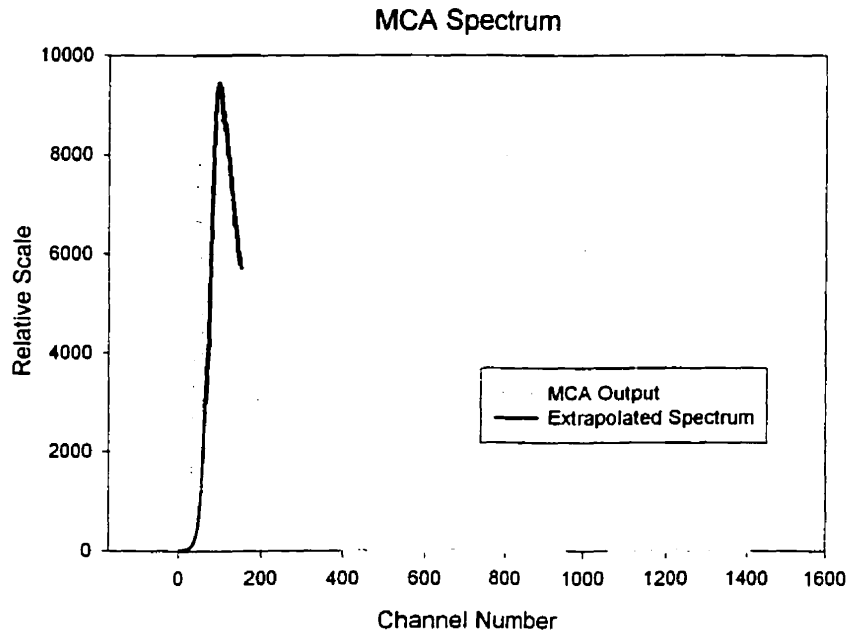

Fig. 3.17 Multi-channel analyzer spectrum of pulse heights. The calibration peak is at channel 1008 while the single ion peak is at channel 149.

Fig. 3.17 shows the MCA spectrum of both the calibration peak and the single ion peak. The noise peak was removed by extrapolating the distinguishable portion of the single ion peak and then by taking a weighted average of all the channels, obtained the representative pulse height of an individual ion signal. The calibration pulse height was 2.75mV, the ratio between the calibration peak channel and the ion peak channel was 6.75 and there was a signal reduction by a factor of 1.4 due to the loading of the pulser to the system. Thus the single ion peak was determined to have a 57mV pulse height.

Ideally, the calibration would be completed by capturing a single ion pulse with a pulse height of 57mV with the digital oscilloscope. However, it was impossible to obtain a stable reading of a single ion pulse because of the difficulty in triggering. From the MCA spectrum, it is obvious that setting the oscilloscope trigger at a level lower than the ion peak height would run into the noise region, causing the oscilloscope to sample noise peaks with peak heights lower than 57mV and therefore yield an unstable signal. Setting the trigger above the peak gave a pulse height that was higher than the desired value of 57mV, as only the high pulse height ions would be sampled. The way to compensate for this was to take an ion pulse when the trigger was set high and scale the pulse down to the true value as obtained by the MCA spectrum. It should be noted that this was only possible since each single ion detection created a pulse shape that was essentially the same in the time profile, only differing in the voltage scale, meaning the vertical component of the pulse shape was scaled up and down. Thus, scaling the pulse height of a single ion profile to 57mV and then determining the area under the principle peak yielded a calibration for the MCP gain of approximately 3.75×10^{7}, with an accuracy of about 7%.

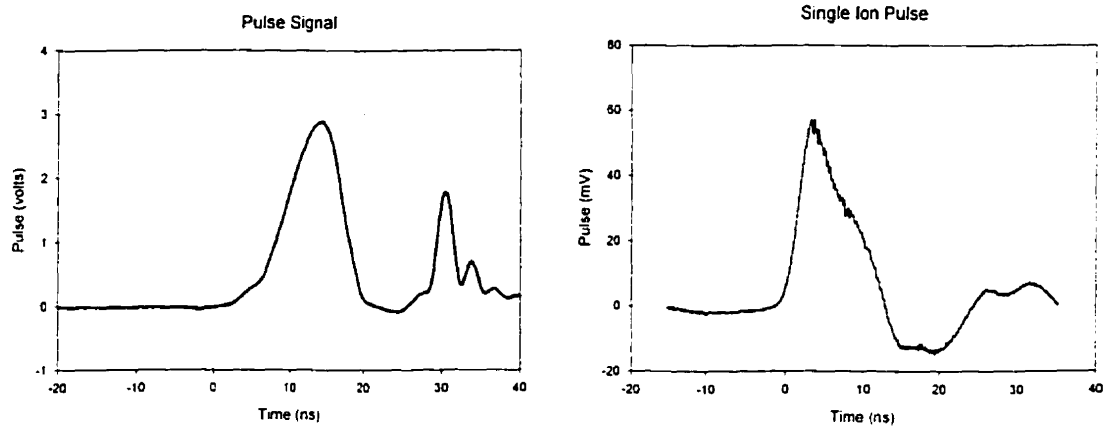

Fig. 3.18 Calibrating pulse (*left*) and adjusted single ion pulse (*right*).

3.5 Vacuum Considerations

The vacuum systems for this experiment were also critical to the performance of the LTRAP. In the first region, the cooling quadrupole rods required relatively high buffer gas pressures (40mTorr). This was necessary to arrest, cool and focus the incoming ion beam from the heater source into a cool beam of about 0.05eV [Kim97].

In the LTRAP system, there still needed to be a small amount of buffer gas to remove enough axial energy from the beam so that it would be trapped in the middle of the axial potential well. Experimentally, the required buffer gas pressure was found to be 0.1mTorr. Typically, the LTRAP region was operated at 0.5mTorr to efficiently capture the ions in the trap. For the time-of-flight performance, it was necessary to be in as high a vacuum as possible, so that the scattering of the ion packet is negligible. However, because this system must allow for an aperture between the LTRAP region and the TOF region, the lowest possible pressure obtainable was dependent on the pressure in LTRAP. Typically, the vacuum in the TOF tube was 2.5μTorr.

Because the system needed a constant flow of buffer gas, the vacuum in the cooling quadrupole region was achieved by a 12" diffusion pump (CVC PVMS-1000A, 5300L/s) backed by an Alcatel 2021 mechanical pump (14.6CFM). The pressure here was monitored by a Penning vacuum gauge (CVC GPH-320C). The miniature quadrupole that coupled the cooling quadrupole rods with the rods of LTRAP had a buffer gas conductance equivalent to a 5mm-diameter tube, 8mm in length. This allowed the pressure difference to be maintained between the cooling rods and the following section.

The LTRAP system also had its own buffer gas intake, so that the pressure here could be controlled independently of the cooling buffer gas pressure. The buffer gas intake was controlled by a NUPRO SS-4BMG needle valve, which was adequate for most pressure adjustments but presented difficulty when very fine control of buffer gas pressure was needed. The system was pumped by a Varian V60 turbo pump (60L/s). The vacuum separation between this pressure region and the time-of-flight tube was a 3mm aperture in the entrance plate that made up the front electrode of the secondary extraction region. On the other side of this vacuum separation was the TOF tube, which was pumped by a Varian V250 turbo pump (250L/s). This arrangement was sufficient to bring the pressure in the TOF tube down to 2.5×10^{-6} Torr, which was acceptable for TOF measurements. Both turbo pumps were backed by an Alcatel 2015 (10.6CFM) and their pressures were monitored by Varian 571 BA ionization gauges.

Chapter 4 Computer Modeling and Simulations

The computational tools and techniques required for the analysis of the experimental data will be presented in this chapter. As outlined in Chapters 1 and 2, the procedure is to construct a model of the phase space distribution of the ion cloud within a linear RFQ trap based on physical theories regarding this distribution. This model is then adjusted until the computer simulation of the response of the TOF detector duplicates the actual signal observed for a given ion collection in the trap. This then becomes a test of both the computer simulations and the physical theories upon which the model is based. If the simulations do duplicate the observed signals for a range of experimental conditions then it is likely that indeed the theories are valid. The model can then be extended to the experimental conditions within a working TOF mass spectrometer design to predict what its performance will be

4.1 Modeling Phase Space

The initial starting point for the simulation is the collection and trapping of ions within the pseudopotential well of LTRAP. In order to characterize the ion cloud, some simplifying assumptions had to be made. The pseudopotential well was assumed to be symmetric in the axial direction, relative to the trap center, when in reality, there is a slightly higher potential at the farthest trap segment to ensure the capture of the ion cloud. Secondly, there was the assumption that everything happened near axis so that field imperfections could be safely ignored. That is to say that the ion cloud cooled to a small

enough radial extent that the pseudopotential well model was indeed accurate. Also, the ion distribution was assumed to not be affected by space charge forces, i.e. the effect of ion-ion repulsion. This last assumption is perhaps the most serious in limiting the validity of the model but to date no feasible computer simulation has been developed for space charge effects in a RF quadrupole trap.

4.1.1 Field Calculations for the Pseudopotential Well

The actual voltage values within the region of the trap were calculated using a finite-difference technique with successive over-relaxation, which was employed by SIMION 6.0, one of the software packages used in this experiment. The technique involved applying a three dimensional grid of points, in this case 0.25mm apart, on top of the volume of interest, which was 48mm x 48mm x 75mm in total. This simulated volume included one set of rod segments prior to the trap, the 3 sets of trap segments, the extraction plate and the extraction mesh electrode. The points that fell within the spaces occupied by the electrodes were then assigned specific voltage values, according to the trapping conditions, and then the rest of the points were allowed to 'relax' to their true voltage values. For an overview of the actual algorithm used in the program, the reader is directed to the reference by Dahl [Dah95].

This technique of over-relaxation only provided the DC axial trap, since the oscillating RF field could not be easily implemented this way. Therefore, the on-axis values of the trap were taken from the SIMION calculations and an analytical function of the form $V(0,z)$ was fitted to these potential values with an error of 0.1%.

$$V(0,z) = (az^2 + bz + c) \cdot V_{DC} \tag{4.1}$$

where V_{DC} is the DC potential between the middle trap segment and the end segments of the trap. The results of this fit for a, b, and c respectively were 0.00622, 0.001502, 0.16667. This was the on-axis DC component in equations (3.5)-(3.7).

The radial component of this on-axis potential arises only from the quadratic term a, since b and c do not contribute to Laplace's equation. Therefore the DC component of the potential near axis can be described as:

$$V(r,z)=V_{DC}\left[a\left(z^2-\frac{r^2}{2}\right)+bz+c\right] \tag{4.2}$$

and the full potential, including the pseudopotential confinement:

$$V(r,z)=V_{DC}\left[a\left(z^2-\frac{r^2}{2}\right)+bz+c\right]+\frac{qV_{RF}}{8r_o^2}r^2 \tag{4.3}$$

Applying this equation at every non-electrode point on the grid, the full trapping potential was expressible in terms of very simple parameters: the (x, y, z) coordinates, the applied axial trapping potential V_{DC} and the applied RF potential V_{RF}. This formula was then implemented into a spreadsheet calculation using MS Excel to generate the values of the potential at the grid points in the trapping region.

4.1.2 Temperature Calculations: σ_z and σ_{p_z}

Having simulated the potential within the trap, it then became possible to define the theoretical distribution that the ions would take within this potential. Because the potential is separable into axial and radial coordinates, the distribution also became separable, and the complete distribution could be expressed as the product of the two.

In the axial dimension, the number distribution was merely that of ions within a simple harmonic oscillator with a potential defined by the function above (4.1). In this case, again only the a term played a role in determining the macromotion oscillation frequency ω.

$$m\omega^2 = 2aV_{DC} \tag{4.4}$$

and therefore the axial spatial distribution (eq. (2.59)) was characterized simply by

$$\sigma_z = \sqrt{\frac{k_B T}{2aV_{DC}}} \tag{4.5}$$

The axial momentum distribution was even simpler, since it depended only on temperature T (eq. (2.60)):

$$\sigma_{p_z} = \sqrt{mk_B T} \tag{4.6}$$

In the transverse directions (x, y), the situation was not much more complicated. By inspection, it is possible to see that the transverse distributions also follow the same behavior as the axial distribution where now the spatial spread is governed by:

$$\sigma_x = \sigma_y = \sqrt{\frac{k_B T}{2\left(\frac{qV_{RF}}{8r_o^2} - \frac{aV_{DC}}{2}\right)}} \tag{4.7}$$

and again, the transverse momentum distributions depend only on T:

$$\sigma_{p_x} = \sigma_{p_y} = \sqrt{mk_B T} \tag{4.8}$$

These six σ values were essential to the rest of the simulations because they relate the position and momentum distributions to a single theoretical quantity T, which therefore entirely governs the motions within the simulated ion ensemble. By varying the temperature, the model of the ion ensemble could be fitted to the experimental data.

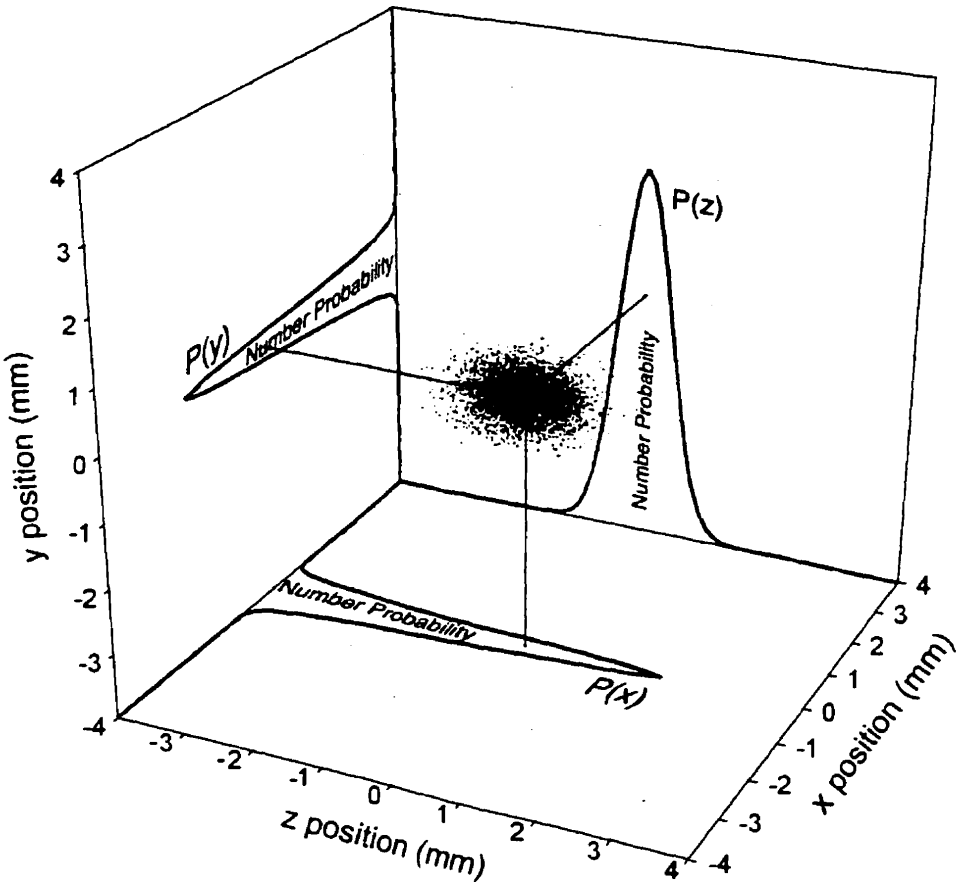

Fig. 4.1 Spatial distribution of a randomly generated ensemble of ions. The full six-dimensional phase space volume occupied by the cloud is the product of the six probability functions and is a function of temperature T.

4.1.3 Representative Particles in Phase Space

As mentioned previously, the goal of the simulation was to obtain a computer generated signal that duplicated the actual signal received at the detector. For that to be possible, it was necessary to carefully model the phase space distribution of the trapped ions in the axial direction (z, p_z). Furthermore, in the computer simulation it is possible to perform the calculations on only a representative set of phase space points. These phase space points were chosen, with appropriate weighting factors, to represent the entire ion cloud distribution as it progressed through the time-of-flight system.

The points chosen to represent the elliptical ensemble depended on the total number of points used in the simulation. For example, the minimum number necessary to obtain any sort of useful information of the phase space distribution would be five: one in the center of the ensemble and one for a selected distance from the origin in each of the four cardinal directions from the origin. The relative weights of the five points would depend on the distance from the origin. One appropriate choice of distance could be $3/2\sigma$, where the center point represents the particles contained within 1σ from the center and the displaced points would represent the rest. The weighting factor would then be 40% for the center point and the remaining four points 15% each.

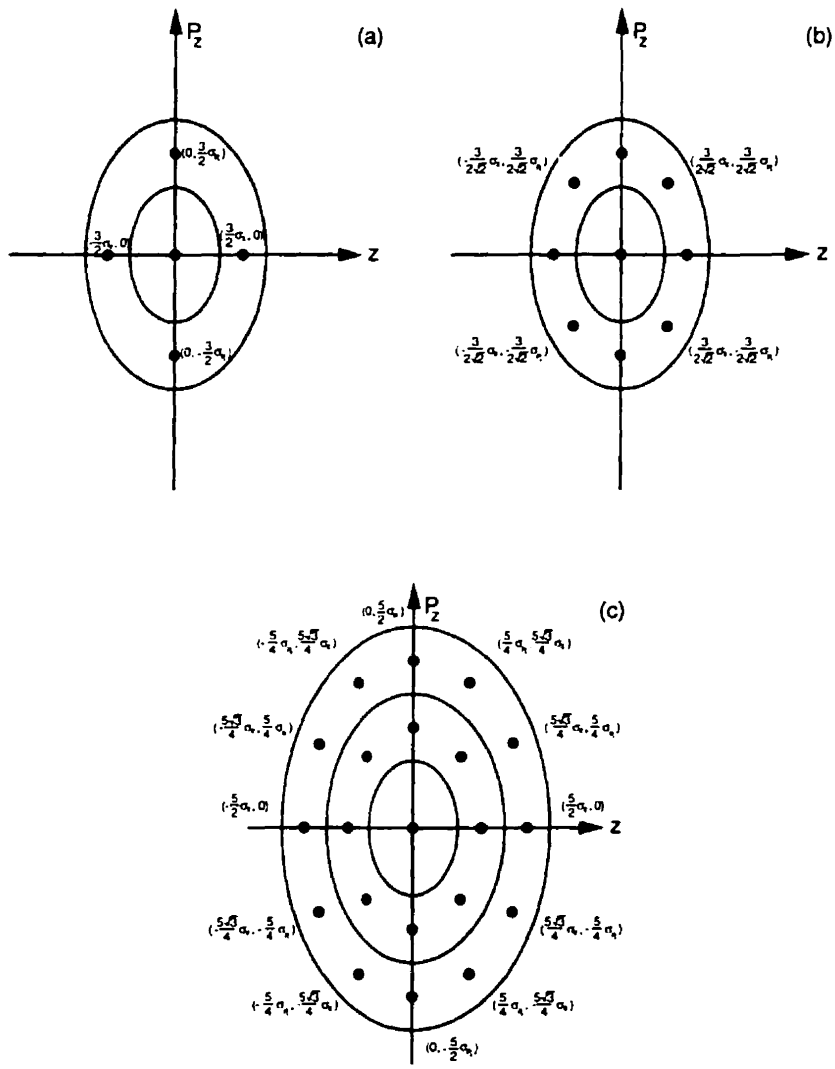

Fig. 4.2 Representative phase space points.
Possible arrangements for: (a) 5 points (b) 9 points (c) 21 points.

A more thorough choice of points would be to select 9 representative points, one in the center, 4 along the axes and 4 along the diagonals. The relative weights of the 8 outer points would then change to 7.5% each. An even more thorough representation would be to include points $5/2\sigma$ away. One choice would be to choose 21 points as in Fig. 4.2. The center point would still have a weight of 40%, the points at $3/2\sigma$ would be reduced to 6% and the outermost points would have a weight of 1% each.

In principle, this method of dividing up the phase space can be carried out *ad infinitum.* In simulations carried out in this work, a set of 1441 representative points was chosen, dividing up a 3.2σ ellipse into equal areas, each point representing only a small weight of the entire ensemble of particles. (Fig. 4.3)

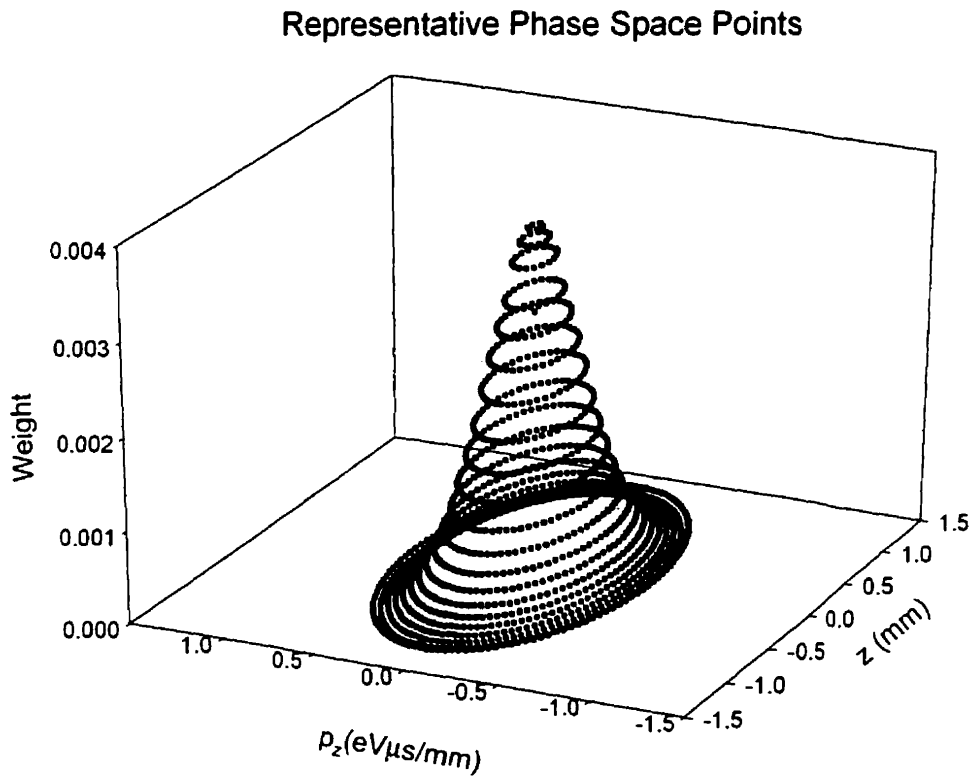

Fig. 4.3 1441 representative phase space points plotted with their weighting factors.

Since the ellipses themselves and the representative points were constructed based on the σ values of z and p_z, the entire simulation was now dependent only on a single variable T. In addition, by using the representative points, the program was able to manipulate each point's phase space coordinates according to the equations of motion and determine the ensemble's behavior as it evolved during its extraction into its time-of-flight. This eventually enabled the simulation to reconstruct a time-of-flight spectrum of the ion ensemble as it reached the detector, a spectrum that was adjustable by varying solely the temperature parameter.

4.2 SIMION Trajectory Calculations

As mentioned before, SIMION 6.0 was the main program used in many of the intensive calculations because it was able to handle the potential arrays and the large number of ions easily and efficiently. In addition, by carefully modeling the actual geometry of LTRAP, SIMION took care of any field imperfections or fringing field effects that were present in the real experiment, but very difficult to model by any analytical method. Therefore, by using the representative phase space points that were generated by Excel as initial conditions for SIMION, the program was able to model the ion extraction.

4.2.1 On-Axis Pulse Extraction

Because time-of-flight analysis, to a very high accuracy, involves only the axial component of the motion of the phase space ensemble, only the z-p_z coordinates were used in the SIMION calculation. That is to say the program dealt only with the on-axis motions of the ions.

Generating the 1441 representative points for various temperatures, ranging from 0.025eV to 0.075eV, the simulation then proceeded to calculate their trajectories during the extraction phase of the LTRAP operation cycle. In the simulation, the trap electrodes were set high/low at time t=0, corresponding to the zero time of the trigger pulse, and representative ions were pulsed out of the LTRAP. Following the trajectories in phase space, the simulation recorded the time evolution of the ensemble as it was extracted in this primary extraction field. The final phase space coordinates of each particle was recorded as it crossed the plane of the mesh, which defined the beginning of the field free drift region of the time-of-flight.

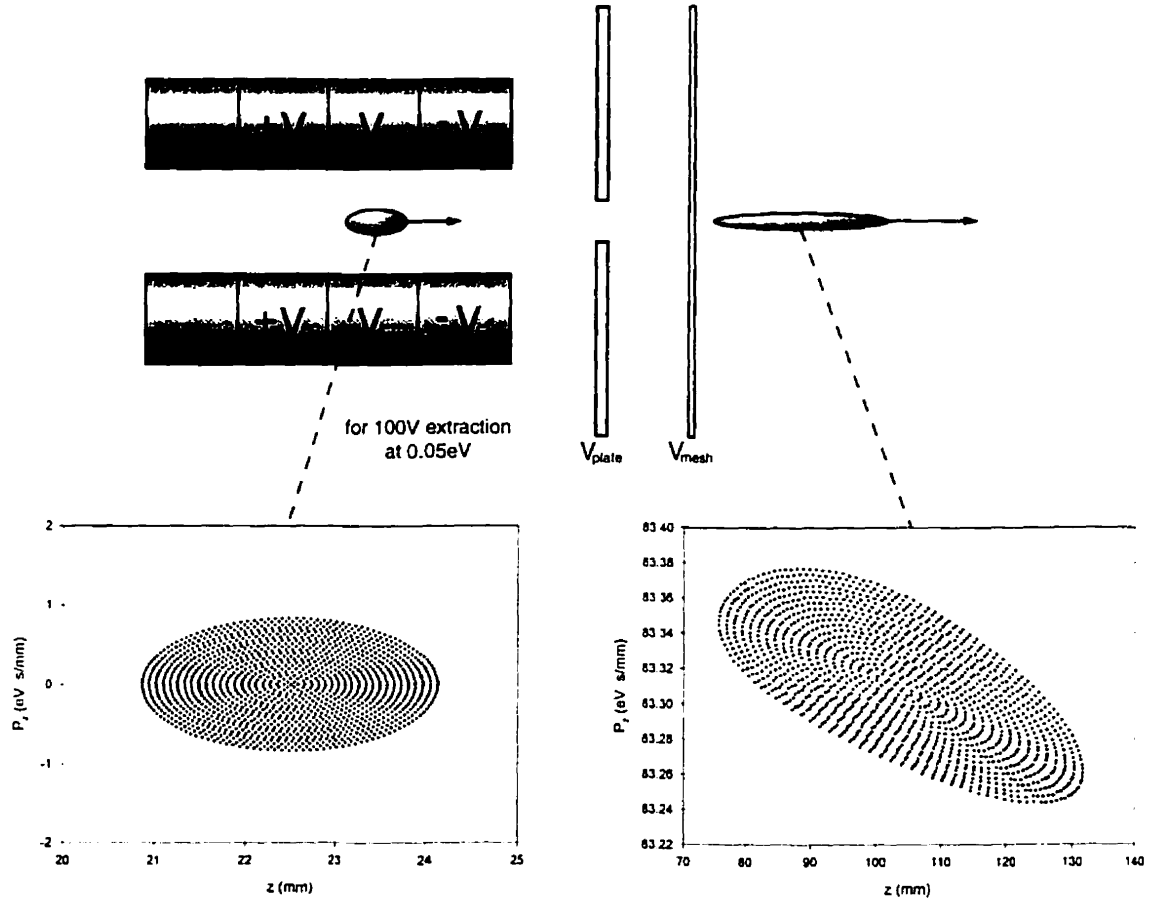

Fig. 4.4 SIMION extraction simulation of 1441 particles.

4.2.2 Full 3D Pulse Extraction: Radial Measurements

It was also necessary to study the radial behavior of the ion ensemble as it was extracted out of LTRAP and into the drift tube. In order to simulate that, a full 3D simulation had to be done. However, to use representative coordinates in this situation would prove difficult, since each pair of canonical coordinates used 1441 points, three dimensions would therefore involve 1441^3 points (approximately 3×10^9). A more practical approach was to generate 5000 points at random, using the probability functions for position and momentum (2.57) and (2.58). In a way similar to the one used in the previous section, a random sample of the ensemble was simulated through the extraction fields and their phase space coordinates recorded in the program, so that radial measurements could be made of the ion cloud inside the TOF system.

4.3 Time-of-flight Simulation

4.3.1 Drift Field Calculations: Building Time Histograms

Having used SIMION to obtain the phase space coordinates of the representative points of the ion ensemble at the entrance mesh, the next step was to project them forward in time to simulate their trajectories in the drift tube towards the detector. Two simplifying assumptions were made in this calculation, that the vacuum was good and so no ion-neutral collisions occurred during the flight and that there were no field imperfections in the drift region to disturb the ion motion.

The first assumption is valid since the mean free path at 2.5×10^{-6} Torr is much larger than the 1m flight tube. To illustrate this, consider the following definition for the mean free path λ [Hal88]

$$\lambda = \frac{1}{\sqrt{2}\pi N d^2} \tag{4.9}$$

where N is the number density of N_2 and d is the effective collision diameter. At STP, λ is typically 8.21×10^{-8} m [Han72]. Since λ is inversely proportional to N, it must also be inversely proportional to the pressure P. Therefore, within the TOF tube, the mean free path is nominally 25m, indicating that the chance of an ion-neutral collision is small. The overall effect is that the ion ensemble drifts through the TOF tube with negligible dispersion or retardation from the background gas.

The second assumption is also reasonable, but not as easy to justify. Theoretically, the flight tube must be field free because the entire tube was made of one solid piece, preventing any exterior fields from penetrating into the drift region. However, slight imperfections in the construction of the flight tube, detector, deflector plates or Einzel lens would contribute to field abnormalities and might possibly affect the ion trajectories. Unfortunately, these cannot be easily estimated and so the only possible solution was to adjust the simulation to fit the experimental data. This was done by leaving the simulation drift length variable, and allowing the computer to determine the effective drift length, to take into account any deviation in trajectory due to stray electric fields.

Evolving each representative particle's phase space coordinate forward in time involved the simple application of the kinematic formulae to each particle, as detailed in section 2.3.1. By fixing a distance D for the effective drift length, the simulation could calculate the total time-of-flight of each particle based on its original phase space coordinate.

In order for the computer program to create a simulated detector signal, it needed only to integrate the representative particles as they reached the plane of the detector, weighting each point with the appropriate weight factor. In so doing, the program essentially built up a histogram in time of all the particles as they arrived at the detector, much like what the experimental detector did when the real ion packet arrived. As was mentioned before, the distance of the detector in the simulation was left as a variable, so that any minor corrections to the path length of the ions could be accounted for in this way.

4.3.2 Temperature Fitting Routine

It was stressed many times already that all the simulations were dependent on one parameter, the temperature T of the ensemble of particles. In order to correctly model the experimental data, a proper value for T had to be chosen. This was accomplished by building up a library of data files containing the phase space coordinates of representative points at increasing temperatures, from k_bT=0.025eV to k_bT=0.075eV, in steps of 0.005eV. These files represented the trapped ion cloud in LTRAP prior to extraction into the drift tube, whose σ_z and σ_{p_z} values were determined by the parameters of the system (V_{RF}, V_{DC} and q) and the variable temperature T, according to the procedure in section 4.1.

Each of these files were then sent into SIMION as the starting point of the extraction phase and a new series of files were created to model the ion cloud at temperature T as it was extracted at each new extraction condition. Thus for every extraction condition, there was a library of files associated with it, representing the different temperatures of the ion cloud that was extracted.

Finally, a temperature fitting C++ program was written to take these new extraction files and evolve them forward in time to build up the histogram at the detector. The program would take each histogram and compare them with the experimental file that it was simulating and would first fit an effective drift length to match the two time-of-flight profiles. This was done using a bisection method for finding the minimum in the least-squares function between the experimental data and the simulated histogram, using a cubic spline interpolation [Pre95]. This fitting was done for each temperature and again the least-squares values were compared and the program selected the temperature file with the smallest deviation from experiment as the one with the best fit. A representative example of the result of such a fitting procedure is shown in Fig. 4.5.

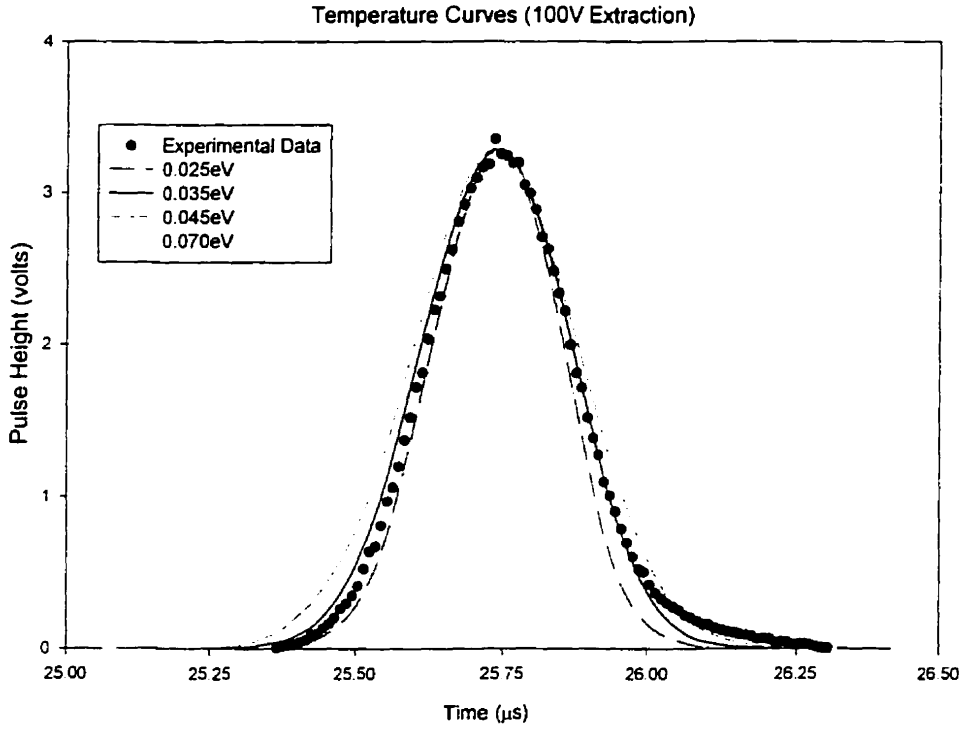

Fig. 4.5 Example of various temperature curves fitted to experimental data. The closest temperature curve was found to be $k_B T = 0.035$ eV.

Chapter 5 Results and Discussion

5.1 Experimental Results: Time-of-Flight Profile

Experimental results were based primarily on the time-of-flight spectrum of the ion cloud collected at the MCP detector. Typically, 1000 ion pulses were collected for each experimental reading, which the digital oscilloscope then averaged and recorded in the computer. Fig. 5.1 presents a typical time-of-flight spectrum of Cs^+ ions.

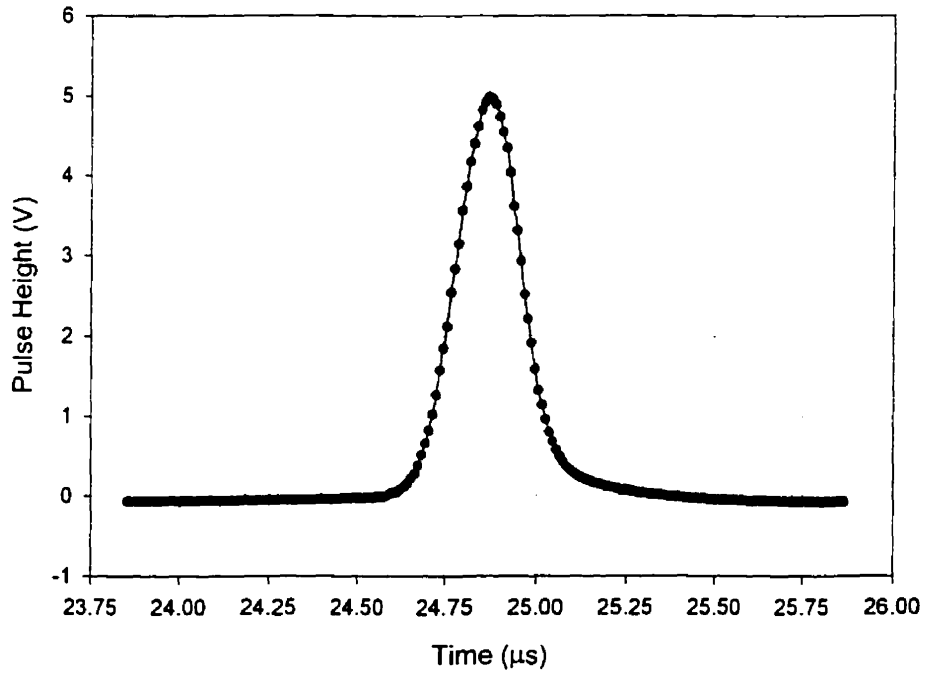

Fig. 5.1 Typical experimental TOF data recorded at the MCP detector.

Characteristically, the ion pulse was quite gaussian in shape, exhibiting only a slight asymmetry in the trailing edge of the pulse, corresponding to a small number of ions arriving slightly later than the ensemble. This was expected since the tail corresponds to ions that were delayed due to scattering by neutral atoms, dispersion due to flying through a mesh or other retarding mechanisms.

A typical pulse would include anywhere from 50 ions to 2500 ions, depending on the initial conditions and trap settings. Standard operating conditions are summarized in Table 5.1.

Operating Parameter	Default Values
LTRAP RF Voltage	200Vpp
LTRAP RF Frequency	800kHz
LTRAP Well Depth Bias Voltage	-10V
LTRAP Collection Time	50ms
LTRAP Extraction Voltage	200V across 30mm
LTRAP Buffer Gas Pressure	5×10^{-4} Torr
TOF Bias Voltage	-2.5kV
TOF Pressure	2.5×10^{-6} Torr

Table 5.1 Default values for the operating parameters of LTRAP.

5.2 Trapping and Extracting Ions in LTRAP

Several parameters were involved in achieving trapping conditions in the system, including q value, buffer gas pressure, axial well depth, initial ion beam current and collection time. Ion extraction also involved its own set of parameters; primary extraction voltage, secondary extraction voltage and time-of-flight bias voltage. Each of these parameters were studied to see which ones affected the spectrum and under what conditions they were important.

5.2.1 General Trapping Conditions

The initial trapping conditions of the system were carefully studied in order to gain a fuller understanding of the phase space dynamics inside LTRAP. Each relevant parameter and the effect that it had on the system has been presented here in order to better comprehend not only the physics involved in this trap, but to gain experience as to what makes a better trap.

Collection Time

One important characteristic of LTRAP was the ability to collect a significant amount of ions and cool them in a reasonable amount of time. By varying the collection time, it was possible to probe the loading characteristics of the trap and understand how different parameters affected the filling process (Fig. 5.2). Fig. 5.3 shows the relative number of ions in a pulse as a function of the loading time for various q values in the trap. The well depth was set to –10V and the extraction voltage was 200V, while the incoming ion beam was kept constant. As can be seen in the graph, the curves indicate that there is trap saturation after approximately 50 – 100 ms of collection time. Also, the dependence on q value indicated that the trap volume was changing with varying RF voltage, which was predicted by the pseudopotential well model. The lower the q value, the lower the RF confinement and then consequently, the larger the radial extent of the ion cloud, effectively reducing the number of ions near axis that would be successfully transmitted to the detector.

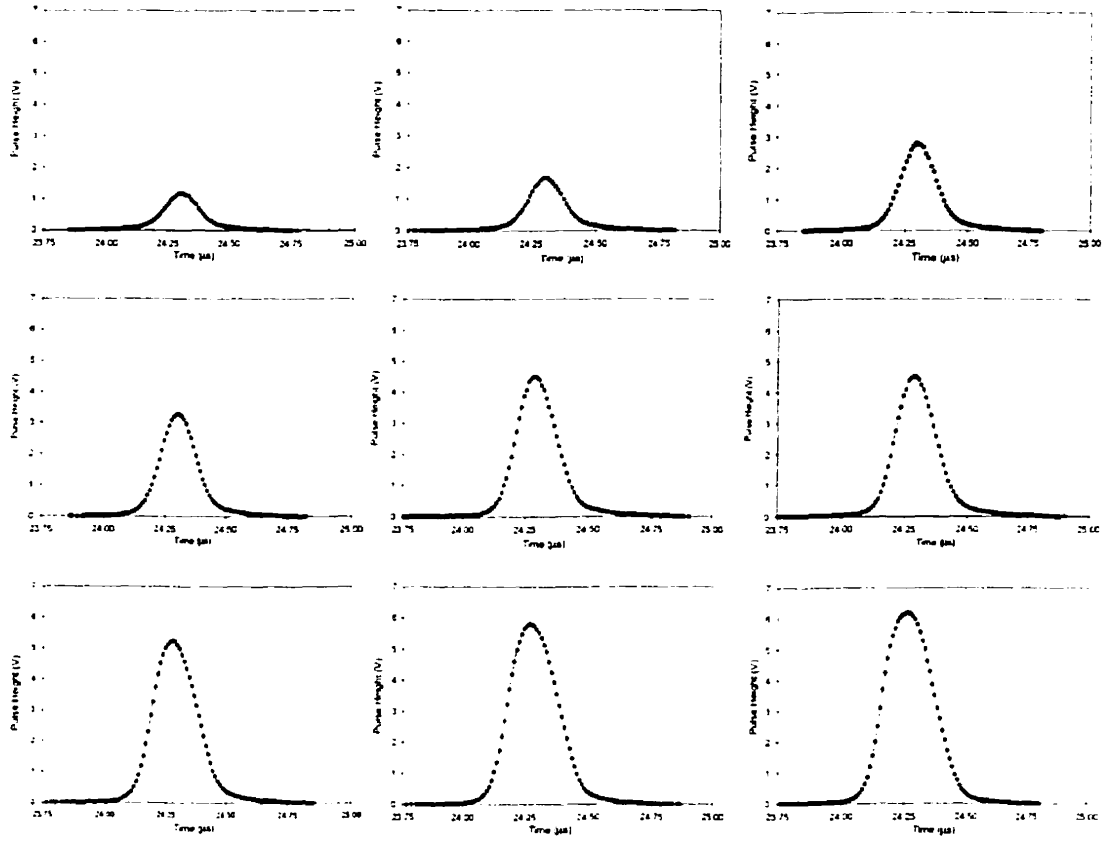

Fig. 5.2 A series of TOF peaks as a function of collection time. This was extracted with $200V_{ext}$ from an initial trap setting of q=0.6 and a well depth of 10V.

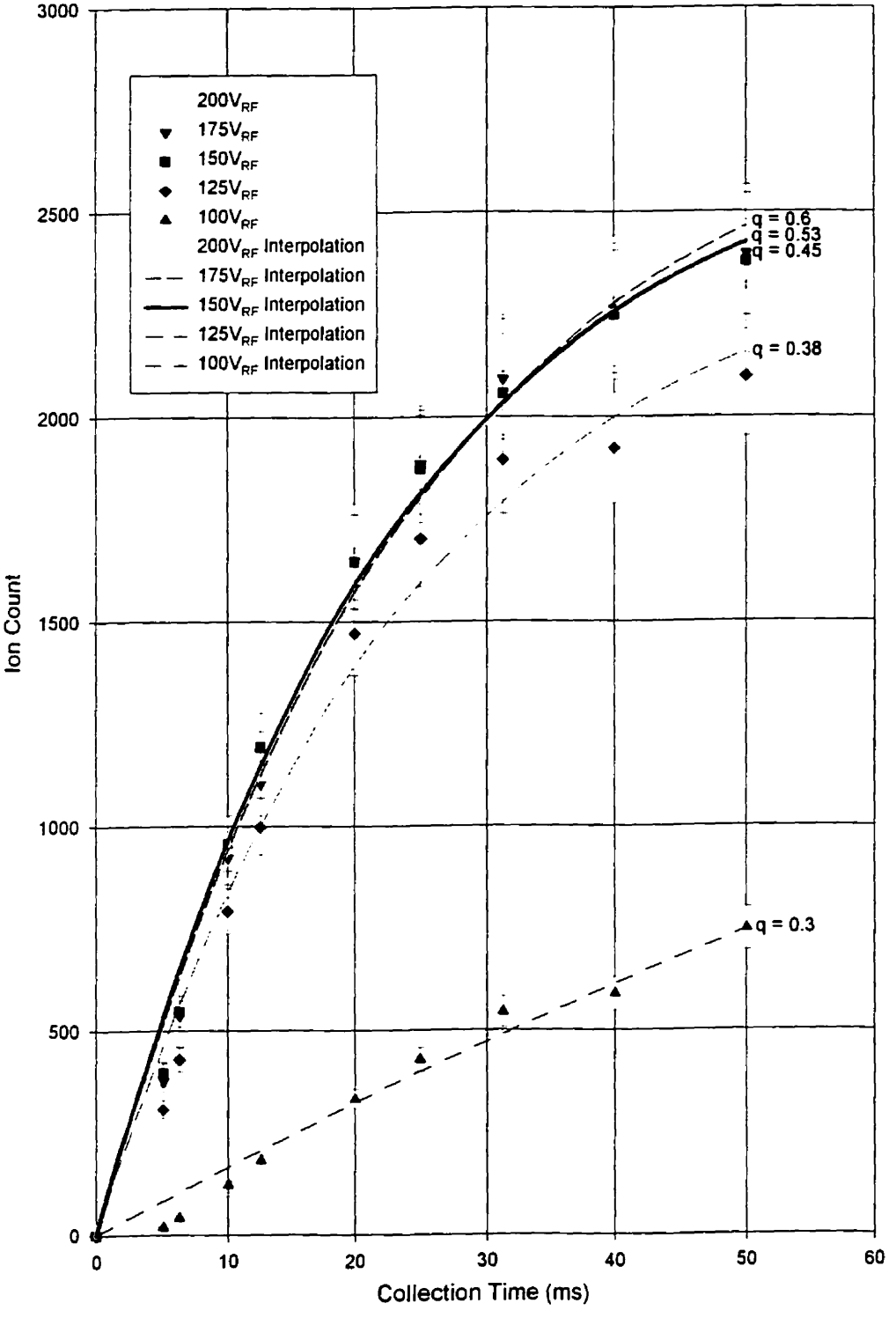

Fig. 5.3 Number of detected ions versus Collection Time. The experiment was carried out for various RF voltages on the LTRAP rods. The interpolation lines are polynomial fits to the experimental data points.

Well Depth

The second major parameter involved in the proper operation of the LTRAP system was the DC bias voltage on the trapping rod segments, which set the axial well depth of the trap. This DC bias was varied from –2V to –35V in order to carefully explore the parameter space and find the optimum trapping well depth. Since the axial well depth affected the radial confinement, it was expected that the signal response would be different at different q values, corresponding to different radial pseudopotentials. Therefore, two q values, 0.24 and 0.6, were used in this study. Fig. 5.4 shows a graph of the total number of captured ions detected as a function of the well depth for these two q values.

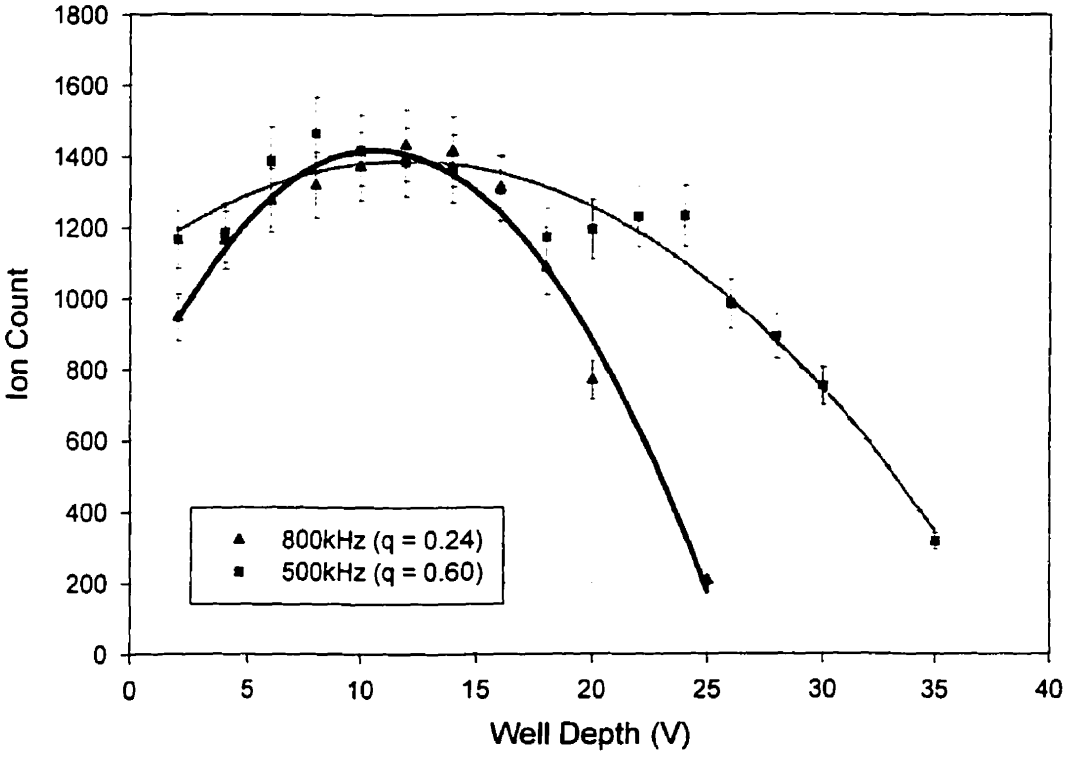

Fig. 5.4 Number of detected ions versus well depth voltage. All experimental data was taken with $V_{RF} = 200\mathrm{V_{pp}}$. The trendlines were generated using a polynomial fit to the data points.

One of the key features to note in this figure is the range of well depths at which effective ion trapping occurs. Below 5V well depth, it can be seen that the ion count decreased. No doubt this was because of the relative weakness of the axial trap in capturing and confining the ions from the incoming DC beam. Above 15V well depth, it can be seen that the ion count again decreased, even though the axial potential well was increasing. This is no doubt due to the effect of the axial potential well on the radial confinement where the strong axial confining field causes a defocusing force in the radial direction. This force is normally counteracted by the RF confinement of the quadrupole rods, but as the well increased in depth, so did this radial defocusing, until the RF confinement was no longer sufficient to hold the ions trapped in space.

It is interesting to note that for the case of $q = 0.24$ the radial deconfinement potential from the axial well at $10\,V_{DC}$ is exactly half the depth of the radial pseudopotential from the RF field. At $20\,V_{DC}$ the axial potential well fully destroys the radial confinement on the axis and so the only ions that are collected must be off axis where the axial confining field decreases. At $q = 0.6$ the corresponding values of V_{DC} would be raised by a factor of about 2.5.

It therefore appears that, at least for a linear RFQ trap of the LTRAP configuration, the optimum axial well depth is about that which takes away half the depth of the pseudopotential well of the RF quadrupole field.

Trap Saturation

An interesting but completely unpredicted phenomenon occurred when testing the trap saturation properties of LTRAP by changing well depth. There was evidence of a secondary potential trap just exterior to that created by LTRAP. While its location could not be accurately pinned down from the time-of-flight observations, it was estimated that this trap was situated somewhere in the region between the last rod segment and the pulsing plate. Referred to as a parasitic trap, this trap would exhibit itself when the primary trap was saturated and ions started spilling into this new trap. The phenomenon was completely reproducible and the parasitic trap volume was surprisingly comparable to the actual trap.

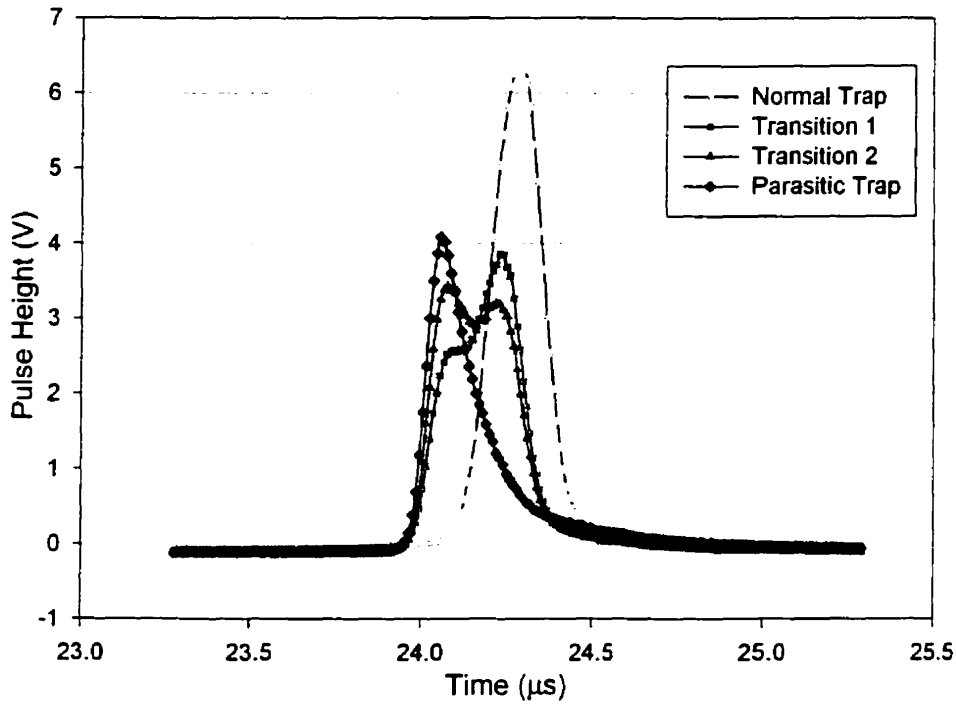

Fig. 5.5 A graph showing the transition between ions occupying the normal LTRAP region and ions falling into the "parasitic" trap region. The axial well depth was set to –1.5V and the transition was created by increasing the DC bias voltage on the final trap segment.

Others have also reported this surprising result [Str55], and the effect has even been photographed by Whetten in his experiments with iron filings in a Paul trap. He described this trapping phenomenon as occurring in "strange locations where there is an inhomogeneous ac field... " [Whe74]. This would agree with the observation that the trap is somewhere within the fringing field region of the quadrupole rods. As fascinating as it was to observe this effect, it was something to be avoided in the proper functioning of the LTRAP system and it set a definite limit on the number of ions the trap could be asked to collect (i.e. of the order of several thousand).

Ion Extraction

As pointed out many times already, the effect of different extraction conditions was critical to the experiment in this thesis. This effect is shown in Fig. 5.6 and the numbers associated with these graphs are given in Table 5.2.

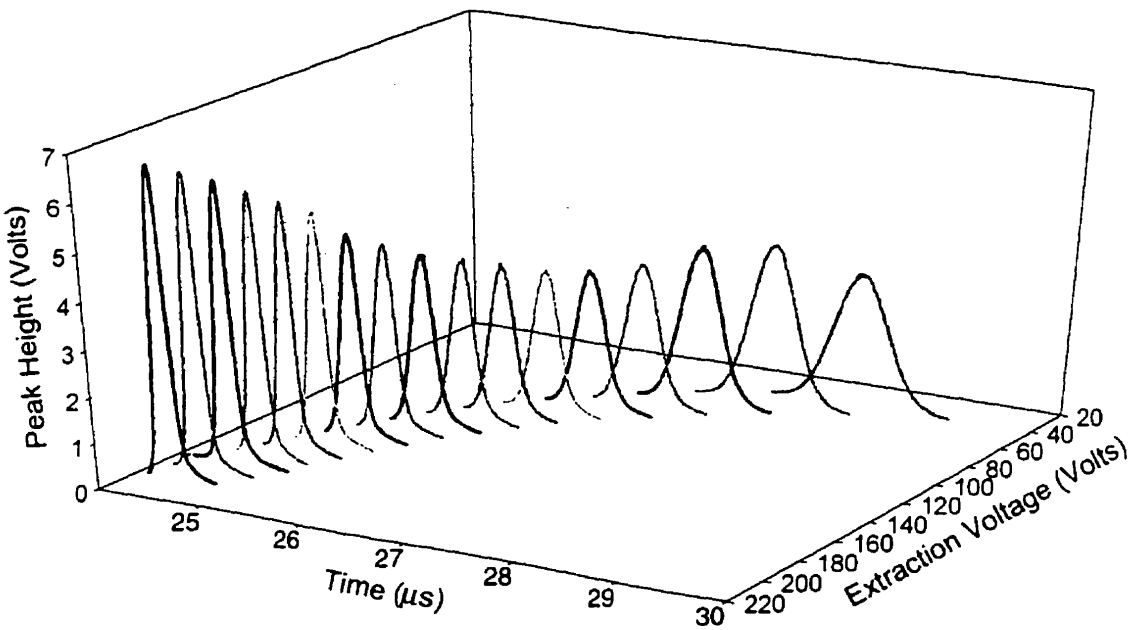

Fig. 5.6 Waterfall plot of TOF spectra as a function of extraction voltages.

Extraction Voltage (V)	T_{peak} (μs)	V_{peak} (V)	Resolution (m/Δm)	Temperature ($[k_B T]$ = eV)	Sim. Detector Distance (mm)
40	28.275	2.95	23.6	0.030	1292.414
50	27.595	3.54	27.6	0.030	1288.466
60	27.075	3.54	31.5	0.030	1285.437
70	26.665	3.17	35.1	0.035	1284.536
80	26.295	3.10	37.6	0.035	1282.039
90	26.005	3.16	41.9	0.035	1279.804
100	25.735	3.41	46.0	0.035	1277.871
110	25.545	3.62	49.1	0.035	1276.825
120	25.325	3.80	52.8	0.035	1275.737
130	25.165	4.14	54.7	0.035	1274.734
140	25.005	4.50	59.5	0.035	1273.199
150	24.865	5.05	62.2	0.035	1273.930
160	24.745	5.41	65.1	0.035	1272.680
170	24.615	5.72	64.8	0.035	1271.762
180	24.515	6.05	72.1	0.035	1271.148
190	24.415	6.36	71.8	0.035	1270.543
200	24.315	6.68	71.5	0.040	1269.721
				T_{ave} = 0.0344	D_{ave} = 1277.697
				σ_T = 0.0024	σ_D = 6.75
				$\%_{error}$ = 7.0%	$\%_{error}$ = 0.53%

Table 5.2 Extraction Data Table. The first four columns summarize the data in Fig. 5.6. The last two columns show the simulation parameters used to obtain the best fit to the data. The results underneath show the averaged values for these parameters as well as their errors.

It should be noted that the quoted extraction voltages refer to the applied voltages at the end rod segments of the LTRAP system. Therefore, the extraction voltage is really the potential difference between the segments that were pulsed high and pulsed low during the extraction phase of the LTRAP cycle. Since the segments were 15mm long, the extraction field was really $V_{ext}/30\text{mm}$.

As can be seen in Fig. 5.6, varying the primary extraction voltage caused the time-of-flight spectrum to change markedly. Primarily, increasing the extraction voltage caused a shift in the time of arrival of the cloud, about 4μs between a 40V extraction and a 200V extraction. The 200V extraction was deemed to be a safe upper limit for the extraction electronics.

It is perhaps interesting to note that the simulations showed that the ion ensemble spent approximately 4 to 8 μs in the overall extraction region before entering the time-of-flight drift region. This ranged from a sixth to a quarter of the overall flight time. Thus in a working mass spectrometer the time taken for extraction from a linear RFQ trap would itself play a significant part in the mass resolution.

Also, it should be noted that the mass resolution ($m/\Delta m$) of the system, here determined as simply half the time resolution, improved by nearly a factor of 3 by increasing the extraction voltage from 40V to 00V (Fig. 5.7).

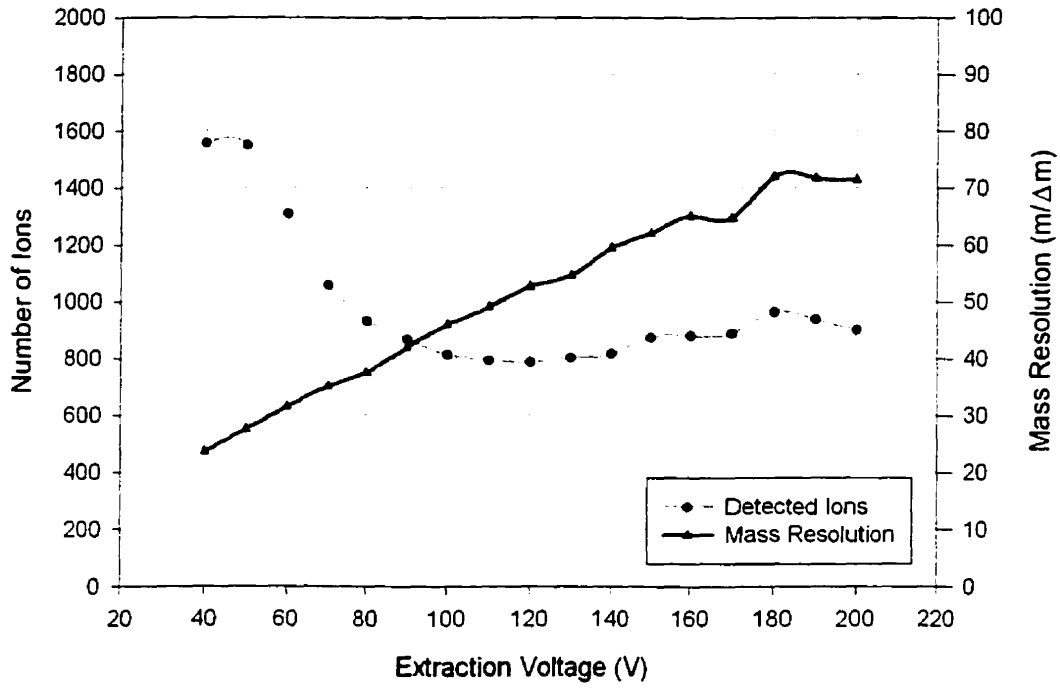

Fig. 5.7 Plot of sensitivity (*left scale*) and resolution (*right scale*) versus extraction voltage. One will always be optimized at the expense of the other in a mass spectrometer.

Finally, the computer simulation showed an impressive agreement for the value of the temperature of the initial ion cloud, based on the least-squares fit with the experimental peaks. The temperature was very near 0.035eV for all the extraction potentials. Also, the drift length of 1.278m, which was left as an adjustable parameter in the computer simulation, was in pretty close agreement for all the different extractions.

5.2.2 Overall LTRAP Efficiency

DC current transmission through various parts of the system was estimated by grounding electrodes through a picoammeter. At normal current settings for the ion gun (65A at 40W), it was determined that the total current entering into the cooling quadrupoles was approximately 23-24pA. Of this current, a maximum of 16pA passed through the miniature quadrupole and entered into LTRAP. This was at a maximum radial confinement setting of $280V_{RF}$ and 0.04 Torr in the cooling rods.

However, this current was far too much for LTRAP to handle and to avoid trap saturation it had to be reduced to about 0.3-0.4pA. This was accomplished by reducing the RF amplitude on the cooling rods to $155V_{RF}$.

From / To	Total Charge	% Transmission
Ion Gun to Cooling RFQ	23 pA	N/A
Cooling RFQ to LTRAP	16 pA maximum 0.3 pA nominal	70% maximum 1.3% nominal
LTRAP*	9 375 ions	N/A
LTRAP to Detector*	2 500 ions at detector	26.7% transmission

*Tabulated values are for a collection time of 50ms and 200V extraction conditions.

Table 5.3 Table of LTRAP transmission efficiency data.

It is seen that, without any optimization for efficiency, the LTRAP system reached a collection efficiency of close to 30% for any ion beam delivered to it. Since the cooling RFQ can reach an efficiency of about 70% the overall trapping efficiency of an ion beam entering the cooling system can be about 20%. This, of course, applies only to beams that do not overload the trap, i.e. beams of 0.3pA or less.

5.2.3 Time-of-Flight Performance

The time-of-flight performance was determined by three basic elements, the drift tube bias voltage V_{DC}, the deflector plates and the Einzel lens system. Each one was investigated experimentally in order to determine the best overall conditions for the optimum detection of ions.

Time-of-flight Bias

Adjusting the time-of-flight bias voltage was the primary way of controlling the final kinetic energy of the ion packet after the secondary extraction region in the flight tube. By adjusting the kinetic energy, the time-of-flight spectrum was altered, as shown in Fig. 5.8.

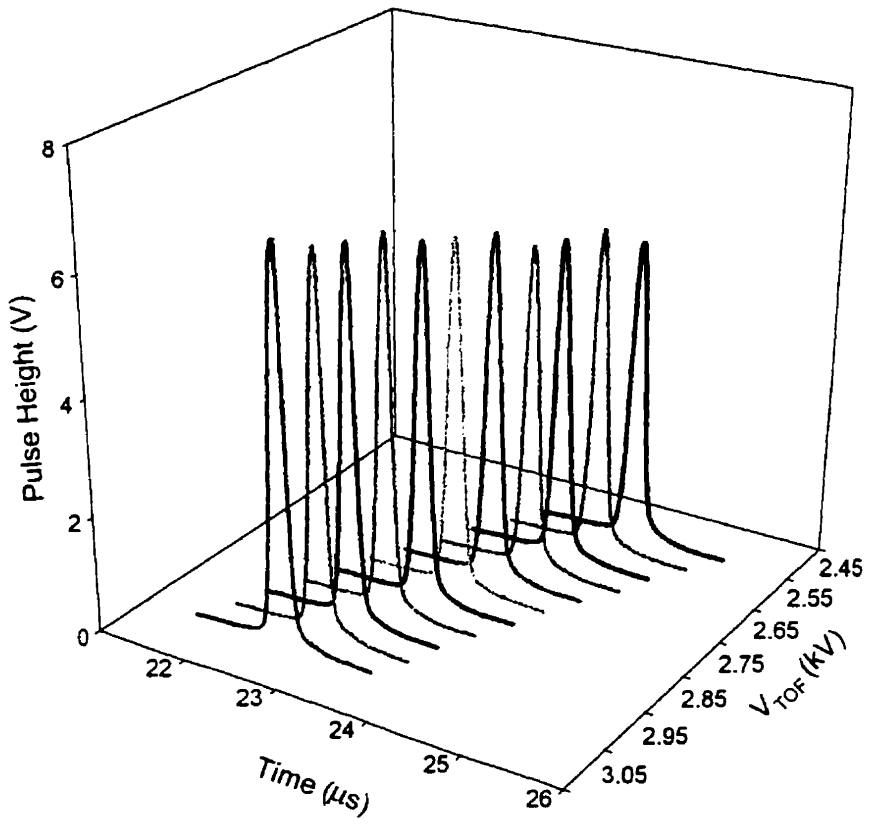

Fig. 5.8 Waterfall plot of TOF spectra as a function Time-of-Flight Bias Voltage.

As was expected, the ion pulses arrived earlier and earlier in time as the TOF bias voltage was increased from –2.5kV to –3.0kV. In addition, the deflector plates and the einzel lens systems were adjusted to optimize the signal detection for each bias voltage setting, while keeping all the trapping conditions constant during the experiment. Table 5.4 summarizes the data collected from the experiment.

V_{TOF} (Volt)	T_{peak} (μs)	V_{peak} (Volt)	Ion Count	Mass Resolution ($m/\Delta m$)
-2500	24.325	5.302	1725	67.57
-2550	24.105	5.632	1861	66.96
-2600	23.885	5.580	1847	65.98
-2650	23.755	5.637	1819	65.43
-2700	23.555	5.972	1947	64.85
-2750	23.345	6.049	1989	64.84
-2800	23.235	6.142	2007	64.54
-2850	23.035	6.416	2097	60.62
-2900	22.855	6.381	2112	60.15
-2950	22.745	6.464	2107	63.18
-3000	22.575	6.702	2247	62.71

Table 5.4 V_{TOF} Data Table. The table represents the data shown in Fig. 5.8.

It can be seen that there was a slight but noticeable decrease in mass resolution as the bias voltage increased. This could possibly be due to the spread in kinetic energy introduced in the acceleration region after extraction. In any case, the effect is of little interest in the present work since the goal was to achieve significant changes in the TOF signal under different operating conditions so as to discern the ion density distribution in the trap. Since the effect was small, it could not be used for this purpose.

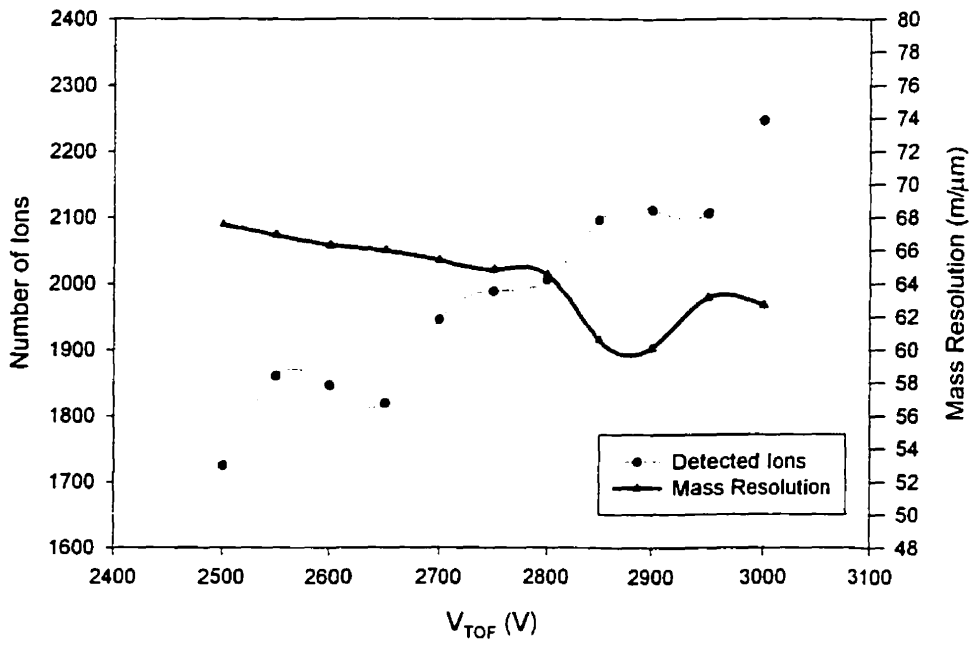

Fig. 5.9 Plot of sensitivity (*left scale*) and mass resolution (*right scale*) versus the TOF bias voltage.

Deflector Plates

The deflector plate system was used primarily to steer the ion pulse onto the detector surface for optimum signal strength. This was necessary because it is generally impossible to perfectly align an ion drift system. However, the system could also be used to obtain an estimate for the radial extent of the ion collection at the detector. This was obtained by deliberately steering the ion collection off the detector path and noting the decrease in ion count for various deflection angles.

The first step was to create a calibration curve of deflection voltage and distance of deflection at the detector. This was accomplished by simply running the computer simulation for various deflection voltages for a parallel beam of ions and seeing the deflection distance at the detector (Fig. 5.10).

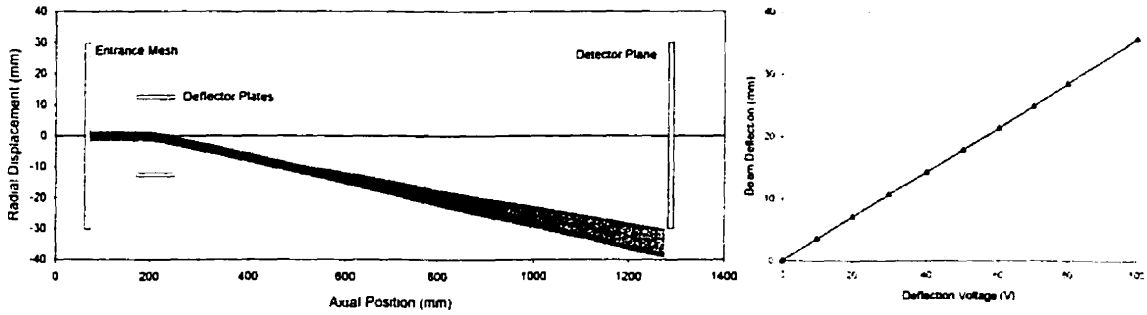

Fig. 5.10 Computer simulated deflection of a parallel ion beam (*left*). The transverse deflection was used to create a calibration curve for the deflector plates (*right*).

Experimentally, the deflection voltage was increased in 5V intervals from –110V to 110V, which corresponded to a deflection of –40mm to 40mm at the detector plane. The total ion count was recorded and the data was then normalized to the highest ion count to obtain the graph in Fig. 5.11.

This figure also shows the data taken from a full 3D simulation of 5000 ions under the same conditions as in the experiment, with a temperature of 0.035eV. It shows the correspondence between the predicted curve and the actual experimental curve. The total radial extent of the ion pulse was estimated to be approximately 120mm, with nearly one-fifth of the ions falling on to the detector surface (25mm diameter). This fraction of detectable ions could be further increased with the addition of an Einzel lens or another such beam focusing system. In this way, the radial extent of the beam was manipulated and the signal strength was greatly improved.

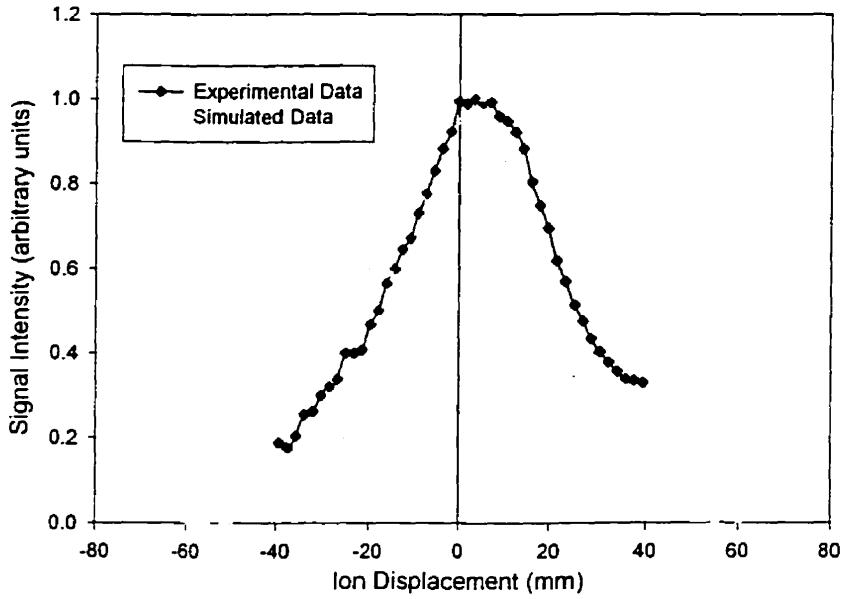

Fig. 5.11 Calibrated graph showing signal intensity versus deflection. The experimental data (◆) shows that the actual system is biased a little to the +x direction in this graph. The simulated data ( ) shows that the predicted radial extent of the pulse is ±60mm.

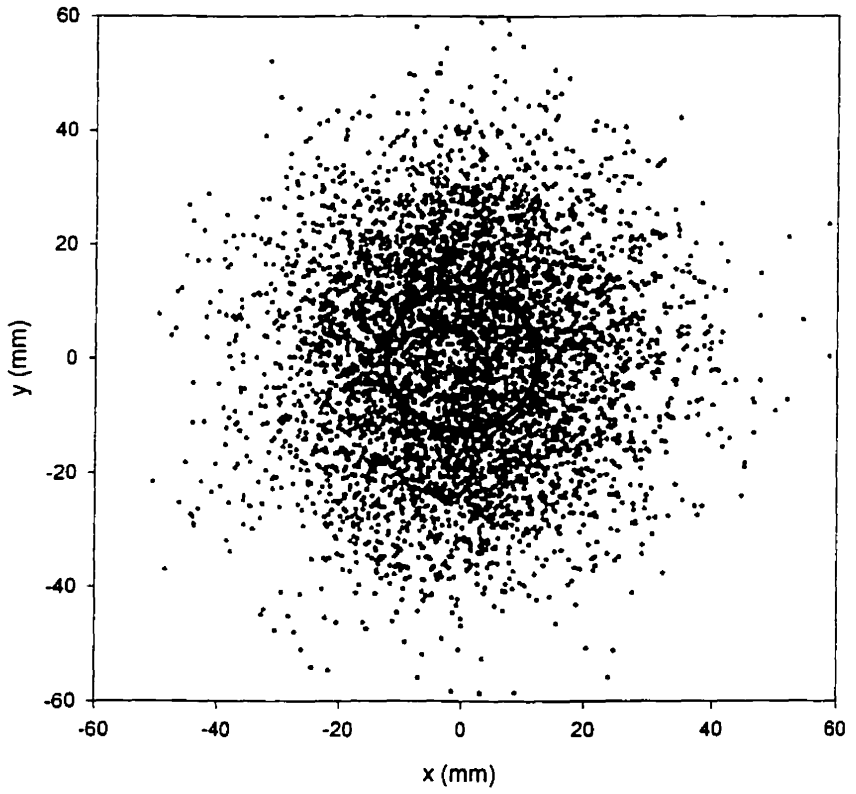

Fig. 5.12 Distribution of ions at the plane of the detector. This simulation data was taken from 5000 randomly generated ions that were pulsed to the detector, showing the radial distribution of ions. Roughly 1/5 of the ions are within the detector surface (*outlined in black*).

Einzel Lens

The Einzel lens was a later addition to the time-of-flight system and was placed there to assist in focusing more of the ion pulse onto the detector surface, thereby increasing the overall sensitivity of the mass spectrometer (Fig. 5.13). It was determined experimentally that the optimum voltage for the lens was to bias it +1675V above the TOF potential.

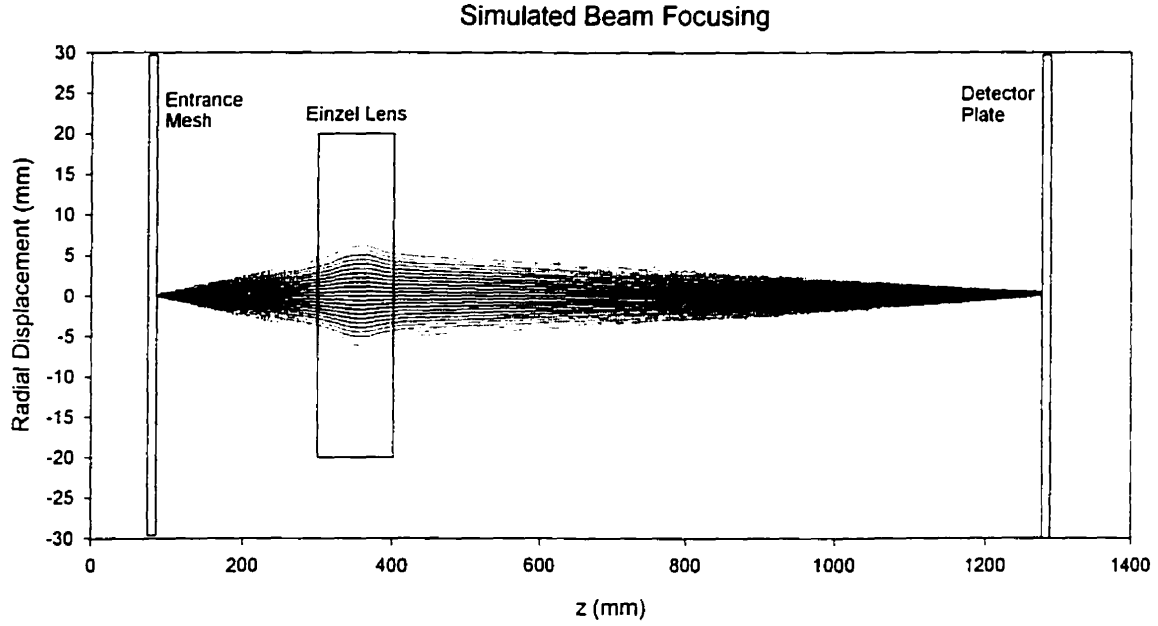

Fig. 5.13 Simulated ion trajectories being focused by the Einzel lens system. Note that the *y*-axis scale has been exaggerated, the actual beam divergence at the entrance mesh is about a 3° cone.

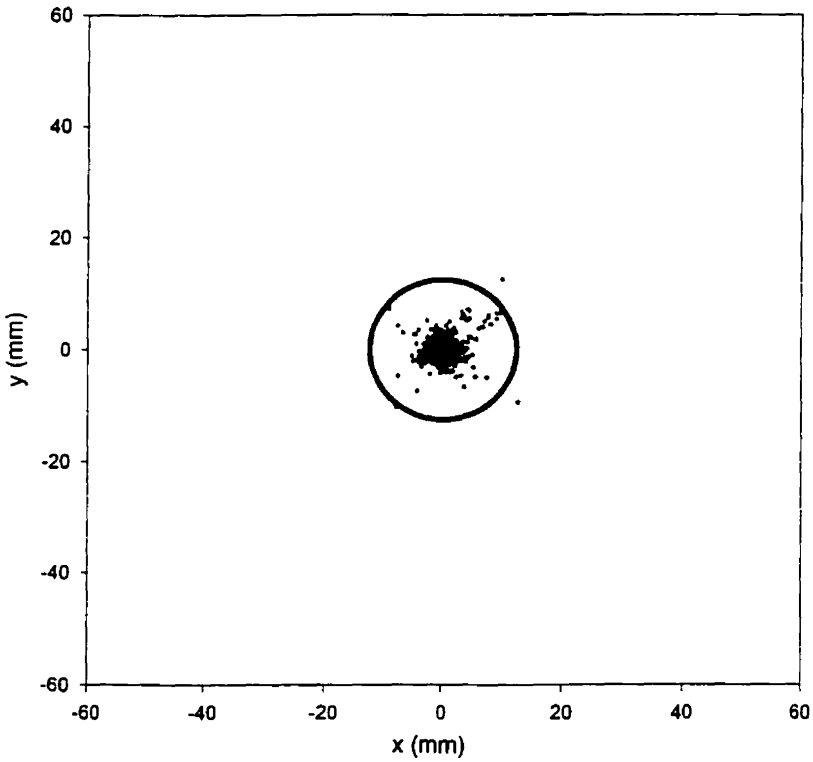

Fig. 5.14 Distribution of 5000 simulated ions at the plane of the detector after being focused by the Einzel lens. The black circle represents the effective detector surface area.

Thus, with the addition of the lens, it was possible to focus nearly all the ions back onto the detector. This was demonstrated through the simulation of 5000 random particles in the program (Fig. 5.14). Experimentally, there was no way of confirming the fraction of ions trapped that were detected by the MCP since there was no ion detection system near the vicinity of LTRAP rod segments. The only thing that could be done was to empirically determine the lens setting that resulted in the highest overall signal at the detector.

5.3 Simulation Results

5.3.1 Temperatures Measurements

The temperature measurement algorithm used in all the experiments involving temperature was the one outlined in section 4.3.2. Because of the labor intensive process of creating a library of files for ion extraction at various extraction voltages and temperatures, only certain experiments could be analyzed this way, since changing any other parameter would require the time consuming process of creating a separate library. Therefore, the temperature fitting program was used only to determine the temperature for all experiments performed with a -10V well depth and a –2.5kV TOF bias voltage.

Temperature at various extraction voltages

The purpose of the first series of experiments to be carried out was mainly to test the temperature fitting algorithm. Because all the TOF signals came from the same initial ion distribution in the LTRAP system, all the signals should be fitted by the same temperature. Fig. 5.15 summarizes the results of this experiment.

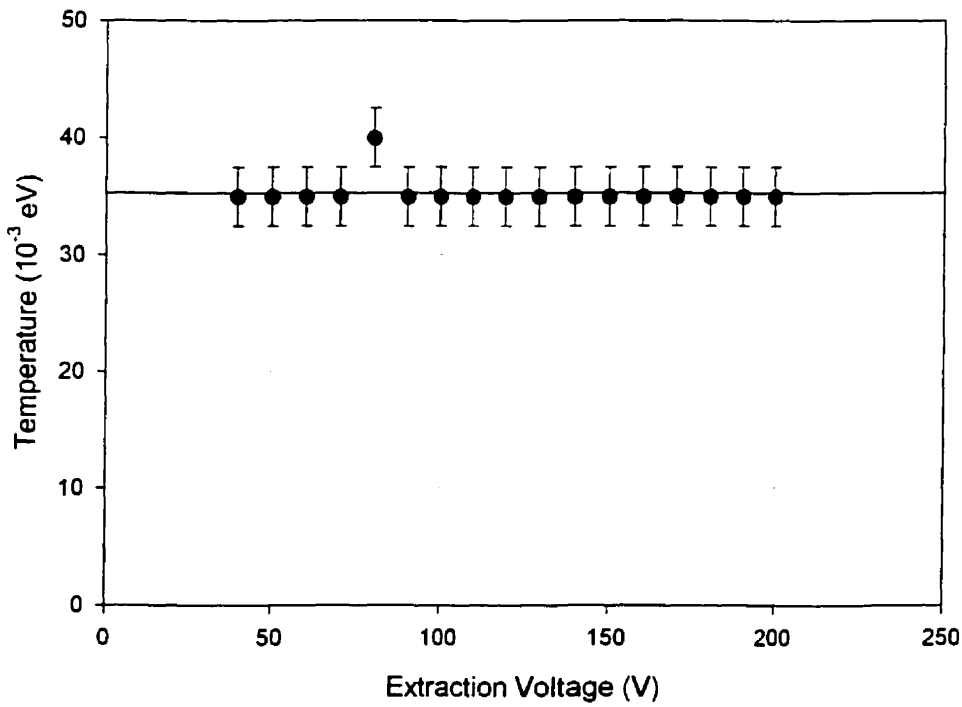

Fig. 5.15 Graph of initial ion temperature in LTRAP as a function of the applied extraction voltage.

All the data points were taken from the same initial LTRAP conditions: $200V_{pp}$ at 800kHz RF, 5×10^{-4} Torr N_2 pressure, -10V well depth bias and –2.5kV TOF bias. As can be seen, all the measurements but one fell into the same temperature bin $k_BT = 0.035\text{eV}$. This was an encouraging result for two reasons; it was evidence that the temperature fitting program was indeed performing properly and the actual value of the temperature was very close to room temperature (0.025eV). This result is in agreement with other studies on ion temperature in traps that were also performed at McGill: 0.042eV by Kim [Kim97], 0.043eV by Ghalambor-Dezfuli [Gha96] and 0.05eV by Lunney [Lun92].

Temperatures at various cooling times

In order to see the time necessary for the ion beam to cool into a thermalized cloud, the collection time was progressively shortened until the ion pulse did not have enough time to cool and the temperature exceeded the 0.075eV limit of the temperature fitting program. The results presented here were taken with a buffer gas pressure of $1.00 \pm 0.25 \times 10^{-4}$ Torr, slightly lower than normal, so that the cooling time was sufficiently lengthened for the cooling process to be observed. Fig. 5.16 shows the results.

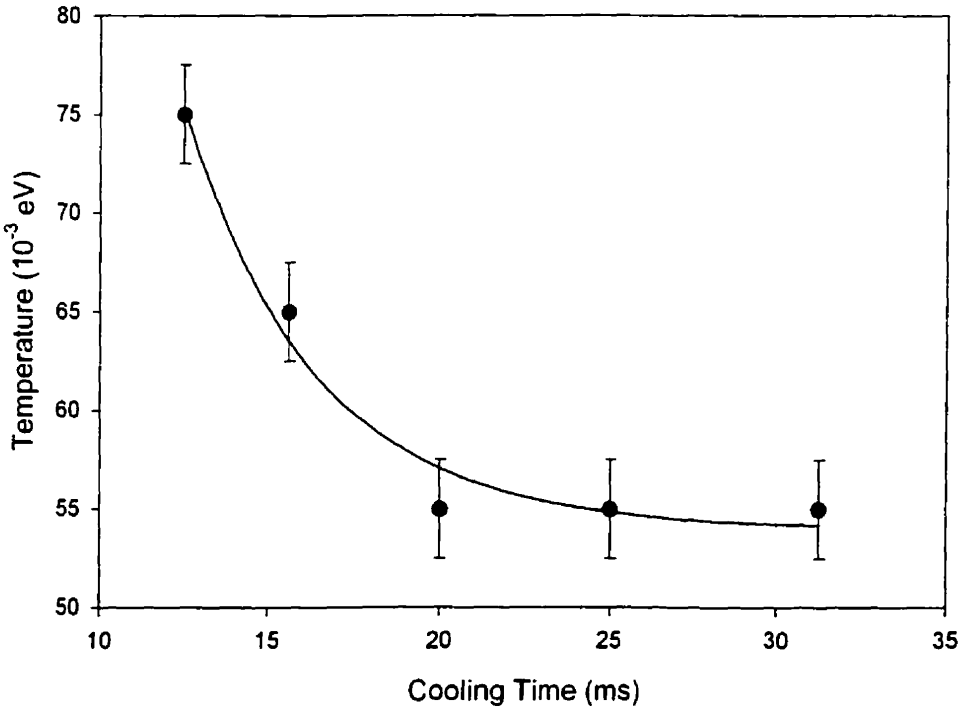

Fig. 5.16 Graph of initial ion temperature as a function of collection time. The curve is an exponential fit to the data points.

The shortest interval (12.5ms) shows a value for k_BT of 0.075eV, which was the limit of the fitting program. The graph also shows an exponentially decaying temperature as a function of collection time, which was indicative of the cooling process within the LTRAP system. From the exponential fit, a decay time constant $\tau_{cool} = 3.87\text{ms}$ was obtained.

It can be seen that in this experiment the temperature did not reach the value of 0.035eV of the other experiments. This is because of the low gas pressure that was used to extend the cooling time (see Fig. 5.17)

To see if this time constant τ_{cool} was reasonable, it was compared to the theoretical mean collision time for N_2 gas at 10^{-4} Torr. At this pressure, the calculated mean free path is $\lambda = 625\text{mm}$. The mean collision time can be defined simply as:

$$\lambda = \tau\tilde{v} \tag{5.1}$$

where $\tilde{v}$ is the most probable value for the velocity of the ion. $\tilde{v}$ can also be estimated by:

$$\tilde{v} = \sqrt{\frac{2k_BT}{m}} \tag{5.2}$$

which comes from the equipartition theory of energy. For a gas pressure of 10^{-4} Torr, this yields a collision time constant $\tau_{collision} = 3.23\text{ms}$.

By comparing the values for the two decay time constants, it can be seen that the cooling process would appear to be occurring on the same time scale as the ion-neutral collisions. This would therefore suggest that the ion cooling in this system was dominated by a small number of collisions, which was a result also reported by Kim [Kim97].

It is perhaps interesting to note that the ion mobility model can also give an estimate to the cooling time constant by extrapolating the mobility to the pressure region of interest. The energy decay constant as determined from mobility can be shown to be:

$$\tau_E = \frac{mK}{2e} \tag{5.3}$$

where K is the mobility constant, which relates the ion drift velocity to the electric field strength.

$$\mathbf{v} = K\mathbf{E} \tag{5.4}$$

K can be deduced from the reduced mobility K_o by the following:

$$K = K_o \cdot \frac{760}{P} \cdot \frac{T}{273.15} \tag{5.5}$$

K_o is a tabulated value that can be found in the tables of ion mobilities [Ell78]. For Cs^+ in N_2, the reduced mobility is 2.21 cm^2/Vs. At 10^{-4} Torr and at T = 300K, K would be 1.84×10^7 cm^2/Vs. This would give a value for $\tau_E = 1.25ms$.

It can be concluded from this result that the mobility model of a viscous drag force on the ions is not as applicable in the pressure regime under which these ion-cooling experiments were being carried out. This is because an ion undergoes less than one collision with a gas molecule in one decay time constant deduced from mobility.

Temperatures at various LTRAP pressures

Another interesting series of experiments involving temperature measurements was the one that determined the minimum pressure required for efficient trapping of ions in the system. By varying the pressure in the LTRAP region, it was possible to record the pressure just at the onset of ion cooling and note the rate of cooling as the pressure increased. However, there is a significant uncertainty in the pressure measurement simply because it was very difficult to control the buffer gas inlet valve reliably at such low pressures. The results are shown in Fig. 5.17.

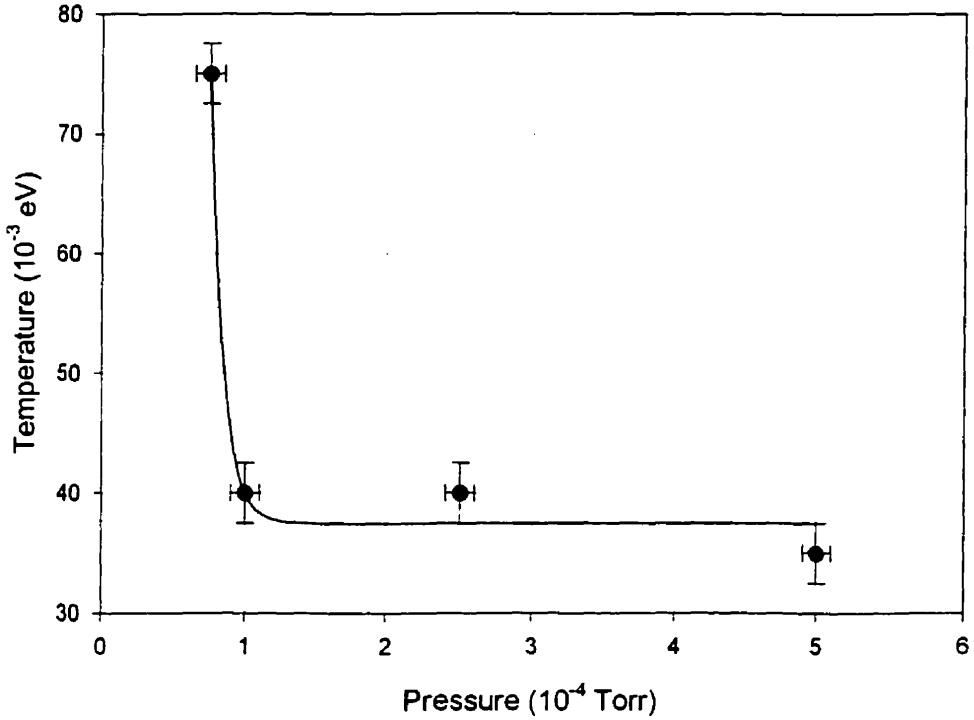

Fig. 5.17 Graph of the initial ion temperature as a function of the buffer gas pressure in the LTRAP region. The curve is an exponential fit to the data points.

It is difficult to understand what mechanisms are involved in the onset of buffer gas cooling, but it was obvious that in this system, the RF heating was greater than the collisional cooling at pressures lower than 10^{-4} Torr. Since both systems rely on the actual ion-neutral collision, it becomes a very complex problem to determine the relationship between heating and cooling as a function of pressure. Nevertheless, it is possible that at low pressures, the RF heating was less affected by the decreased number of neutral gas particles than the collisional cooling process, suggesting that the heating mechanism requires fewer collisions to effectively transfer heat into the system.

5.3.2 Phase Space Reconstruction

In an attempt to create an actual phase space reconstruction using the Fourier Slice theorem, a program was made to take the experimental Time-of-Flight pulse data and extrapolate them back into the LTRAP region, essentially recreating a projection of the phase space distribution of the initial ion ensemble.

Again, some simplifying assumptions had to be made in setting the parameters of the computer program, such as actual flight length, in order to obtain the phase space projections from the experimental data. Essentially, the complete $z - p_z$ phase space plane of the LTRAP system was mapped out, with limits $-22.5\text{mm} \le z \le 22.5\text{mm}$, where $z = 0$ is the trap center, and $-2\,\text{eV}\cdot\mu\text{s/mm} \le p_z \le 2\,\text{eV}\cdot\mu\text{s/mm}$. Fig. 5.18 shows the reconstructed phase space projection taken from the same experimental data as in Fig. 5.6 at 120V extraction.

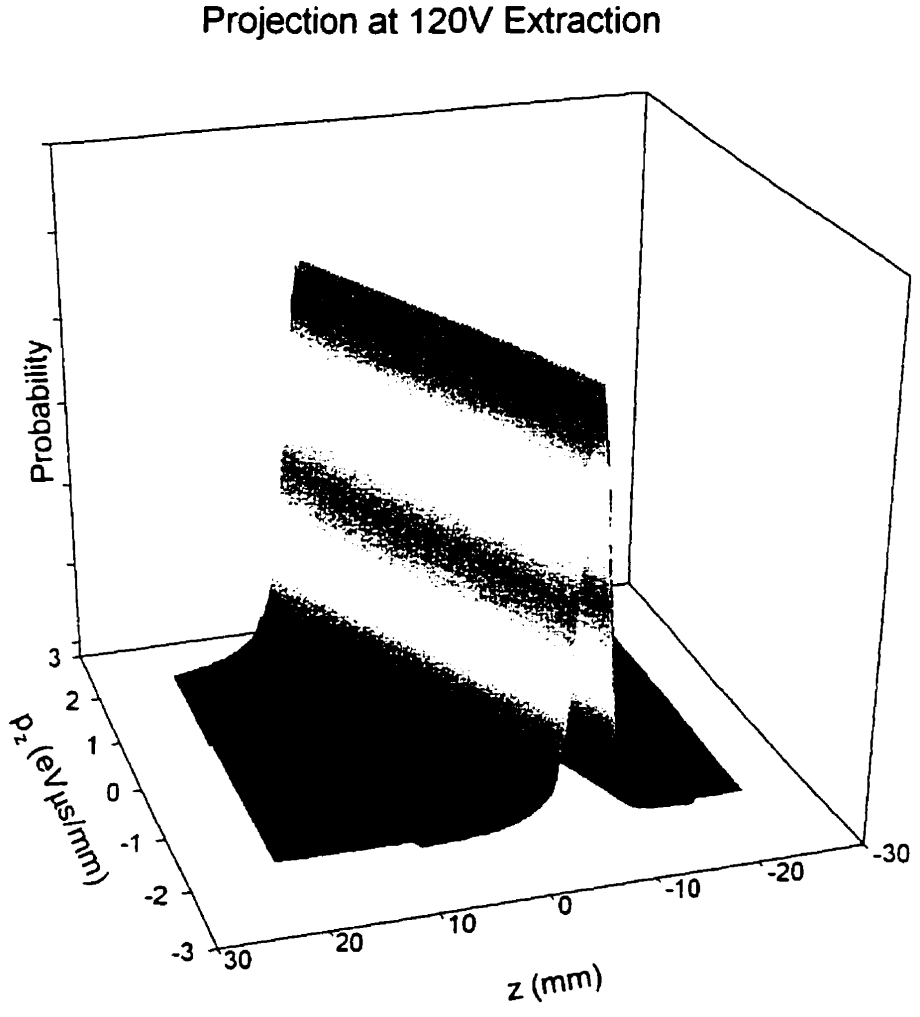

Fig. 5.18 Representation of the parallel phase space projection of the initial ion distribution in the LTRAP system. This projection was reconstructed from actual experimental data.

It can be seen in this figure that the time-of-flight spectrum indeed was translated into a parallel projection of the initial phase space distribution. Fig. 5.19 is another parallel projection of the same initial phase space distribution taken at a different viewing angle, corresponding to a 40V extraction voltage.

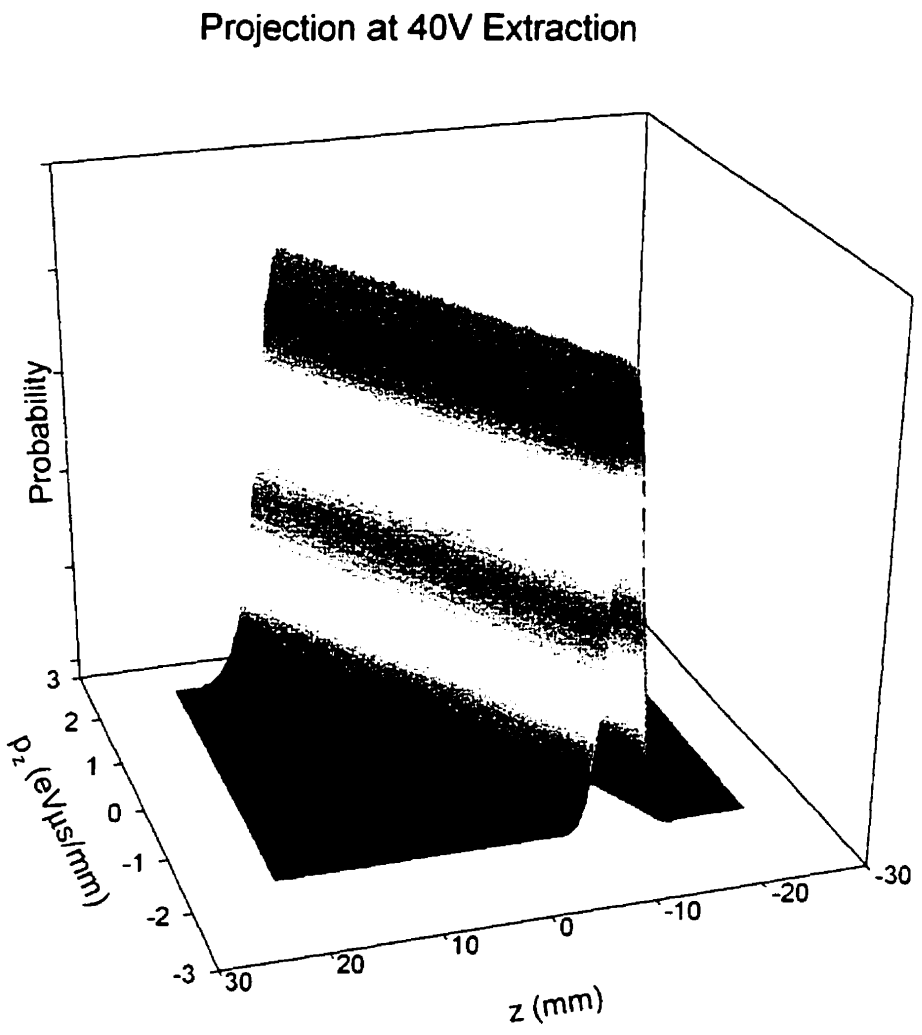

Fig. 5.19 Another phase space projection taken at an extreme viewing angle.

Taking the data from the series of experiments done on extraction voltages, from 40V to 200V, corresponded to a range of viewing angles from 10° to 14°, where 45° is defined as the angle between the z axis and the vector $\langle 1\text{mm}, 1\text{eV}\cdot\mu\text{s/mm}\rangle$. It should be noted that the figures were drawn with a left-handed coordinate system to facilitate viewing of the parallel projections.

Combining the 17 experimental TOF pulses at various extraction voltages according to the Fourier Slice theorem resulted in the composite figure Fig. 5.20.

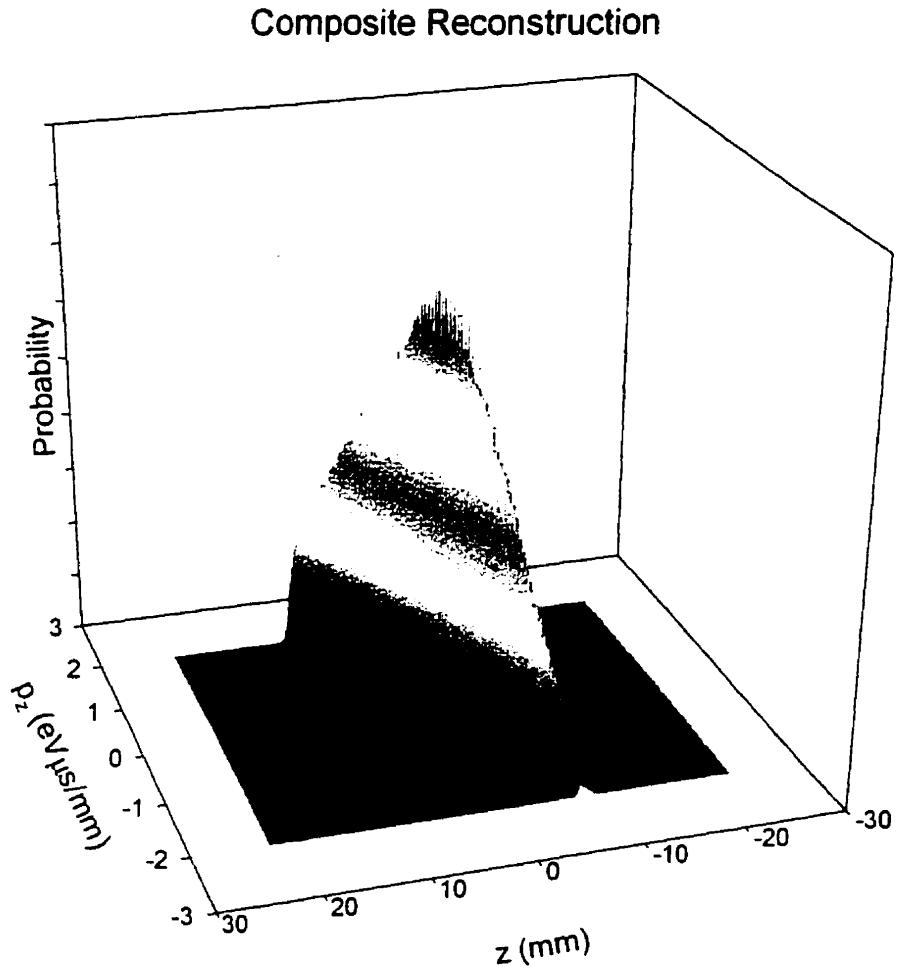

Fig. 5.20 Composite representation of the initial ion distribution, using projections from 17 different viewing angles.

This figure shows a fin-like structure in the phase space diagram, which was a result of the limited range of viewing angles provided by the available range of extraction voltages of 40V to 200V. It would be theoretically possible to improve the range of viewing angles by manipulating the ion ensemble as it drifted in the flight tube with a pulse down cavity system or a synchronized voltage ramping system. However, these would be difficult to implement.

By making some assumptions about the nature of the ion distribution, it was possible to improve the image of the initial ion distribution. Enforcing a four-fold symmetry to the distribution, that is, making it symmetric about the z and p_z axes, would result in a view constructed from four 4° viewing 'wedges' from each of the four quadrants in phase space. Essentially, what was done was to combine Fig. 5.20 with its three other mirror images to result in a fully symmetric ion distribution. The result is shown in Fig. 5.21.

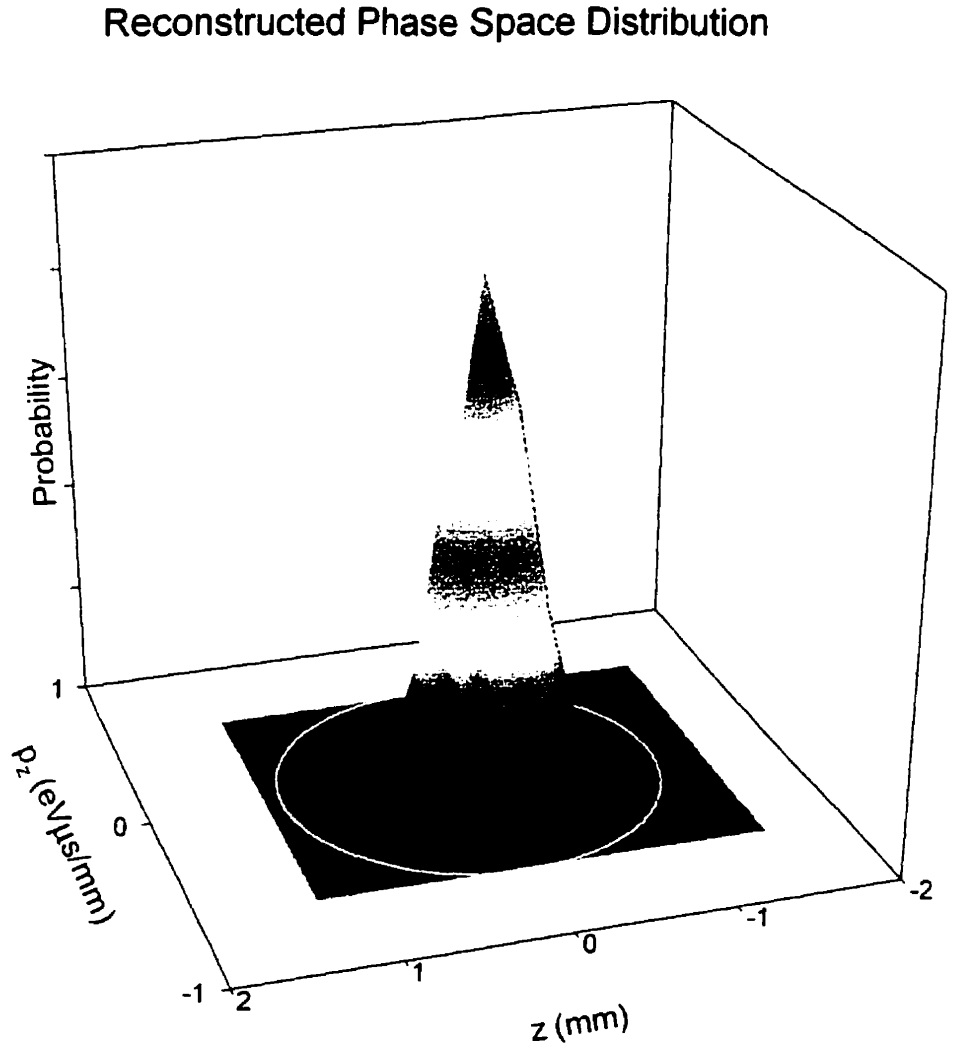

Fig. 5.21 Fully symmetric representation of the initial ion distribution in z-p_z phase space. The white ellipse at the base of the distribution represents the theoretical 3σ volume.

The assumption of fourfold symmetry is reasonable and the resulting ion distribution is in fact in agreement with the pseudopotential well model. In Fig. 5.21, the 3σ ellipse was drawn assuming a temperature of 0.035eV. While the reconstructed peak was slightly smaller in extent than the theoretical thermodynamic model of the ion ensemble, it was nevertheless in remarkably close agreement. It yielded values for σ_z and σ_{p_z} of 0.26mm and $0.0625\,\mathrm{eV}\cdot\mu\mathrm{s/mm}$ respectively, which can be compared to the thermodynamic model's values of 0.433mm and $0.22\,\mathrm{eV}\cdot\mu\mathrm{s/mm}$. Thus the slice projection validates the thermodynamic model.

Chapter 6 Summary and Conclusion

This thesis presented the studies carried out on a novel Linear RFQ Trap/Time-of-Flight mass spectrometer, one of the first of its kind. The goal was to investigate the phase space behavior of an ion ensemble confined in the LTRAP system to gain a better understanding of the physics governing its performance when used as a source for a TOF mass spectrometer. To this end, the experiments that were performed all led to the characterization of the ion ensemble in terms of its action diagrams, relating them to a temperature of the ion ensemble defined by the Gibb's distribution, and studying how this temperature changed with various experimental parameters.

6.1 Summary of Results

The LTRAP system was successfully built and tested and suitable operating parameters were established for obtaining the desired results. For a trap with this particular configuration, it was found that a well depth between –5V and –15V was the optimum range for trapping ions, with the quadrupole rods running with a q value of 0.3 to 0.6. It was also determined that the optimum buffer gas pressure, N_2 in this case, was approximately 10^{-4} Torr or greater. Below this pressure, the gas could not effectively cool the ion ensemble.

The detected ion pulse was typically gaussian in its time profile, quite clean and very distinct above the background noise. By analyzing the time-of-flight spectrum for the Cs^+ ions that were used it was possible to obtain information on the initial phase space configuration of the ion ensemble.

The detector system used was a custom designed MCP detector, mounted at the end of a 1-meter flight tube. The design of this detector allowed for minimum thickness (8.5mm) and had a measured charge amplification of 3.75×10^7. This unique configuration showed the benefits of slim design, high amplification, ease of construction and mechanical durability to protect the MCPs from cracking during assembly or handling of the detector.

The number of ions within a pulse was estimated using a multichannel analyzer to record a single ion event. In this way, the total area in the time-of-flight spectrum of a single ion pulse was determined with an accuracy of about 7%. This yielded figures for the trapping volume of the system. At a q value of 0.6, a well depth of -10V and a cooling/collection time of 50ms, the trap volume was estimated to be approximately 2500 ions. This translated to a detection efficiency of about 26.7% of the total incoming ions entering the LTRAP system.

This thesis also presented a theoretical framework for the behavior of the ion ensemble in the LTRAP system based on a thermodynamic model. The theory offered some simplifications, such as the pseudopotential well model and the assumption of phase-space symmetry, in order to make the computational aspect of the analysis more tractable. With these theoretical tools, a series of computer programs and simulations were created as tools to investigate the physical characteristics of the trapped ion ensemble. The computer simulations included a 3D pseudopotential well simulator, an ion ensemble generator based on a thermal distribution, the commercially available SIMION 6.0 to simulate the ion trajectories and a temperature-fitting program to evaluate the experimental data.

The results showed that after a sufficient cooling time, the ion ensemble achieved an equilibrium temperature of 0.0353 ± 0.0025eV, very near the buffer gas temperature,. The measurements also showed that with a buffer gas pressure of 5×10^{-4} Torr this temperature was reached in less than 10 ms.

A separate computer program was written in order to take the experimental data and reconstruct the phase space density function based on the technique of tomographic imaging. Although the apparatus proved inadequate to fully image the phase space distribution of ions in the LTRAP system (it only provided a 4° viewing angle), it did show that it was possible to perform the reconstruction. By assuming phase space symmetry, the imaged ion distribution then agreed quite well with the theoretical distribution.

6.2 Implications for TOF Mass Spectrometry

As an introduction to the consideration of an LTRAP type system as a source for a TOF mass spectrometer, consider the mass resolving power that could be obtained by using LTRAP as it was in the work of this thesis but with a time focusing device such as a reflectron for mass spectrometry. The theoretical mass resolving power is given by (1.2). Defining the mass interval Δm to be the Full Width at Half Maximum (FWHM) of the mass peak, the fraction of the number of ions appearing in this interval becomes 76%. For a collection of ions in thermodynamic equilibrium 76% will be within a radius of 1.69σ in the action diagrams. Thus the axial action area determining the mass resolving power will be about

$$3\pi\sigma_z\sigma_{p_z} = 3\pi\frac{1}{\omega}k_BT \tag{6.1}$$

and the axial extent of the action diagram determining the energy spread ΔE will be about

$$\Delta z = 3.4\frac{1}{\omega}\sqrt{\frac{k_BT}{m}} \tag{6.2}$$

With a reflectron the time of flight of the ions will be about 50 μs. Taking the case of $q = 0.24$, yielding an angular frequency ω of 0.3 rad/μs, with the extraction field of 6 V/mm that was used the theoretical resolving power for cesium ions at a temperature of 0.035eV will then be about $m/\Delta m = 250$.

A modern working TOF mass spectrometer could be designed to cover a range of masses up to a factor of 10. Considering then the possibility of trapping and resolving mass-1330 ions, it is seen that, because the radial pseudopotential, which is inversely proportional to the mass, drops by a factor of 10 the DC axial potential well must also be reduced by a factor of 10. This results in the angular frequency of the axial oscillations being reduced by a factor of 10 ($\sqrt{10}$ for the potential well depth and $\sqrt{10}$ for the mass) so that the axial extent of the collection, and hence the extraction energy spread increases by $\sqrt{10}$. Since the time to be resolved also increases by $\sqrt{10}$, while the action diagram area increases by 10, the resolving power for mass-1330 ions is also about 250.

Meanwhile, with the smaller axial trap potential depth any mass-133 ions collected along with the mass-1330 ions will have an angular oscillation frequency which is $1/\sqrt{3}$ times that for the stronger trap. However, since this results equally in both a larger action area and a larger axial spread, the resolving power is the same as before, i.e. 250. Thus the resolving power of a collection of ions of differing masses is independent of the mass. This is a characteristic feature of a linear RFQ trap/TOF mass spectrometer.

One of the reasons for the low resolving power of the LTRAP used in the present work is the low energy spread at extraction. For the weaker trap that would capture mass-1330 ions this would be about 30 eV at the extraction potential of 200 V. (Again, as with the resolving power, this would be independent of the ion mass.) By raising the extraction potential to 600 V the energy spread could be raised to about 100 eV, which is the normal range for a modern high-resolution TOF mass spectrometer. This would raise the mass resolving power to about 750.

However, while such a trap could, in principle, collect ions, it was demonstrated (see Fig. 5.4) that an axial potential well depth of about 10 V was necessary for efficient collection. As pointed out above, increasing the trap strength by this amount would destroy the radial confinement of the heavy ions unless the pseudopotential well depth is increased in proportion, i.e. by a factor of 10. This can be achieved by raising the RF amplitude by a factor of $\sqrt{10}$, i.e. to about $600V_{pp}$ on each rod pair. The q value for the light ions then increases to about 0.75, which is high but still tolerable (barely) for the radial confinement. This increases the axial oscillation frequency by a factor of $\sqrt{10}$. If the extraction field is increased by this same factor, by applying an extraction potential of about 1800 V, then the resolving power also increases by the factor, i.e. to about 2250. This is to be compared to the results of Lubman et al. [Lub92], who reported a mass resolution of 1300 for a Paul trap-TOF system with a reflectron.

Thus with higher-powered electronics, feasible with vacuum tubes and modern high-voltage switching transistors, LTRAP could be made into quite a workable TOF mass spectrometer. However, it should be possible to raise the resolving power even further. In the vacuum range in which LTRAP operates, the electric breakdown fields, with very clean electropolished surfaces are typically about 5000V/mm. By careful design it should therefore be possible to raise the RF potentials on the rod pairs to the order of $10\,kV_{pp}$. This was, in fact demonstrated in the work of Ghalambor-Dezfuli [Gha96]. To maintain the q values at these fields the RF would have to be increased by a factor of 4 in frequency, i.e. to about 3.2 MHz. The frequency of the axial oscillation in the trap would be then increased by a factor of 4. With the extraction potential increased to 7200 V, again quite feasible with modern switching transistors, the resolving power would increase by a factor of 4, to almost 10,000.

This would appear to be the feasibility limit of a LTRAP-TOF mass spectrometer.

The principle advantage of the LTRAP-TOF mass spectrometer would be in the high efficiency with which it can prepare a DC beam of ions for such a spectrometer. Thus it would be a powerful tool when only small quantities of ions are delivered. An example would be in fragmentation analysis after mass filtering of a primary beam and colliding this beam with background molecules in a collision cell. On the other hand, for moderate beam currents it would be quickly overloaded, being capable of processing only about 250,000 ions (100 × 2500) ions per second, corresponding to a beam current of only about 0.04 pA.

6.3 Suggested Future Work

From the above considerations it is obvious that one does not, at this time, proceed to the design of a LTRAP-TOF mass spectrometer for a mass resolving power of 10,000. Rather a staged approach should be taken. It seems that these stages should be

1. The installation of a reflectron for time focusing on the existing LTRAP_TOF system. This could be used to check the actual resolving power that system can achieve with cesium ions.

2. The development of the RF and the extraction electronics for operation of the trap at 600 V_{PP} on the rods.

3. The coupling of the system to an Atmospheric Pressure Ionization (API) -mass filter system for delivering ions of the mass range 100 to 1500 to the trap. This could then be used to test the performance of the system over an extended mass range.

4. The development of electronics to raise the potentials to the limit of what can be handled by the system electrodes.

In developing a system to reach the highest possible electric fields it might be useful to investigate the possibility of using a cylindrical structure for the RF fields rather than the commonly used rods. The geometry of such a cylinder is shown in Fig. 6.1. Each activated segment would cover an angle θ of the cylinder, with smaller cylindrical segments held at ground potential filling the gaps between the activated segments. The angle θ would be adjusted for maximizing the quadrupolar component of the field.

While this geometry would not have as ideal a quadrupole field as the rod geometry, it would have a much more ideal axial field geometry for the trapping field in that it would greatly reduce the off-axis azimuthal nonuniformities induced by the rods. It would also be advantageous in reducing the capacitive loading of the RF supply and in reducing the outside dimensions of the trap structure so as to ease problems associated with electrical breakdown to the trap surroundings.

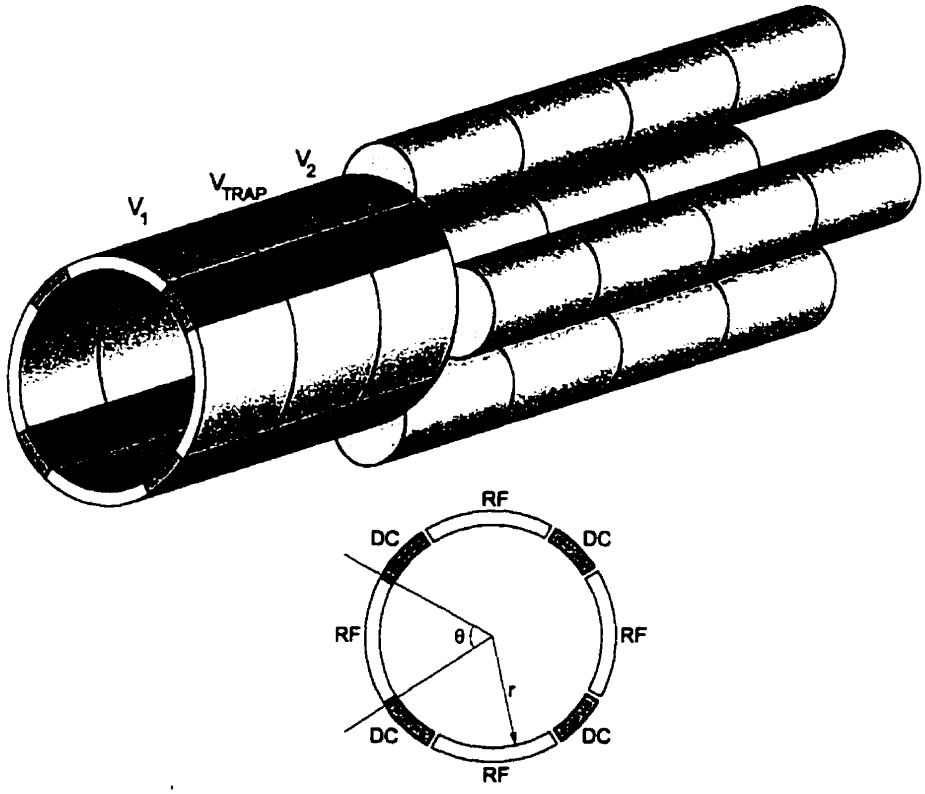

Fig. 6.1 Proposed hybrid trap design. *Above*-The trapping electrodes, defined by DC voltages V_1, V_{Trap} and V_2, are designed to improve axial electric field shape and enhance performance in ion confinement and extraction. *Below*-Cross-sectional view of one set of electrodes, showing the positions of both RF and DC segments.

References

[Bec89] Becker, S., G. Bollen, F. Kern, H.J. Kluge, R.B. Moore, G. Savard, L. Schweikhard, H. Stolzenberg, and the ISOLDE Collaboration. *CERN EP89-126*, 1989.

[Bla66] Blauth, E. W. *Dynamic Mass Spectrometry*. Amsterdam: Elsevier, 1966.

[Bre74] Breck, Donald W. "Chapter 7." Chap. in *Zeolite Molecular Sieves-Structure, Chemistry and Use*. USA: Wiley, 1974.

[Che97] Chernushevich, I.V., A.A. Shevchenko, B. Thomson, E.W. Ens, M. Mann, and K.G. Standing. "A Tandem Quadrupole/Time-of-Flight Mass Spectrometer with Electrospray Ionization.," 14th ICMS conference., 1997.

[Che99] Chernushevich, I.V., W. Ens, and K.G. Standing. "Orthogonal Injection TOFMS for Analyzing Biomolecules." *Analytical Chemistry News & Features* July 1, 1999 (1999): 452-461.

[Cot94] Cornish, T.J., and R.J. Cotter. "A Curved Field Reflectron Time-of-Flight Mass Spectrometer for the Simultaneous Focusing of Metastable Product Ions." *Rapid Communications in Mass Spectrometry* (USA) 8 (1994): 781-785.

[Cot94] Cornish, T.J., and R.J. Cotter. "A Curved Field Reflectron Time-of-Flight Mass Spectrometer for the Simultaneous Focusing of Metastable Product Ions." *Rapid Communications in Mass Spectrometry* (USA) 8 (1994): 781-785.

[Cot95] Cordero, M.M., T.J. Cornish, and R.J. Cotter. "Sequencing Peptides Without Scanning the Reflectron Post-Source Decay with a Curved-Field Reflectron Time-of-Flight Mass Spectrometer." *Rapid Communications in Mass Spectrometry* (USA) 9 (1995): 1356-1361.

[Cot95] Cordero, M.M., T.J. Cornish, and R.J. Cotter. "Sequencing Peptides Without Scanning the Reflectron Post-Source Decay with a Curved-Field Reflectron Time-of-Flight Mass Spectrometer." *Rapid Communications in Mass Spectrometry* (USA) 9 (1995): 1356-1361.

[Dah95] Dahl, David A., manual. *SIMION 3D 6.0 User's Manual.* USA: Lockheed Martin Idaho Technologies, 1995.

[Daw76] Dawson, P.H. *Quadrupole Mass Spectrometry and Its Applications.* Amsterdam: Elsevier Scientific Publishing Company, 1976.

[Day54] Dayton, I.E., F.C. Shoemaker, and R.F. Mozley. "The Measurement of Two-Dimensional Fields. Part II: Study of a Quadrupole Magnet." *Rev. Sci. Instrum.* 25 (1954): 485.

[Deh67] Dehmelt, H. *Advan. At. Mol. Phys.* 3 (1967): 53.

[Den71] Denison, D.R. "Operating Parameters of a Quadrupole in a Grounded Cylindrical Housing." *J. Vac. Sci. Technol.* 8 (1971): 266.

[Dou98] Campbell, J.M., B.A. Collings, and Douglas,D.J. "A New Linear Ion Trap Time-of-Flight System with Tandem Mass Spectrometry Capabilities." *Rapid Communications in Mass Spectrometry*, 12 (1998): 1463-1474.

[Ell78] Ellis, H.W., and E. W. McDaniel. *Transport Properties of Gaseous Ions Over a Wide Energy Range. Part II.* Atomic Data and Nuclear Data Tables vols. USA: Academic Press, Inc., 1978.

[Gha96] Ghalambor-Dezfuli, A.M. "Injection, Colling, and Extraction of Ions from a Very Large Paul Trap." Ph.D. Thesis, McGill University. 1996.

[Gol59] Goldstein, Herbert. *Classical Mechanics.* USA: Addison-Wesley Publishing Company, Inc., 1959.

[Gro96] Wilhelm, U., K.P. Aicher, and J. Grotemeyer. "Ion Storage Combined with Reflectron Time-of-Flight Mass Spectrometry: Ion Cloud Motions as a Result of Jet-Cooled Molecules." *International Journal of Mass Spectrometry and Ion Processes* (Germany) 152 (1996): 111-120.

[Gro96a] Wilhelm, U., C. Weickhardt, and J. Grotemeyer. "Ion Trajectory Calculations for a Quadrupole-Ion-Trap Reflectron Time-of-Flight Hybrid Instrument- Effects of the Initial rf-Phase and the Trapping Time on an Ion Bunch Produced from a Molecular Beam." *Rapid Communications in Mass Spectrometry* (Germany) 10 (1996): 473-477.

[Hal88] Halliday, D., R. Resnick, and J. Merrill, textbook. *Fundamentals of Physics*. USA: John Wiley & Sons, 1988.

[Han72] *Handbook of Chemistry and Physics*. Robert C. Weast. 52. USA: The Chemical Rubber Co., 1972.

[Her00] Herfurth, F., J. Dilling, A. Kellerbauer, G. Bollen, S. Henry, H.J. Kluge, E. Lamour, D. Lunney, R.B. Moore, C. Scheidenberger, S. Schwarz, G. Sikler, and J. Szerypo. "A Linear Radiofrequency Ion Trap for Accumulation and Bunching of Radioactive Ion Beams." *Preprint Submitted to Elsevier* (2000).

[Hop99] Hopfgartner, G., I. Chernushevich, T. Covey, J.B. Plomley, and R. Bonner. "Exact Mass Measurement of Product Ions for the Structural Elucidation of Drug Metabolites with a Tandem Quadrupole Orthogonal-Acceleration Time-of-Flight Mass Spectrometer." *J Am Soc Mass Spectrom* 10 (1999): 1305-1314.

[Kak88] Kak, A.C., and M. Slaney. *Principles of Computerized Tomographic Imaging*. USA: IEEE Press, 1988.

[Kim97] Kim, T. "Buffer Gas Cooling of Ions in a Radio Frequency Quadrupole Ion Guide." Ph.D. Thesis, McGill University. 1997.

[Kin24] Kingdon, K.N., and J. Langmuir., 1924.

[Law83] Lawson, J.D. "Space Charge Optics." Chap. in *Applied Charged Particle Optics*. 2. USA: Academic Press, Inc., 1983.

[Lub92] Michael, S.M., Chien,M., and Lubman,D.M. "An Ion Trap Storage/Time-of-Flight Mass Spectrometer." *Rev. Sci. Instrum.* (Michigan) 63, 10 (1992): 4277.

[Lub93] Michael, S.M., B.M. Chien, and D.M. Lubman. "Detection of Eletrospray Ionization Using a Quadrupole Ion Trap Storage/Reflectron Time-of-Flight Mass Spectrometer." *Analytical Chemistry* 65 (1993): 2614-2620.

[Lun92] Lunney, M.D.N. "The Phase Space Volume of ion clouds in Paul traps." Ph.D. Thesis, McGill University. 1992.

[Maj68] Major, F.G., and H.G. Dehmelt. "Exchange-Collision Technique for the RF Spectroscopy of Stored Ions." *Phys. Rev.* 170 (1968): 91.

[Moo92] Moore, R.B., M.D.N. Lunney, G. Rouleau, and G. Savard. "Collection and Cooling and Delivery of ISOL beams." *Nucl. Instr. and Meth.* B70 (1992): 482-489.

[Mor96] Morris, H.R., T. Paxton, A. Dell, J. Langhorne, M. Berg, R.S. Bordoli, J. Hoyes, and R.H. Bateman. "High Sensitivity Collisionally-Activated Decomposition Tandem Mass Spectrometry on a Novel Quadrupole/Orthogonal-Acceleration Time-of-Flight Mass Spectrometer." *Rapid Communications in Mass Spectrometry* 10 (1996): 889-896.

[Nib86] Nibbering, N.M.M. "Proceedings of the 10th International Mass Spectrometry Conference.," Todd, J.F.J. London, Wiley. 1986. p.417.

[Nie99] Niessen, W.M.A. *Liquid Chromatography - Mass Spectrometry.* 2nd Edition. Chromatographic Science Series. USA: Marcel Dekker, Inc., 1999.

[Pre95] Press, W. H., S. A. Teukolsky, W. T. Vetterling, and B. P. Flannery. *Numerical Recipes in C - the Art of Scientific Computing.* USA: Cambridge University Press, 1995.

[Qia96] Qian, M.G., J.T. Wu, S. Parus, and D.M. Lubman. "The Development of a Data System for a Combination of Liquid Chromatography or Capillary Electrophoresis with an Ion Trap Storage/Reflectron Time-of-Flight Mass Detector." *Rapid Communications in Mass Spectrometry* 10 (1996): 1209-1214.

[Rou92] Rouleau, G. "A Tandem Paul-Penning Trap Mass Measurement System for Radionuclides." Ph.D. thesis, McGill University. 1992.

[She97] Shevchenko A., I. Chernushevich, W. Ens, K.G. Standing, B. Thomson, M. Wilm, and M. Mann. "Rapid *'de Novo'* Peptide Sequencing by a Combination of Nanoelectrospray, Isotopic Labeling and a Quadrupole/Time-of-Flight Mass Spectrometer." *Rapid Communications in Mass Spectrometry* 11 (1997): 1015-1024.

[Sta94] Verentchikov,A.N., W. Ens, and K.G. Standing. "Reflecting Time-of-Flight Mass Spectrometer with an Electrospray Ion Source and Orthogonal Extraction." *Analytical Chemistry* 66, 1 (1994): 126-133.

[Str55] Straubel, H. *Naturwiss*, 1955.

[Whe74] Whetten, N.R. "Macroscopic Particle Motion in Quadrupole Fields." *J. Vac. Sci. Technol.* 11, 2 (1984): 515-518.

[Wu96] Wu, J., M.G. Qian, M.X. Li, L. Liu, and D.M. Lubman. "Use of an Ion Trap Storage/Reflectron Time-of-Flight Mass Spectrometer as a Rapid and Sensitive Detector for Capillary Electrophoresis in Protein Digest Analysis." *Analytical Chemistry* 68 (1996): 3388-3396.

[Wue59] Wuerker, R.F., H. Shelton, and R.V. Langmuir. "Electrodynamic Containment of Charged Particles." *J. Appl. Phys.* 30 (1959): 515.

Appendix A: Autocad® Rendered Diagrams